

# HUNGARIAN

Journal of

# INDUSTRIAL

# CHEMISTRY

Edited by

the Hungarian Oil & Gas Research Institute (MÁFKI),  
the Research Institute for Heavy Chemical Industries (NEVIKI),  
the Research Institute for Technical Chemistry of the  
Hungarian Academy of Sciences (MÜKKI),  
the University of Veszprém (VE) Veszprém (Hungary)



Volume 18.

1990.

Number 1.

HU ISSN: 0133-0276  
CODEN: HJICAI

Editorial Board:

R. CSIKÓS and Gy. MÓZES  
Hungarian Oil & Gas Research Institute  
(MÁFKI Veszprém)

A. SZÁNTÓ and M. NÁDASY  
Research Institute for Heavy Chemical Industries  
(NEVIKI Veszprém)

L. MARKÓ and T. BLICKLE  
Research Institute for Technical Chemistry  
of the Hungarian Academy of Sciences  
(MÜKKI Veszprém)

P. ÁRVA and G. DEÁK  
University of Veszprém (VE Veszprém)

Editor-in Chief:  
E. BODOR

Assistant Editor:  
J. DE JONGE

University of Veszprém (VE Veszprém)

---

The "Hungarian Journal of Industrial Chemistry" is a joint publication of the Veszprém scientific institutions of the chemical industry that deals with the results of applied and fundamental research in the field of chemical processes, unit operations and chemical engineering. The papers are published in two numbers at irregular intervals in one annual volume, in English.

Editorial Office:  
University of Veszprém  
"Hungarian Journal of Industrial Chemistry"  
H-8201 Veszprém, P.O. Box: 158.  
Hungary

---

Distributor:  
KULTURA Foreign Trading Co. H-1389, BUDAPEST, P.O. Box 149. Hungary.

---

FELELŐS SZERKESZTŐ: DR. BODOR ENDRE H-8201 Veszprém, P.O. Box 158  
KIADJA A PALLAS LAP- ÉS KÖNYVKIADÓ VÁLLALAT 1073 Bp. VII. ERZSÉBET (LENIN) KRT. 9-11.  
TELEFON: 221-285. LEVÉLCÍM: 1906 BP., PF. 223.  
FELELŐS KIADÓ: NÉMETH JENŐ VEZÉRIGAZGATÓ

## ASYMPTOTIC THEORY OF NON-LINEAR TRANSPORT PHENOMENA. II. HEAT TRANSFER

CHR. BOYADJIEV

(Institute of Chemical Engineering, Bulgarian Academy of Sciences, Sofia 1040, Bulgaria)

Received: March 29, 1989

An asymptotic theory of heat transfer in the boundary layer, where heat transfer is accompanied with non-linear mass transfer, resulting from intensive mass exchange, is presented. It is demonstrated that the direction of the mass exchange influences the heat transfer rate.

### Introduction

Theoretical study of non-linear mass transfer [1,2] has shown that the changes in mass transfer rate result from the intensive mass exchange influencing the hydrodynamics. This could lead to analogous changes in the heat transfer rate when thermal diffusivity and diffusive heat transfer are neglected [3,4].

The results from the numerical theory [3] show that the rate of heat transfer considerably depends on Schmidt and Lewis numbers. Taking this into consideration, an asymptotic theory, which avoids the need to solve a system of nonlinear equations in each particular case is presented here.

### The Mathematical Model

The mathematical description of the heat transfer, resulting from a simultaneous heat and mass exchange among a semi-infinite plate and a fluid flux flowing along it, is characterized by the nonlinearity of the convective mass transfer equation and linearity of the convective heat transfer equation. From the above, the conclusion follows that the equation describing the convective heat transfer in the boundary layer approximation has to be added to the mathematical description in [1]:

$$u \frac{\partial t}{\partial x} + v \frac{\partial t}{\partial y} = a \frac{\partial^2 t}{\partial y^2} \quad (1)$$

$$\begin{aligned} x=0, & \quad t=t_0 \\ y=0, & \quad t=t^* \\ y \rightarrow \infty, & \quad t=t_0 \end{aligned}$$

Introducing the similarity variables [1] in Equation (1) leads to the following boundary value problem:

$$T'' + \bar{\varepsilon}_t \Phi T' = 0 \quad (2)$$

$$T(0) = 1, \quad T(\infty) = 0,$$

where:

$$\bar{\varepsilon}_t = \alpha \varepsilon, \quad \alpha = \frac{D}{a} = Le^{-1}, \quad (3)$$

$$T = \frac{t - t_0}{t^* - t_0}, \quad T = T(\eta),$$

In Equation (2)  $\Phi(\eta)$  is determined from a  $\Theta$  series expansion [3] and the solution of Equation (2) can be found from:

$$T = T_0 + \Theta T_1 + \Theta^2 T_2 + \dots \quad (4)$$

Introducing Equation (4) in Equation (2) leads to equations for the separate approximations, where  $\Phi_0$ ,  $\Phi_1$  and  $\Phi_2$  are determined in [1].

In the zeroth - order approximation is directly obtained:

$$T_0'' + \bar{\varepsilon}_t \Phi_0 T_0' = 0 \quad (5)$$

$$T_0(0) = 1, \quad T_0(\infty) = 0$$

The solution of (5) can be obtained analogous to the one in [1]:

$$T_0(\eta) = 1 - \frac{1}{\varphi_{0t}} \int_0^z E(\varepsilon_t, p) dp, \quad z = \frac{2}{\varepsilon} \eta, \quad (6)$$

where:

$$\varphi_{0t} = \int_0^\infty E(\varepsilon_t, p) dp \approx 3.01 \varepsilon_t^{-0.7} \quad (7)$$

$$E(\varepsilon_t, p) = \exp \left[ -\frac{\varepsilon_t^2}{2} \int_0^p f(s) ds \right]$$

$$\varepsilon_t = (\varepsilon \bar{\varepsilon}_t)^{0.5}$$

The first-order approximation for the small parameter  $\Theta$  is:

$$T_1'' + \bar{\varepsilon}_t (\Phi_0 T_1' + \Phi_1 T_0') = 0 \quad (8)$$

$$T_1(0) = 0, \quad T_1(\infty) = 0$$

The solution of (8) is:

$$T_1(\eta) = \frac{\bar{\varepsilon}_t \varphi_{3t}}{\varphi_0 \varphi_{0t}^2} \int_0^z E(\varepsilon_t, p) dp - \frac{\bar{\varepsilon}_t}{\varphi_0 \varphi_{0t}} \int_0^z \left[ \int_0^p \varphi(s) ds \right] E(\varepsilon_t, p) dp, \quad (9)$$

where:

$$\varphi_{3t} = \int_0^\infty \left[ \int_0^p \varphi(s) ds \right] E(\varepsilon_t, p) dp \approx 6.56 \varepsilon_t^{-1.6} \quad (10)$$

The boundary value problem for the second-order approximation is:

$$T_2'' + \bar{\varepsilon}_t (\Phi_0 T_2' + \Phi_2 T_0' + \Phi_1 T_1') = 0 \quad (11)$$

$$T_2(0) = 0, \quad T_2(\infty) = 0$$

The solution of (11) is:

$$T_2(\eta) = - \left[ \frac{\bar{\varepsilon}_t \varepsilon \varphi_{3t}}{\varphi_0^2 \varphi_{0t}^2} \left( \frac{\varphi_3}{\varphi_0} + \frac{\bar{\varepsilon}_t \varphi_{3t}}{\varepsilon \varphi_{0t}} \right) - \frac{\bar{\varepsilon}_t^2 \varphi_{33t}}{2 \varphi_0^2 \varphi_{0t}^2} - \frac{\bar{\varepsilon}_t \bar{\varphi}_{33t}}{2 \varepsilon \varphi_0^2 \varphi_{0t}^2} \right] \int_0^z E(\varepsilon_t, p) dp + \quad (12)$$

$$+ \frac{\bar{\varepsilon}_t \varepsilon}{\varphi_0^2 \varphi_{0t}} \left( \frac{\varphi_3}{\varphi_0} + \frac{\bar{\varepsilon}_t \varphi_{3t}}{\varepsilon \varphi_{0t}} \right) \int_0^z \left[ \int_0^p \varphi(s) ds \right] E(\varepsilon_t, p) dp -$$

$$- \frac{\bar{\varepsilon}_t^2}{2 \varphi_0^2 \varphi_{0t}} \int_0^z \left[ \int_0^p \varphi(s) ds \right]^2 E(\varepsilon_t, p) dp - \frac{\bar{\varepsilon}_t}{2 \varepsilon \varphi_0^2 \varphi_{0t}} \int_0^z \left[ \int_0^p \bar{\varphi}(s) ds \right] E(\varepsilon_t, p) dp,$$

where:

$$\varphi_{33t} = \int_0^\infty \left[ \int_0^p \varphi(s) ds \right]^2 E(\varepsilon_t, p) dp \approx 24 \varepsilon_t^{-2.6} \quad (13)$$

$$\bar{\varphi}_{33t} = \int_0^\infty \left[ \int_0^p \bar{\varphi}(s) ds \right] E(\varepsilon_t, p) dp \approx 0.326 \varepsilon_t^{-3.26}$$

### Heat Transfer Kinetics

The average heat transfer rate for a plate of length "L" is determined from the average heat flow:

$$J_t = k_t (t^* - t_0) = \frac{1}{L} \int_0^L I_t dx, \quad (14)$$

which has a convective component as well:

$$I_t = -\lambda \left( \frac{\partial t}{\partial y} \right)_{y=0} + \varrho_0 c_p v t \quad (15)$$

The Nusselt number can be determined from (3), (14) and (15):

$$\text{Nu} = \frac{k_t L}{\lambda} = -\text{Pe}^{0.5} \left[ T'(0) + \Theta \bar{\varepsilon}_t \frac{t^*}{t^* - t_0} \Psi'(0) \right], \quad (16)$$

where:

$$\text{Pe} = \frac{u_0 L}{D} \quad (17)$$

In Equation (16)  $\Psi'(0)$  is determined in [1], while  $T'(0)$  can be obtained directly from (4), (6), (9) and (12):

$$T'(0) = -\frac{2}{\varepsilon \varphi_{0t}} + \Theta \frac{2\alpha \varphi_{3t}}{\varphi_0 \varphi_{0t}^2} - \Theta^2 \left[ \frac{2\bar{\varepsilon}_t \varphi_{3t}}{\varphi_0^2 \varphi_{0t}^2} \left( \frac{\varphi_3}{\varphi_0} + \frac{\alpha \varphi_{3t}}{\varphi_{0t}} \right) - \frac{\alpha \bar{\varepsilon}_t \varphi_{33t}}{\varphi_0^2 \varphi_{0t}^2} - \frac{\alpha \bar{\varphi}_{33t}}{\varepsilon \varphi_0^2 \varphi_{0t}^2} \right]. \quad (18)$$

Comparison of the result for a dimensionless heat flow, obtained from the asymptotic theory (18), with data from the numerical theory  $T'_N(0)$ , obtained in [3], is presented in *Table 1*. It demonstrates the good accuracy of the asymptotic theory.

*Table 1*

$\varepsilon = 1, \quad \alpha = 2, \quad \bar{\varepsilon}_t = 2, \quad \varepsilon_t = 2^{0.5}$		
$\Theta$	$-T'_N(0)$	$-T'(0)$
0	0.846	0.847
+0.1	0.762	0.765
-0.1	0.943	0.945
+0.2	0.690	0.700
-0.2	1.063	1.059
+0.3	0.633	0.652
-0.3	1.212	1.190

The results obtained are valid only for gases. It was shown that the nonlinear mass transfer does not influence heat transfer for liquids, because the Lewis number has a large value ( $\alpha \approx 10^{-2}$ ). In other words, mass transfer in the thin diffusive boundary layer cannot perturb the "thick" temperature boundary layer. This follows directly from Equation (2), where the small value of  $\bar{\varepsilon}_t$  practically eliminates the nonlinear effect resulting from  $\Phi(0) = 0$ .

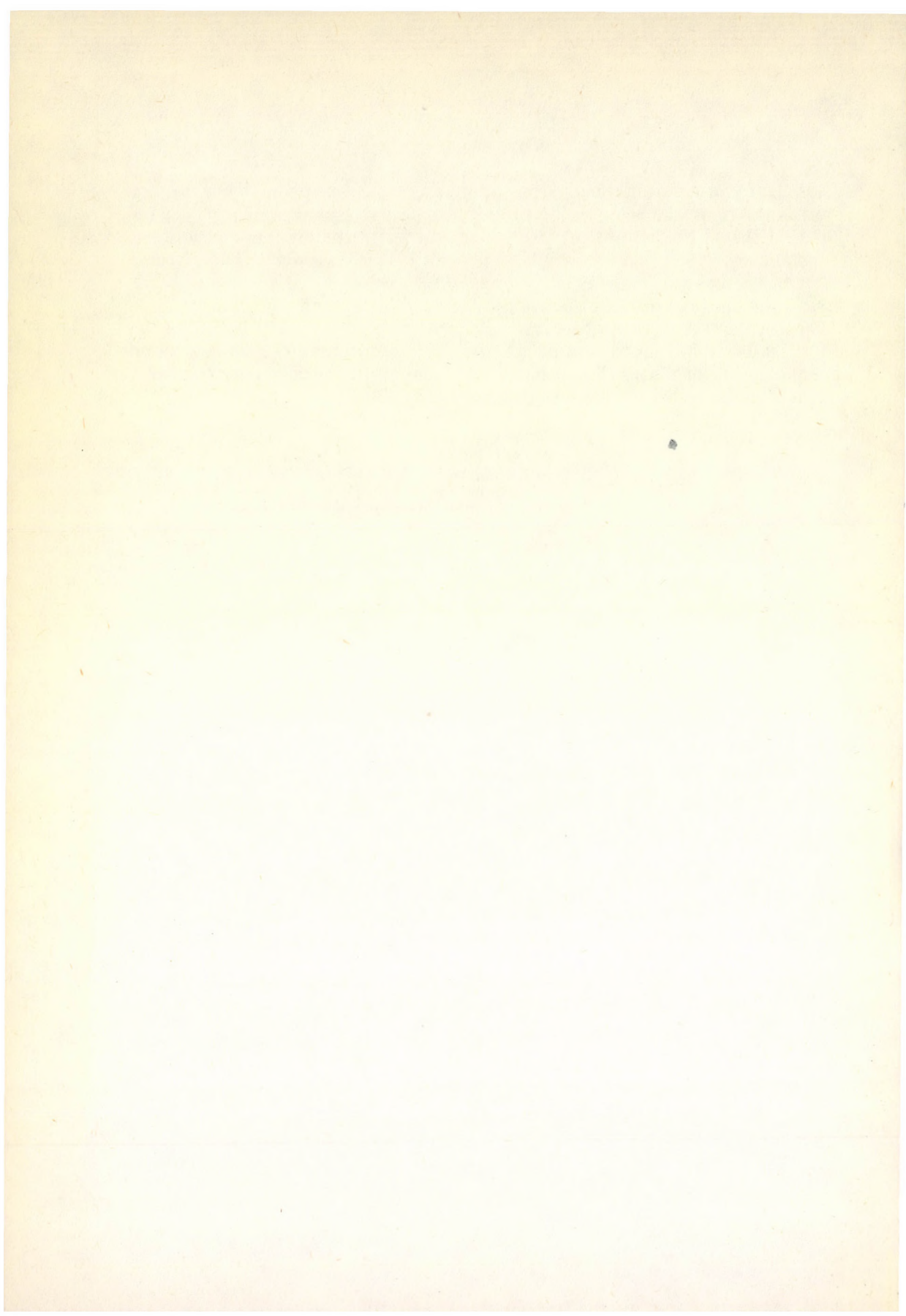
### Conclusion

It was clearly seen that in the presence of intensive mass exchange, from the gas towards the rigid wall ( $\Theta < 0$ ), the rate of heat transfer increases. Contrary to the linear theory predictions ( $\Theta = 0$ ), where, in the approximations considered, heat and mass transfer are independent. The rate of heat transfer decreases when the intensive mass exchange is from the solid wall towards the gas ( $\Theta > 0$ ). The direction of the heat transfer does not influence these effects. They can be used to control the rate of heat transfer.

The relationship for the rate of heat transfer, accurate to the second order approximation for the small parameter  $\Theta$ , provides the necessary accuracy for solving different problems in chemical engineering.

### REFERENCES

1. BOYADJIEV, CHR. and TOSCHEV, E.: *Hung. J. Ind. Chem.* 1989, 17 (3) 457-463.
2. BOYADJIEV, CHR. and VULCHANOV, N.: *C.r. Acad. Bulg. Sci.* 1987, 40 (11), 35-38.
3. BOYADJIEV, CHR. and VULCHANOV, N.: *C.r. Acad. Bulg. Sci.* 1988, 41 (10), 49-52.
4. FRANK-KAMENITSKII, D. A.: *Diffusion and Heat Transfer in Chemical Kinetics*. Nauka. Moscow. 1967. pp. 170-185.



## ASYMPTOTIC THEORY OF THE NON-LINEAR TRANSPORT PHENOMENA

### III. MULTICOMPONENT MASS TRANSFER

CHR. BOYADJIEV

(Institute of Chemical Engineering, Bulgarian Academy of Sciences, Sofia 1040, Bulgaria)

Received: March 29, 1989

An asymptotic theory of multicomponent mass transfer in the approximations of independent diffusion is suggested. Multicomponent mass transfer in the boundary layer when the mass transfer of one of the components is non-linear as a result of intensive mass exchange is studied. It is demonstrated that the mass exchange direction influences the rate of the multicomponent mass transfer.

### Introduction

Intensive mass exchange, leading to non-linear mass transfer in a boundary layer can induce sufficient perturbation in the hydrodynamics of this layer [1,2]. The transport phenomena kinetics in the boundary layer is also changed. It was shown [3,4] how non-linear mass transfer influences the heat transfer rate in cases of combined heat and mass exchange.

It is expected that because of its pronounced hydrodynamic nature, the same effect will be observed in cases of combined mass exchange of several components, if the concentration gradient of only one of them is big enough to cause the appearance of the effect of the non-linear mass transfer.

The theory of diffusion in multicomponent systems [5,6] showed that independent diffusion approximation is valid in two cases: when the concentrations of the components are low and when their diffusivities do not considerably differ. This provides a sufficient basis to solve the problem of the influence of non-linear mass transfer on the multicomponent mass transfer in the independent diffusion approximation [5,6]. The numerical solution of this problem [7] shows that the rate of multicomponent mass transfer depends to a great extent on the Schmidt numbers for the separate components.

### Mathematical Model

The mathematical description of multicomponent mass transfer, which is realised when a multicomponent mass exchange between a semi infinite rigid plate and a fluid flowing along it takes place, is characterized with the non-linearity of the equation of convective diffusion for one of the components and with the linearity of the equations for the rest of the  $n$  components. It directly follows that the following system of equations has to be added to the mathematical description of the non-linear mass transfer in [1]:

$$u \frac{\partial c_i}{\partial x} + v \frac{\partial c_i}{\partial y} = D_i \frac{\partial^2 c_i}{\partial y^2} \quad (1)$$

$$x=0, \quad c_i = c_{0i}$$

$$y=0, \quad c_i = c_i^*$$

$$y \rightarrow \infty, \quad c_i = c_{0i}, \quad i = 1, \dots, n$$

Introducing the similarity variables from [2] yields the following system of equations:

$$\Psi_i' + \bar{\varepsilon}_i \Phi \Psi_i = 0 \quad (2)$$

$$\Psi_i(0) = 1, \quad \Psi_i(\infty) = 0, \quad i = 1, \dots, n$$

where:

$$\bar{\varepsilon}_i = \alpha_i \varepsilon, \quad \alpha_i = \left( \frac{\varepsilon_i}{\varepsilon} \right)^2, \quad \varepsilon_i = \text{Sc}_i^{0.5}, \quad (3)$$

$$\text{Sc}_i = \frac{v}{D_i}, \quad \Psi_i = \Psi_i(\eta) = \frac{c_i - c_{0i}}{c_i^* - c_{0i}}, \quad i = 1, \dots, n.$$

As  $\Phi(\eta)$  is determined from a series of  $\Theta$  [2], and the solution of Equation (2) will be found from:

$$\Psi_i = \Psi_i^{(0)} + \Theta \Psi_i^{(1)} + \Theta^2 \Psi_i^{(2)} + \dots, \quad i = 1, \dots, n \quad (4)$$

Substitution of (4) into Equation (2) allows an equation to be obtained for the separate approximations, where  $\Phi_0, \Phi_1, \Phi_2$  are determined in [2].

In the zeroth-order approximation one directly obtains:

$$\Psi_i^{(0)''} + \bar{\varepsilon}_i \Phi_0 \Psi_i^{(0)'} = 0 \quad (5)$$

$$\Psi_i^{(0)}(0) = 1, \quad \Psi_i^{(0)}(\infty) = 0, \quad i = 1, \dots, n$$

The solution of (5) is analogous to that in [2]:

$$\Psi_i^{(0)}(\eta) = 1 - \frac{1}{\varphi_{0i}} \int_0^\eta E(\varepsilon_i, p) dp, \quad i = 1, \dots, n, \quad (6)$$

where:

$$\varphi_{0i} = \int_0^\infty E(\varepsilon_i, p) dp \approx \begin{cases} 3.01 Sc_i^{-0.35} & \text{for the gas [2]} \\ 3.12 Sc_i^{-0.34} & \text{for the liquid [2]} \end{cases} \quad (7)$$

$$E(\varepsilon_i, p) = \exp \left[ -\frac{\varepsilon_i^2}{2} \int_0^p f(s) ds \right], \quad i = 1, \dots, n$$

The first-order approximation is:

$$\begin{aligned} \Psi_i^{(1)''} + \bar{\varepsilon}_i(\Phi_0 \Psi_i^{(1)'} + \Phi_1 \Psi_i^{(0)'}) &= 0 \\ \Psi_i^{(1)}(0) &= 0, \quad \Psi_i^{(1)}(\infty) = 0, \quad i = 1, \dots, n \end{aligned} \quad (8)$$

The solution of (8) is:

$$\Psi_i^{(1)}(\eta) = \frac{\bar{\varepsilon}_1 \varphi_{3i}}{\varphi_0 \varphi_{0i}^2} \int_0^z E(\varepsilon_i, p) dp - \frac{\bar{\varepsilon}_i}{\varphi_0 \varphi_{0i}} \int_0^z \left[ \int_0^p \varphi(s) ds \right] E(\varepsilon_i, p) dp, \quad i = 1, \dots, n, \quad (9)$$

where  $\varphi_{3i}$  is obtained in [2]:

$$\varphi_{3i} = \int_0^\infty \left[ \int_0^p \varphi(s) ds \right] E(\varepsilon_i, p) dp \approx \begin{cases} 6.56 Sc_i^{-0.8} & \text{for the gas} \\ 5.08 Sc_i^{-0.67} & \text{for the liquid} \end{cases} \quad i = 1, \dots, n \quad (10)$$

The boundary value problem for the second-order approximation is:

$$\begin{aligned} \Psi_i^{(2)''} + \bar{\varepsilon}_i(\Phi_0 \Psi_i^{(2)'} + \Phi_2 \Psi_i^{(0)'}) + \Phi_1 \Psi_i^{(1)'} &= 0 \\ \Psi_i^{(2)}(0) &= 0, \quad \Psi_i^{(2)}(\infty) = 0, \quad i = 1, \dots, n \end{aligned} \quad (11)$$

Its solution is:

$$\begin{aligned} \Psi_i^{(2)}(\eta) &= - \left[ \frac{\varepsilon \bar{\varepsilon} \varphi_{3i}}{\varphi_0^2 \varphi_{0i}^2} \left( \frac{\varphi_3}{\varphi_0} + \frac{\bar{\varepsilon}_i \varphi_{3i}}{\varepsilon \varphi_{0i}} \right) - \frac{\bar{\varepsilon}_i^2 \varphi_{33i}}{2 \varphi_0^2 \varphi_{0i}^2} - \frac{\bar{\varepsilon}_i \bar{\varphi}_{33i}}{2 \varepsilon \varphi_0^2 \varphi_{0i}^2} \right] \int_0^z E(\varepsilon_i, d) dp + \\ &+ \frac{\varepsilon \bar{\varepsilon}_i}{\varphi_0^2 \varphi_{0i}} \left( \frac{\varphi_3}{\varphi_0} + \frac{\bar{\varepsilon}_i \varphi_{3i}}{\varepsilon \varphi_{0i}} \right) \int_0^z \left[ \int_0^p \varphi(s) ds \right] E(\varepsilon_i, p) dp - \\ &- \frac{\bar{\varepsilon}_i^2}{2 \varphi_0^2 \varphi_{0i}} \int_0^z \left[ \int_0^p \varphi(s) ds \right]^2 E(\varepsilon_i, p) dp - \\ &- \frac{\bar{\varepsilon}_i}{2 \varepsilon \varphi_0^2 \varphi_{0i}} \int_0^z \left[ \int_0^p \bar{\varphi}(s) ds \right] E(\varepsilon_i, p) dp, \quad i = 1, \dots, n \end{aligned} \quad (12)$$

where [2]:

$$\begin{aligned} \varphi_{33i} &= \int_0^\infty \left[ \int_0^P \varphi(s) ds \right]^2 E(\varepsilon_i, p) dp \approx \begin{cases} 24 Sc_i^{-1.9} & \text{for the gas} \\ 12.2 Sc_i^{-1} & \text{for the liquid} \end{cases} \\ \bar{\varphi}_{33i} &= \int_0^\infty \left[ \int_0^P \bar{\varphi}(s) ds \right]^2 E(\varepsilon_i, p) dp \approx \begin{cases} 0.326 Sc_i^{-1.69} & \text{for the gas} \\ 0.035 Sc_i^{-1.1} & \text{for the liquids} \end{cases} \\ & i = 1, \dots, n \end{aligned} \quad (13)$$

### Kinetics of Multicomponent Mass Transfer

The multicomponent mass transfer mean rate for a plate with a length "L" can be determined from the average mass flux:

$$J_i = \mathcal{M}_i k_i (c_i^* - c_{0i}) = \frac{1}{L} \int_0^L I_i dx, \quad i = 1, \dots, n, \quad (14)$$

where the mass flux has a convective and diffusive component:

$$\begin{aligned} I_i &= -\mathcal{M}_i D_i \left( \frac{\partial c_i}{\partial y} \right)_{y=0} + \mathcal{M}_i (c_i v)_{y=0} = \\ &= -\mathcal{M}_i D_i \left[ \left( \frac{\partial c_i}{\partial y} \right)_{y=0} + \frac{\mathcal{M}}{\varrho_0} \alpha_i \left( c_i \frac{\partial c}{\partial y} \right)_{y=0} \right], \quad i = 1, \dots, n, \end{aligned} \quad (15)$$

An expression for the Sherwood number can be obtained directly from (3), (14) and (15):

$$Sh_i = \frac{k_i L}{D_i} = -Pe^{0.5} \left[ \Psi'_i(0) + \Theta \bar{\varepsilon}_i \frac{c_i^*}{c_i^* - c_{0i}} \Psi''(0) \right], \quad i = 1, \dots, n, \quad (16)$$

where:

$$Pe = \frac{u_0 L}{D}. \quad (17)$$

$\Psi''(0)$  in Equation (16) is determined in [2], while  $\Psi'_i(0)$  ( $i = 1, \dots, n$ ) are determined directly from Equations (4), (6), (9) and (12):

$$\begin{aligned} \Psi'_i(0) &= -\frac{2}{\varepsilon \varphi_{0i}} + \Theta \frac{2\bar{\varepsilon}_i \varphi_{3i}}{\varepsilon \varphi_0 \varphi_{0i}^2} - \Theta^2 \left[ \frac{2\bar{\varepsilon}_i \varphi_{3i}}{\varphi_0^2 \varphi_{0i}^2} \left( \frac{\varphi_3}{\varphi_0} + \frac{\bar{\varepsilon}_i \varphi_{3i}}{\varepsilon \varphi_{0i}} \right) - \frac{\bar{\varepsilon}_i^2 \varphi_{33i}}{\varepsilon \varphi_0^2 \varphi_{0i}^2} - \frac{\bar{\varepsilon}_i \bar{\varphi}_{33i}}{\varepsilon^2 \varphi_0^2 \varphi_{0i}^2} \right], \\ & i = 1, \dots, n \end{aligned} \quad (18)$$

Here, as in [2], the feasible values of  $\Theta$ , for which Equation (18) holds, can be obtained. For example, for  $\varepsilon = 20$  and  $\varepsilon_i = 0$ ,  $\Theta \leq 0.033$ .

The comparison of the result for the dimensionless diffusive flow, obtained from the asymptotic theory, with numerical theory data  $\Psi'_{iN}(0)$ , obtained in [7], is presented in *Tables 1* and *2*. It displays the good accuracy of the asymptotic theory.

Table 1

$\varepsilon = 1,$	$\alpha_i = 2,$	$\bar{\varepsilon}_i = 2$
$\Theta$	$-\Psi'_{iN}(0)$	$-\Psi'_i(0)$
0	0.845	0.847
+0.1	0.762	0.765
-0.1	0.943	0.945
+0.2	0.690	0.700
-0.2	1.060	1.061
+0.3	0.633	0.652
-0.3	1.212	1.190

Table 2

$\varepsilon = 20,$	$\alpha_i = 0.5,$	$\bar{\varepsilon}_i = 10$
$\Theta$	$-\Psi'_{iN}(0)$	$-\Psi'_i(0)$
0	0.198	0.194
+0.03	0.167	0.169
-0.03	0.275	0.250
0.05	0.154	0.170
0.10	0.132	0.234

### Conclusion

The results obtained demonstrate that intensive mass exchange of one of the components, from the volume towards the solid surface ( $\Theta < 0$ ), also increases the rate of mass transfer for all components. The differences in the rates result only from differences in the diffusive constants. The change of direction of the intensive mass exchange (from the solid surface towards the volume,  $\Theta > 0$ ) leads to a decrease in the mass transfer rate. These effects do not change with a change in the direction of the mass exchange of the components, whose concentration gradients are not big enough.

The relationship for the multicomponent mass exchange rate, accurate to the second-order approximation for the  $\Theta$  parameter, can be successfully used for solving different chemical engineering problems.

## REFERENCES

1. BOYADJIEV, CHR. and VULCHANOV, N.: *C. r. Acad. Bulg. Sci.* 1987, 40 (11), 35-38.
2. BOYADJIEV, CHR. and TOSCHEV, E.: *Hung. J. Ind. Chem.* 1989, 17 (3) 457-463.
3. BOYADJIEV, CHR. and VULCHANOV, N.: *C. r. Acad. Bulg. Sci.* 1988, 41 (10), 49-52.
4. BOYADJIEV, CHR.: *Hung. J. Ind. Chem.*
5. SHERWOOD, T. K., PIGFORD, R. L. and WILKE, C. R.: *Mass Transfer*, McGraw-Hill. New York. 1975. pp. 76-82.
6. FRANK-KAMENETSKII, D. A.: *Diffusion and Heat Transfer in Chemical Kinetics*. Mir. Moscow. 1987. pp. 189-209.
7. BOYADJIEV, CHR. and VULCHANOV, N.: *Chem. Eng. Sci.*, in press.

## MODEL STUDIES OF CATALYTIC HYDROGENOLYSIS OF N-BUTYLAMINE OVER ZEOLITE AND ALUMINA CATALYSTS

Z. SARBAK

(Wydział Chemii, Uniwersytet im Adama Mickiewicza, 60-780 Poznań, Poland)

Received: May 2, 1989.

The catalytic decomposition of *n*-butylamine absorbed on the examined catalysts proceeds in several different directions. This seems to suggest that it is the catalysts that exhibit polyfunction properties, in particular, destructive hydrogenation, deamination and dehydrogenation.

As follows from the performed studies, stronger Brønsted acid centres become poisoned already in the initial period of the reaction. On the other hand, gamma alumina reaches activity comparable with that of H-mordenite, which would suggest the involvement of Lewis acidic centres.

It seems that in the case of zeolites of X-type modified with  $\text{Co}^{2+}$  and  $\text{Ni}^{2+}$  ions, their high activity may be due to generation of new Lewis acidic centres. They may be formed on the introduced transition metal ions.

### Introduction

The catalytic decomposition of aliphatic amines by hydrogenolysis is not only of practical importance, but also a theoretical one. The investigation of the decomposition is connected with studies of that mechanism governing catalytic hydrodenitrogenation of nitrogen organic compounds occurring in carbo- an petrochemicals products.

Aliphatic amines can be relatively easy hydrogenolyzed and do not require high hydrogen pressure. On the other hand, they are found as intermediate products of hydrodenitrogenation of nitrogen heterocyclic compounds [1-3]. Therefore, the investigations of *n*-butylamine hydrogenolysis in the presence of zeolites of faujasite type, modified by nickel and cobalt ions were carried out.

## Experimental

The studies on the catalytic activity were carried out in a flow microreactor at the temperature of 400° C where 0.3000 g of catalyst was placed. Carrier gas, i.e. purified and dried hydrogen, flowed with the flow rate of 10 cm<sup>3</sup> min<sup>-1</sup> through a thermostated evaporator containing *n*-butylamine.

Then the mixture of hydrogen and *n*-butylamine flowed through a layer of a catalyst covered with 1 cm<sup>3</sup> of quartz wool. The reaction products formed and unreacted *n*-butylamine were separated chromatographically in a gas chromatograph GCHF 18.3 at the temperature of 90° C using 2m column with Chromosorb W AW and 10% Carbowax 20M. The samples for GC analysis were taken periodically using a sampling loop. The first sample was taken 5 minutes after the reaction started, the others every 15 minutes for 4 hours.

## Results and Discussion

The findings showed that in the experimental conditions, the main reaction products were butane, ammonia and trace amounts of butenes and butyronitrile.

However, dibutylamine, *N*-butylidenobutylamine and butylidenoimine were not found to occur, which contradicts the results reported elsewhere [4-6] concerning the deamination reaction on alumina, which was carried out in the atmosphere of neutral gas.

On the basis of the comparison of *n*-butylamine conversion with the reaction time for the investigated zeolite catalysts and for gamma-alumina, a considerable difference between cation-faujasite forms and H-mordenite form were found to occur (*Fig. 1*).

The latter form is rapidly deactivated and then it catalyses the investigated reaction on a stable, but relatively low level, whereas the nickel and cobalt forms of zeolite X undergo a considerably smaller deactivation than the previous one and after a relatively short time they regain their catalytic properties. There is *n*-Butylamine conversion on gamma-alumina as a catalyst changes in a different way. Here, conversion increases initially and then is stabilized.

Different catalytic behaviour of alumina in *n*-butylamine hydrogenolysis is probably due to the lack of Brönsted acid centres on its surface.

It seems correct to assume that in the case of zeolites, strong proton donor centres will, first of all, undergo poisoning by *n*-butylamine, which will bring about a decrease in catalytic activity. Poisoning of acid centres can also be proved by the fact that butenes formed during the reaction do not undergo polymerization. This is indicated by the lack of colour change of the white mordenite, which, because of the channel system of its pores, is sensitive to this kind of poisoning [7].

Zeolites of type X modified by nickel and cobalt cations relatively quickly regain their activity after initial loss of it. Such untypical changes must be connected with the presence of other active centres than acid Brönsted centres.

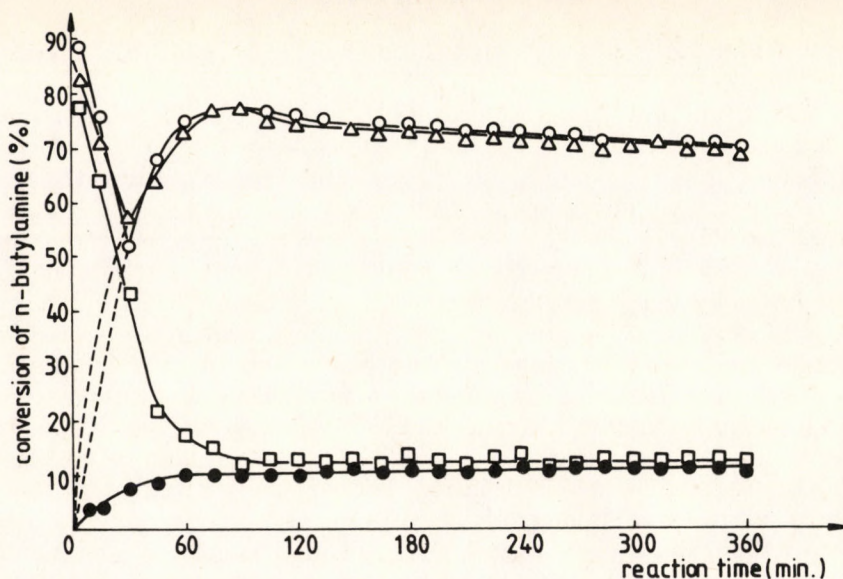


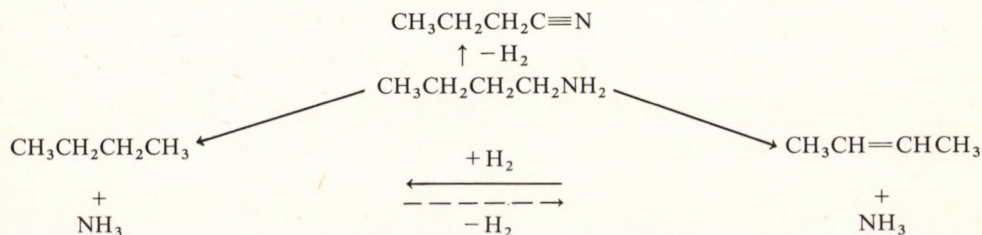
Fig. 1.

Conversion of n-butylamine over:  $\odot$  - NaNiX zeolite,  $\Delta$  - NaCoX zeolite,  $\square$  - H-mordenite and  $\bullet$  - gamma alumina.

This may be caused by transition metal cations. The above conclusion follows from the fact that no activity is observed for the sodium form of zeolite X in n-butylamine hydrogenolysis.

At this point, another problem should be considered - why do the latter active centres show their catalytic action after the poisoning of the mentioned acid centres. The considered centres seem to be not competitive enough, in the first reaction stage, with respect to the Brönsted acid centres. This may result from a considerably greater affinity of amine and ammonia to strong Brönsted acid centres than e.g. to cations of transition metals, which begin to play an important role, while the first ones are poisoned.

On the basis of the above results, it can be claimed that n-butylamine hydrogenolysis is the main reaction, which takes place apart from dehydrogenation, hydrogenation and reagent deamination on basic and acidic centres, which can be schematically presented:



(dashed line indicates that the reaction direction noted on the above scheme is also possible).

It follows from the presented data that the investigated catalysts are of polyfunctional character, which means that both acidic centres and centres responsible for dehydrogenation and hydrogenation, mainly a destructive one, take part in n-butylamine decomposition.

At the first stage, only the action of the acidic Brönsted centres can be observed. As it is known acidic centres show great affinity to strong basic amine and ammonia molecules, and thus are poisoned as the reaction proceeds.

From the observations based on the catalytic action of gamma-alumina (support of Lewis acidic centres) and H-mordenite (support of strong Brönsted acidic centres and Lewis acidic centres) it follows that Lewis acidic centres are responsible for n-butylamine decomposition in the range of stabilized activity.

However, the observed decrease in activity at the beginning of the reaction should be connected with the Brönsted acidic centres deactivation. On the example of zeolite X containing cations of transition metals we can observe a definite synergetic influence of these ions on the high activity of catalysts in the reaction considered. It seems that the above mentioned cations can play the role of Lewis acidic centres.

#### REFERENCES

1. ZIELIŃSKI, S. and SARBAK, Z.: *Przem. Chem.* 1983, 62,262.
2. ZIELIŃSKI, S. and SARBAK, Z.: *Przem. Chem.* 1983, 62,323.
3. SARBAK, Z.: *React. Kinet. Catal. Lett.* 1979, 12,265.
4. BREY, W.S. and COBBLEDICK, J.C.: *Ind. Eng. Chem.* 1959, 51,1031.
5. CATRY, J.P. and JUNGERS, J.C.: *Bull. Soc. Chim. Fr.* 1964, 2317.
6. TOMIDA, M., TANAKA, M., IWASAWA, Y. and OGASAWARA, S.: *Chem. Lett.* 1973, 375.
7. KARGE, H.G. and LADEBECK, J.: *Acta Phys. Chem.* 1978, 24,161.

## NEW DERIVATIVES OF DICHLOROBENZENE SULPHONANILIDES FOR PEST CONTROL IN MAIZE

F. I. EL-DIB, M. A. SALAMA, and A. Y. EL-SHARKAWY\*

(Petrochemicals Department, Petroleum Research Institute, Nasr City, Cairo, Egypt.)

\* Plant Pathology Institute, Agriculture Research Center, Cairo, Egypt.)

Received: July 12, 1989

The development of *s*-ethyl (and benzyl-isothiuronium) salts of some dichlorobenzene sulphonanilides is reported. The prepared compounds were examined as fungicides against *Helminthosporium turcicum* (cause of leaf-blight in maize), and *Cephalosporium maydis* (cause of late-wilt disease in maize). The most potent agents in this series were those bearing a nitro group in the anilide moiety. The effects of various structural modifications on the fungicidal activity are discussed in detail.

### Introduction

In the search for new pest control agents, it was found that isothiuronium salts have proved to be powerful fungicides [1-3]. Recently, BADAWI et al., [4] synthesized useful antibacterial and antifungal isothiuronium salts derived from *n*-butyl-isothiuronium bromide, isobutyl-isothiuronium bromide, ethylene-1,2-bis-isothiuronium bromide and propylene-1,3-isothiuronium bromide.

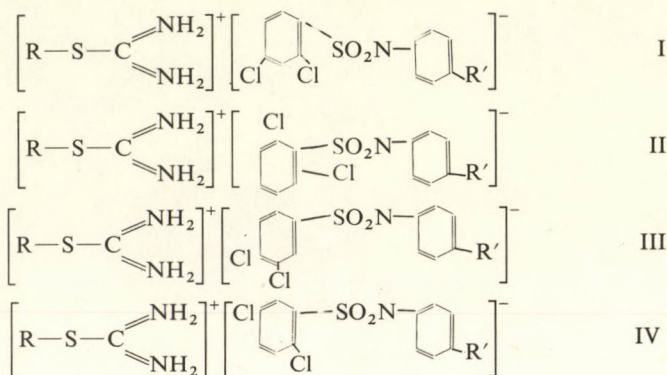
On the other hand, it was well established that compounds having the moiety  $\text{—SO}_2\text{NH—}$  have high biochemical significance as bactericidal, fungicidal, as well as insecticidal activities [5-8].

In view of the previously mentioned biological facts, the present investigation was directed towards the synthesis of a series of some *s*-alkylisothiuronium salts of dichlorobenzene sulphonanilides. It seemed possible that a combination of both *s*-alkylisothiuronium and sulphonanilide moieties in one molecule might give a product, which could behave as a fungicide.

### Discussion

Interaction between 2,4-, 2,6-, 3,4- and 3,5-dichlorobenzene-1-sulphon 4-chloroanilide and *s*-alkylisothiuronium bromide (benzyl, ethyl), yielded the corresponding isothiuronium salts I<sub>a,c</sub>, II<sub>a,c</sub>, III<sub>a,c</sub> and IV<sub>a,c</sub> (Table I).

The isothiuronium salts I<sub>b,d,e</sub>, II<sub>b,d,e</sub>, III<sub>b,d,e</sub> and IV<sub>b,d,e</sub> (9) were similarly prepared:



- I, II, III and IV a: R = C<sub>6</sub>H<sub>5</sub>CH<sub>2</sub>, R' = Cl  
 b: R = C<sub>6</sub>H<sub>5</sub>CH<sub>2</sub>, R' = CH<sub>3</sub>  
 c: R = C<sub>2</sub>H<sub>5</sub>, R' = Cl  
 d: R = C<sub>2</sub>H<sub>5</sub>, R' = CH<sub>3</sub>  
 e: R = C<sub>2</sub>H<sub>5</sub>, R' = NO<sub>2</sub>

Table I

S-Alkylisothiuronium Salts of Dichloro-benzene-1-Sulphon-4'-chloroanilide

Comp. No.	M.P. °C	Formula	Analysis	
			N	Calc./Found % S
I <sub>a</sub>	104-5	C <sub>20</sub> H <sub>18</sub> Cl <sub>3</sub> N <sub>3</sub> O <sub>2</sub> S <sub>2</sub>	8.36	12.74
			8.72	12.62
II <sub>a</sub>	121-2	C <sub>20</sub> H <sub>18</sub> Cl <sub>3</sub> N <sub>3</sub> O <sub>2</sub> S <sub>2</sub>	8.36	12.74
			8.00	13.21
III <sub>a</sub>	112-3	C <sub>20</sub> H <sub>18</sub> Cl <sub>3</sub> N <sub>3</sub> O <sub>2</sub> S <sub>2</sub>	8.36	12.74
			7.90	12.36
IV <sub>a</sub>	98-9	C <sub>20</sub> H <sub>18</sub> Cl <sub>3</sub> N <sub>3</sub> O <sub>2</sub> S <sub>2</sub>	8.36	12.74
			8.81	13.00
I <sub>c</sub>	90-1	C <sub>15</sub> H <sub>16</sub> Cl <sub>3</sub> N <sub>3</sub> O <sub>2</sub> S <sub>2</sub>	9.54	14.53
			10.00	15.00
II <sub>c</sub>	101-3	C <sub>15</sub> H <sub>16</sub> Cl <sub>3</sub> N <sub>3</sub> O <sub>2</sub> S <sub>2</sub>	9.54	14.53
			9.92	14.27
III <sub>c</sub>	114-5	C <sub>15</sub> H <sub>16</sub> Cl <sub>3</sub> N <sub>3</sub> O <sub>2</sub> S <sub>2</sub>	9.54	14.53
			9.75	14.86
IV <sub>c</sub>	88-9	C <sub>15</sub> H <sub>16</sub> Cl <sub>3</sub> N <sub>3</sub> O <sub>2</sub> S <sub>2</sub>	9.54	14.53
			9.82	14.35

Element analysis and infrared data were in accordance with the proposed structures. Thus, the infrared spectra of these compounds showed absorption bands at wavelengths in  $\text{cm}^{-1}$ : 1490 for 1,4-disubstituted, 1,2,4-, 1,2,6- and 1,3,5-trisubstituted aromatic nucleus, 840 for C—Cl aromatic, 1356 and 1180 for  $\text{SO}_2\text{—N}$ , 1315 for C— $\text{NO}_2$  and 3310 for —N—H.

The antifungal activities of the prepared compounds were tested against *Helminthosporium turcicum* (cause of leaf-blight in maize) and *cephalosporium maydis* (cause of late-wilt disease in maize). The compounds showed similar activities against both fungi (*Table 2*).

*Table 2*

Activity of S-Alkylisothiuronium Salts of Dichlorobenzene-1-Sulphonanilides at 500  $\mu\text{g/ml}$

Comp. No.	Growth diameter <i>Helminthosporium turcicum</i>	Growth diameter <i>cephalosporium maydis</i>
I <sub>a</sub>	+++	+++
II <sub>a</sub>	+++	+++
III <sub>a</sub>	+++	+++
IV <sub>a</sub>	++	++
I <sub>b</sub>	+++	+++
II <sub>b</sub>	+++	+++
III <sub>b</sub>	+	+
IV <sub>b</sub>	++	++
I <sub>c</sub>	+++	+++
II <sub>c</sub>	+++	+++
III <sub>c</sub>	++	++
IV <sub>c</sub>	+++	+++
I <sub>d</sub>	++	++
II <sub>d</sub>	+++	+++
III <sub>d</sub>	+++	+++
IV <sub>d</sub>	++	++
I <sub>e</sub>	—	—
II <sub>e</sub>	—	—
III <sub>e</sub>	—	—
IV <sub>e</sub>	+	+

Control plate:	high growth	+++
Fungicide plate:	high growth	+++
Fungicide plate:	moderate growth	++
Fungicide plate:	little growth	+
Fungicide plate:	No growth	—

Regarding structure-activity relationship, it was found that the effect of the position of the chlorine atoms on fungicidal activity was in the order 3,4-isomer = 3,5-isomer > 2,4-isomer > 2,6-isomer. On the other hand, it was found that thiuronium salts bearing — $\text{NO}_2$  group in the anilide ring gave higher activities than those with — $\text{CH}_3$  group, while those with Cl atom showed lower

toxicities. It was clear from the data obtained that the extent of modification of fungitoxic effect was related to the size of the positive ion, in other words, benzyl > enthyl.

It could be concluded that increasing substituent electronegativity was accompanied by increasing fungicidal activity. The superiority of the nitro-substituted compounds attests to this.

## Experimental

### *Anilides of Dichlorobenzene Sulphonic Acids*

Four isomers of dichlorobenzene sulphonyl chlorides (3,5-, 2,6-, 2,4- and 3,4-dichlorobenzene sulphonyl chlorides) were converted to the corresponding substituted anilides, dichlorobenzene-1-sulphon-toluidide, dichlorobenzene-1-sulphon-nitroanilide and dichlorobenzene-1-sulphon-chloroanilide [6].

### *S-Alkyl Isothiuronium Salts of Dichlorobenzene-1-Sulphonanilides*

To each of the dichlorobenzene-1-sulphon-toluidide, dichlorobenzene-1-sulphon-nitroanilide and dichlorobenzene-1-sulphon-chloroanilide (3.2 g, 3.5 g and 3.4 g respectively), 5 ml · 10% NaOH was added and the mixture was warmed on a water-bath till dissolution, some water was added when necessary, then a solution of s-alkyl (ethyl or benzyl) isothiuronium bromide [10] was added (2 g/3 ml water) while cooling and shaking. The formed precipitate was filtered and recrystallized from aqueous ethanol where compounds I<sub>a,c</sub>-IV<sub>a,c</sub> were obtained (yields 68-81%) (Table 1). Similarly, compounds I<sub>b,d,e</sub>-IV<sub>b,d,e</sub> were prepared.

### *Antifungal Activities of the Prepared Compounds*

Food poison technique was employed [11] to test the prepared compounds I-IV. Non solidified potatodextrin agar (P.D.A.), medium in a 100 ml flask were poisoned at 500 µg/ml of the tested compounds. The poisoned medium was poured in sterile petri-dishes and allowed to solidify. Each dish was inoculated with a 5 mm diameter disk of inoculum removed from a 5 day old culture of the fungus (*Helminthosporium turcicum* and *cephalosporium maydis*). Treatments were replicated 5 times and the plates were incubated at 28 °C. Untreated medium was used as control. The growth diameter was measured after 5 days. The growth diameter of each plate was estimated with reference to that of the control plate as follows (Table 2).

## REFERENCES

1. EL-NAWAWY et al.: Alex. J. Agri. Res., 1960, 8 (1), 277
2. EL-NAWAWY et al.: Alex. J. Agri. Res., 1963, 11 (1), 189
3. EL-NAWAWY et al.: Alex. J. Agri. Res., 1968, 16 (1), 261
4. BADAWI, A. M., SELIEM, R., HAROUN B. and SOLIMAN, H.: Oriental J. Chem., 1988, 4, 107
5. MARIE, A. et al.: Bull. N.R.C., Egypt, 1979, 4, 407
6. MAREI, A. et al.: Bull. N.R.C., Egypt, 1980, 5, 127
7. CREMLYN, R. J.: J. Chem. Soc., 1962, 2133
8. RUDD-JONES: Outlook on Agric. 1956, 1, 111
9. SALAMA, M. A. and EL-DIB, F. I.: 3rd. Egypt. Congress of Chemical Engineers, Cairo, March 1988.
10. URQUHART, G. G. et al.: Org., Synth. 1941, 21, 36
11. SHARVELLE, E. G.: Laboratory testing of fungicide in the nature and use of modern fungicides, Burgess Publish Co., U.S.A., 1961. Chapter 16.



## PRODUCTION OF MOTOR FUELS BY PYROLYSIS OIL HYDROCRACKING UNDER SEVERE CONDITIONS II.

L.T. HUNG., GY. GÁRDOS, and T. KUN SZABÓ,

(Institute of Hydrocarbon and Coal Processing, Veszprém University of Chemical Engineering)

Received: September 5, 1989

The study of resin free pyrolysis oil hydrocracking was extended for more severe hydrogenation conditions. Ni-W/Al<sub>2</sub>O<sub>3</sub> catalyst was also tested alongside the Shell Ni-Mo/Al<sub>2</sub>O<sub>3</sub> and Co-Mo/Al<sub>2</sub>O<sub>3</sub> preparations. The different behaviour of the catalysts was observed which gives a possibility for the flexible modification of the product composition. It was concluded that the hydrocracking of the raw material completely takes place. The product was of aromatic nature, however, olefinic components were not identified, i.e. the product was stable. The optimum parameters of the process were established on the basis of the amount of gasoline fraction.

The hydrocracking of pyrolysis oil was studied under mild conditions in our previous paper [1]. The conditions were selected on the basis of the technological parameters of the existing mild hydrocracking (hydrogenation) plants of refineries with the objective in mind to utilize the available equipment without modification. It was stated that motor fuels can be produced by the hydrocracking of pyrolysis oil, however, it was also concluded that the stability of products, especially light fractions (naphtha) was not adequate [2]. Our goal was to extend these studies for the hydrocracking of pyrolysis oil under severe conditions to produce motor fuels (gasoline) with a higher yield (at relatively low gas yield). Bifunctional catalysts /Co-Mo/Al<sub>2</sub>O<sub>3</sub>, Ni-Mo/Al<sub>2</sub>O<sub>3</sub> and Ni-W/Al<sub>2</sub>O<sub>3</sub> made by Shell were used for the experiments.

### Experimental

The hydrocracking experiments were carried out in a fixed bed reactor (Fig. 1), which is suitable for the activation of the catalysts and for the determination of the optimum parameters (pressure, temperature, liquid load, and hydrogen-hydrocarbon ratio) of the reaction. 20 cm<sup>3</sup> of the catalyst was charged into the reactor and used for the experiments.

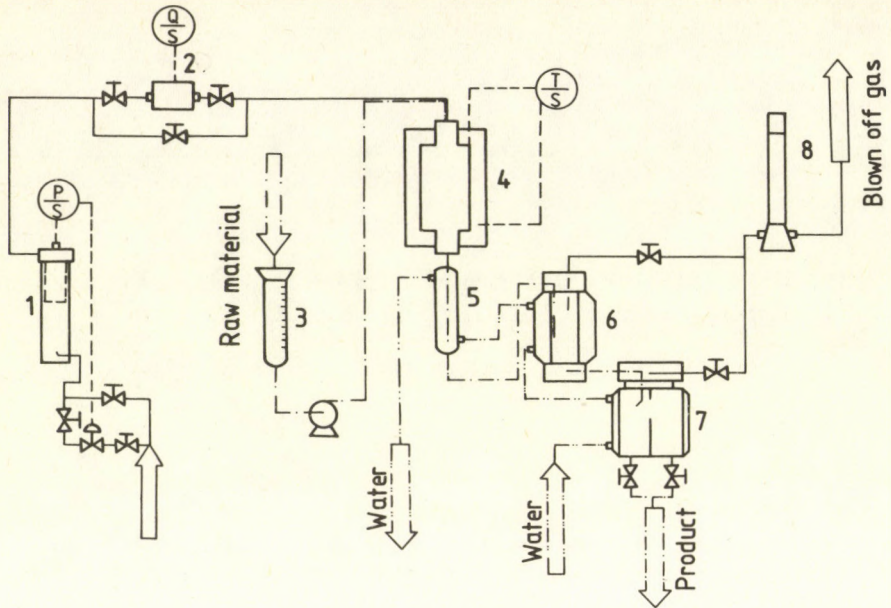


Fig. 1.  
Scheme of the experimental apparatus.

Table 1.

Parameters of the optimizing experiments

Experiment No.	Temperature °C	Pressure bar	H/CH molar ratio	Liquid load $\text{cm}^3/\text{cm}^3 \cdot \text{h}$
1	450	125	40	1.25
2	450	125	40	0.75
3	450	125	30	1.25
4	450	75	40	1.25
5	425	100	35	1.00
6	400	125	40	1.25
7	450	125	30	0.75
8	450	75	40	0.75
9	400	125	30	1.25
10	425	100	35	1.00
11	450	75	30	1.25
12	400	125	40	0.75
13	400	75	40	1.25
14	450	75	30	0.75
15	425	100	35	1.00
16	400	125	30	0.75
17	400	75	40	0.75
18	400	75	30	1.25
19	400	75	30	0.75
20	425	100	35	1.00

The pretreatment of the catalysts was carried out according to the Shell specifications and on the basis of our previous experience [3]. After drying, the catalysts were reduced with hydrogen and were sulphided with a solution of 2-methyl thiophene (1.0 m/m%) and toluene. After the stabilization of the catalysts (constant crack gas composition) the experimental programme was commenced.

The experimental programme was developed on the basis of the available experience, considering the severe reaction condition [4].

The experimental programme permitted the investigation of the effect of the technological parameters on the hydrocracking of the pyrolysis oil and the determination of the optimum parameters on the basis of several experiments [5].

The check measurements (No.5, 10, 15, 20) provided information on the stability of the catalysts. The programme, consisting of 20 experiments, is outlined in *Table 1*.

The test and calculating methods given in our previous paper [1] were used for the qualification of the products. The fractional composition of the products was determined with fractionation using a Vigreux-adaptor. The yields of the fractions in mass percent related to the feed were calculated taking the gas yield into consideration.

The change of the fractional composition ( $\Delta$  m/m%) can be calculated on the basis of the mass of light (i.b.p., e.b.p.: 180° C), medium (i.b.p.: 180, e.b.p.: 280° C) heavy (i.b.p.: 280, e.b.p.: 350° C) residual (i.b.p.: 350° C, e.b.p.) cuts in the feed and in the product [6].

i.b.p.: initial boiling point

e.b.p.: end boiling point

## Results and Discussions

The experimental results obtained on the catalysts tested are given in *Tables 2-4*. The corresponding data of the raw material (partially resin free pyrolysis oil) are also given (serial No.0) to help the comparison.

On the basis of the experimental data it can be concluded that both three catalysts exhibited nearly identical results, therefore, the investigation of the effect of parameters on the hydrocracking of pyrolysis oil and the determination of the optimum parameters were carried out on a selected catalyst. The Co-Mo/ $\text{Al}_2\text{O}_3$  catalyst was chosen for the discussion (the differences between the catalysts will be dealt with later).

It can be seen from *Table 2* that all the liquid products exhibited lower densities than of the raw material. The extent of the differences depends on the process parameters. The temperature and the pressure have the greatest effect. The density of the product is lower at higher temperature or pressure if the other parameters are identical. The true boiling point (TBP) curve of the product mixture is below that of the raw material and its position depends on the reaction temperature showing its effect on the hydrocracking. It can be stated

Table 2

The results of the experiments carried out over Co-Mo/Al<sub>2</sub>O<sub>3</sub>

Experiment No.	Casyield %	Density d <sub>4</sub> <sup>20</sup>	Iodine number g <sub>1/2</sub> /100 g	TBP data, °C						MABP °C	M <sub>A</sub>	C/H ratio	K <sub>w</sub>	Change of the fractional composition, Δm/m %				
				i.b.p.	10%	30%	50%	70%	90%					e.b.p.	Light	Medium	Heavy	Residue
0	—	0.998	32.00	(85)	163	209	235	264	317	358	230	158	9.8	9.7	14	61	21	4
1	4.5	0.895	1.10	(15)	83	148	193	213	248	287	169	129	8.0	10.3	+24	-5	-19	-4
2	7.0	0.891	1.00	(20)	81	139	191	216	255	297	167	129	7.9	10.3	+26	-11	-18	-4
3	4.5	0.905	1.05	(15)	84	150	198	225	271	294	175	132	8.1	10.2	+25	-12	-14	-4
4	2.0	0.945	0.90	(35)	101	182	210	234	276	318	190	137	8.8	9.9	+12	-1	-9	-4
5	3.0	0.929	0.75	(35)	111	176	212	239	288	327	195	143	8.5	10.1	+14	-7	-6	-4
6	3.6	0.931	0.60	(30)	123	185	218	246	293	300	204	149	8.5	10.2	+10	-6	-4	-4
7	3.5	0.883	1.10	(25)	73	134	184	216	253	291	162	126	7.8	10.4	+30	-10	-19	-4
8	4.0	0.939	1.00	(30)	103	175	206	229	273	319	188	136	8.7	10.0	+14	-5	-9	-4
9	0.5	0.934	0.40	(35)	114	184	219	242	290	321	200	145	8.6	10.1	+12	-3	-5	-4
10	4.0	0.928	0.84	(40)	110	176	211	237	285	324	194	142	8.5	10.1	+14	-6	-8	-4
11	2.5	0.945	0.90	(15)	112	180	212	237	285	322	196	141	8.8	10.0	+13	-5	-6	-4
12	3.5	0.934	0.50	(35)	114	180	215	240	289	318	198	144	8.6	10.1	+13	-6	-6	-4
13	2.0	0.952	0.60	(25)	133	192	221	246	304	326	210	150	8.9	10.0	+10	-6	-1	-4
14	6.0	0.932	1.00	(3)	84	162	204	230	277	311	179	131	8.6	10.0	+17	-10	-9	-4
15	2.5	0.931	0.85	(30)	111	179	208	230	279	311	193	141	8.5	10.1	+13	-3	-9	-4
16	2.9	0.924	0.65	(40)	116	178	212	238	290	317	197	145	8.4	10.2	+14	-7	-6	-4
17	3.0	0.945	0.65	(15)	128	190	215	235	286	318	203	146	8.8	10.0	+10	-4	-7	-4
18	1.5	0.951	0.60	(40)	140	194	220	243	299	330	211	151	8.9	10.0	+12	-5	-3	-4
19	2.0	0.944	0.75	(10)	134	189	215	238	285	319	205	148	8.7	10.0	+13	-6	-5	-4
20	0.5	0.938	0.90	(35)	113	197	214	237	288	319	196	143	8.6	10.1	+14	-5	-5	-4

Table 3

The results of the experiments carried out over Ni-MO/Al<sub>2</sub>O<sub>3</sub>

Experiment No.	Gasyield %	Density d <sub>4</sub> <sup>20</sup>	Iodine number g <sub>1/2</sub> /100 g	TBP data, °C						MABP °C	M <sub>A</sub>	C/H ratio	K <sub>w</sub>	Change of the fractional composition, Δm/m%				
				i.b.p.	10%	30%	50%	70%	90%					e.b.p.	Light	Medium	Heavy	Residue
0	—	0.998	32,00	(85)	163	209	235	264	317	358	230	158	9.8	9.7	14	61	21	4
1	3.0	0.904	0.90	(35)	87	150	197	227	262	293	175	132	8.1	10.3	+24	-6	-17	-4
2	6.5	0.887	0.90	(30)	82	141	188	216	251	294	168	130	7.8	10.4	+27	-10	-20	-4
3	1.0	0.901	0.95	(30)	84	150	195	222	261	282	173	131	8.1	10.3	+26	-10	-13	-4
4	2.5	0.936	0.80	(20)	102	169	209	237	284	304	190	138	8.7	10.0	+15	-7	-7	-4
5	4.5	0.920	0.70	(25)	107	170	206	233	283	311	190	141	8.4	10.2	+17	-8	-10	-4
6	2.5	0.935	0.55	(15)	121	183	212	239	290	311	200	145	8.6	10.1	+9	-2	-5	-4
7	3.5	0.890	1.00	(30)	79	140	188	216	254	302	166	128	7.9	10.4	+28	-10	-18	-4
8	4.0	0.935	0.95	(30)	100	167	205	230	274	317	186	135	8.7	10.0	+17	-8	-10	-4
9	1.0	0.936	0.60	(10)	136	192	215	238	291	320	206	150	8.6	10.1	+10	-1	-6	-4
10	3.5	0.928	0.70	(30)	107	169	210	235	285	331	192	140	8.5	10.1	+17	-9	-8	-4
11	4.0	0.937	0.80	(25)	99	168	205	228	271	316	185	135	8.7	10.0	+15	-7	-9	-4
12	2.0	0.946	0.45	(10)	133	189	214	240	292	325	205	148	8.8	10.0	+12	-5	-5	-4
13	0.5	0.951	0.55	(10)	129	187	221	249	306	327	208	149	8.9	10.0	+9	-5	0	-4
14	1.0	0.934	0.95	(25)	110	173	211	237	284	315	194	141	8.6	10.1	+18	-8	-8	-4
15	1.0	0.934	0.70	(30)	114	176	211	235	286	317	195	142	8.6	10.1	+16	-6	-7	-4
16	1.5	0.952	0.55	(5)	129	184	211	235	287	320	202	144	8.9	9.9	+11	-2	-6	-4
17	0.5	0.954	0.60	(30)	134	191	216	241	292	331	207	147	8.9	10.0	+11	-4	-4	-4
18	0.5	0.949	0.65	(40)	126	187	220	249	303	329	207	148	8.8	10.0	+10	-6	0	-4
19	2.5	0.942	0.65	(40)	118	179	214	241	297	316	200	144	8.8	10.0	+13	-9	-3	-4
20	1.0	0.936	0.75	(30)	115	173	210	235	285	321	195	142	8.6	10.0	+16	-7	-7	-4

Table 4.

The results of the experiments carried out over Ni-W/Al<sub>2</sub>O<sub>3</sub>

Experiment No.	Gasyield %	Density d <sub>4</sub> <sup>20</sup>	Iodine number g <sub>1/2</sub> /100 g	TBP data, °C							MABP °C	M <sub>A</sub>	C/H ratio	K <sub>w</sub>	Change of the fractional composition, Δm/m %			
				i. b. p.	10%	30%	50%	70%	90%	e. b. p.					Light	Medium	Heavy	Residue
0	—	0.998	32.00	(85)	163	209	235	264	317	358	230	158	9.8	9.7	14	61	21	4
1	4.5	0.917	1.10	(15)	105	167	203	224	260	285	185	131	8.3	10.1	+20	-6	-15	-4
2	6.5	0.890	1.10	(25)	86	147	187	214	247	274	169	123	7.8	10.3	+27	-8	-21	-4
3	4.5	0.920	1.05	(20)	107	169	206	233	273	299	189	133	8.3	10.1	+21	-10	-12	-4
4	6.0	0.929	1.05	(25)	102	167	206	232	281	316	188	131	8.5	10.0	+15	-9	-8	-4
5	4.0	0.930	1.00	(10)	118	179	210	231	277	303	196	136	8.5	10.1	+13	-3	-10	-4
6	4.0	0.934	0.45	(20)	127	185	215	238	286	319	203	141	8.5	10.1	+9	-2	-7	-4
7	6.0	0.895	1.05	(25)	87	148	188	215	249	280	170	124	7.9	10.3	+27	-8	-21	-4
8	6.0	0.932	1.00	(35)	99	162	197	224	258	290	180	125	8.6	9.9	+18	-5	-15	-4
9	3.5	0.933	0.50	(10)	129	187	215	240	290	323	205	142	8.5	10.1	+10	-4	-5	-4
10	4.0	0.932	1.00	(10)	121	181	211	232	275	299	197	137	8.5	10.1	+12	-3	-9	-4
11	6.0	0.929	1.00	(30)	103	169	207	233	287	326	189	132	8.5	10.0	+14	-8	-7	-4
12	3.0	0.934	0.50	(5)	126	183	213	235	286	324	201	140	8.5	10.1	+10	-2	-7	-4
13	3.5	0.945	0.40	(5)	133	188	222	243	295	322	208	143	8.7	10.0	+9	-6	-3	-4
14	6.0	0.930	0.90	(30)	104	167	203	227	263	289	185	129	8.5	10.0	+17	-5	-15	-4
15	4.0	0.932	1.00	(10)	120	182	212	232	278	303	197	137	8.5	10.0	+11	-1	-10	-4
16	3.0	0.934	0.50	(5)	127	183	214	235	286	324	202	140	8.5	10.1	+11	-4	-6	-4
17	3.0	0.935	0.70	(15)	128	184	215	240	290	327	204	141	8.5	10.1	+10	-2	-7	-4
18	3.5	0.947	0.65	(15)	133	189	223	245	303	334	210	144	8.7	10.0	+7	-4	-2	-4
19	3.0	0.935	0.70	(10)	128	185	215	239	287	320	203	141	8.5	10.1	+9	-2	-6	-4
20	4.0	0.934	1.05	(15)	121	181	213	233	279	304	198	137	8.5	10.1	+12	-2	-10	-4

that the TBP data, mean-average boiling point (MABP) and average molecular mass ( $M_A$ ) are lower than those of the raw material. These changes indicate the occurrence of hydrocracking reactions. The C/H ratio and the Watson characterization factor ( $K_w$ ) are typical data, and these values provide information on the extent of saturation of the molecular structure and on the incorporation of hydrogen into the molecule.

The changes of the fractional composition show that the amount of the light fraction increased significantly in the case of all product mixtures depending on the operational parameters (between 10–30 m/m%). The amount of the light fraction increases unambiguously on increasing the temperature or pressure. The decrease of the liquid load results in the same effect as mentioned above. *Fig. 2* shows the changes of the light fraction in the function of the parameters over Co-Mo/ $Al_2O_3$  catalyst. *Figs. 3* and 4 illustrate the results obtained over

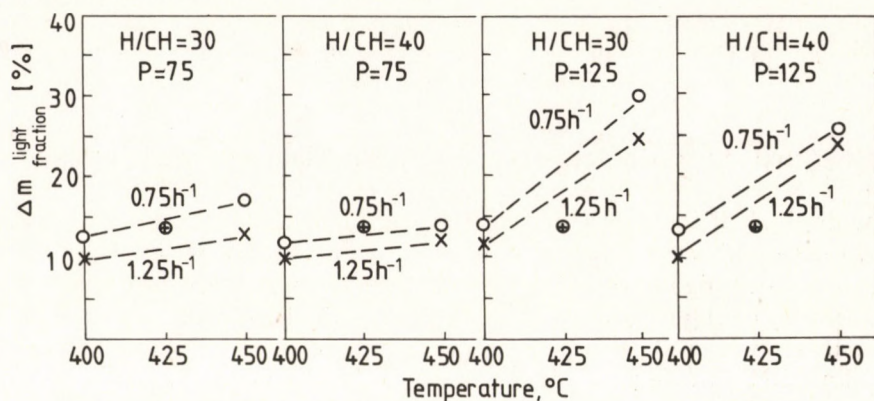


*Fig. 2.*

Change of the amount of the light fraction in the function of parameters of the experimental programme over Co-Mo/ $Al_2O_3$ .

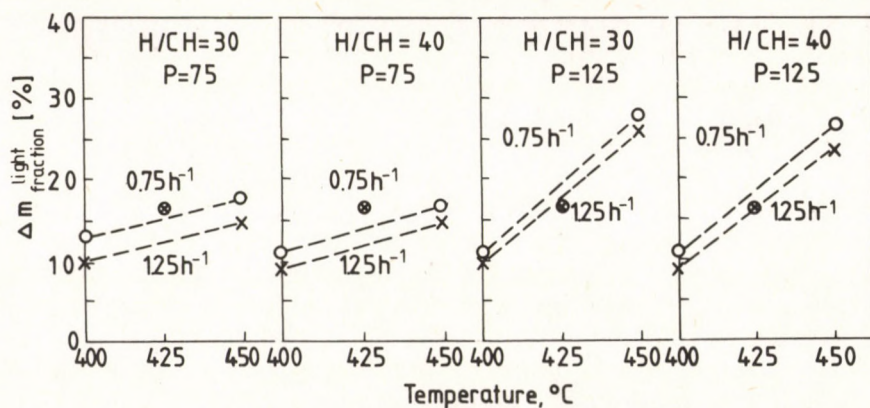


*Fig. 3.*

Change of the amount of the light fraction in the function of parameters of the experimental programme over Ni-Mo/ $Al_2O_3$ .

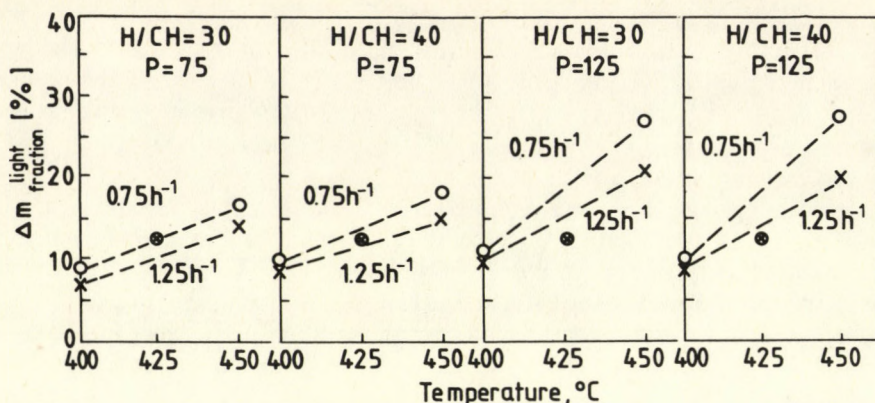


Fig. 4.

Change of the amount of the light fraction in the function of parameters of the experimental programme over Ni-W/Al<sub>2</sub>O<sub>3</sub>.

the other two catalyst preparations (the dashed line indicates the correlating points).

The amount of the light fraction shows an increase with the decrease of the liquid load in all cases: however, the extent of increase is relatively small (2–3 m/m%) for a change of 0.5 h<sup>-1</sup>. The increase of the temperature supports the formation of the light products. The change of the light product formed is still moderate (2–3 m/m%) for a temperature change of 50° C at 75 bar. The increase of the amount of the light product can soon achieve 15 m/m% at higher pressure (125 bar): e.g. the amount of the light fraction is 14 m/m%, which increases to 29 m/m% at 400° C and to 44 m/m% at 450° C. The favourable effect of the application of higher pressure in the case of pyrolysis oil raw material is indicated by the fact that the average point (marked by x) is practically above the lines in the case of the experimental results obtained at lower pressure, while it is below the lines in the case of higher pressure. The amount of the medium fraction decreased by 1–12 m/m% depending on the experimental parameters, which is equal to 2–20 m/m% based on the amount in the feed (= 61 m/m%). The amount of the heavy fraction decreased significantly. Even 90% of its original amount was converted, which was not observed at lower pressures (under mild hydrocracking conditions). The residual cut was completely converted in all experiments.

The iodine numbers of the product mixture show that practically complete hydrogenation occurred during the hydrocracking due to the higher pressure and H/CH ratio compared to the experiments carried out previously. This can result in the higher stability of the fractions formed, and the occurrence of the resin formation is not probable, since the olefin content of the product mixture (calculated on the basis of the iodine numbers) is below 0.3–0.5 m/m%. The raw material (feed) had a dark colour inspite of the carrier gas distillation and contained all the heavy components, which result in the dark colour due to their

chromophore groups. The products formed had a greenish-yellow colour and were transparent. The colour stability of the products was fairly good. Considering the effect of the temperature, it can be stated that on increasing the temperature, the hydrogenation reactions are pressed back only in a slight extent (see experiments No.1-4 and 7-8, respectively) due to the high hydrogen partial pressure.

The experiments carried out at 75,100,125 bar pressures show that the catalysts maintained their higher activity and the saturation of the products with hydrogen was better than in the former cases.

The control measurements (experiments No.5, 10, 15, 20) confirmed the experimental results. The Co-Mo/Al<sub>2</sub>O<sub>3</sub> catalyst maintained its original activity even after 120 hrs on stream.

The following optimum parameters can be given in the case of the Co-Mo/Al<sub>2</sub>O<sub>3</sub> catalyst: temperature: 450° C, H<sub>2</sub> pressure: 125 bar, liquid load: 0.75 cm<sup>3</sup>/cm<sup>3</sup>h, molar ratio of H/CH = 30 (experiment No.7.)

On the basis of the comparison of the three catalysts (Tables, and Figs) it can be stated that good and similar results were obtained.

Since the possible optimum was achieved at experiment No.7 on all the three catalysts, the comparison of the catalysts was mainly performed on the basis of the results of these experiments.

The gas yields were nearly identical on all the catalysts studied. The former statements on the densities and iodine numbers are valid. On the basis of the mean average boiling points, TBP curves and the change of the fractional composition of the products, it can be stated that the formation of the light fraction over the Co-Mo/Al<sub>2</sub>O<sub>3</sub> catalyst is the most selective process. However, the Ni-W/Al<sub>2</sub>O<sub>3</sub> catalyst due to its nature is close to the cracking catalysts compared to the former catalyst. The highest amount of the light fraction was obtained over Co-Mo/Al<sub>2</sub>O<sub>3</sub> catalyst (44 m/m%). Both the heavy fraction and residue were converted over Ni-W/Al<sub>2</sub>O<sub>3</sub> catalyst (experiments No. 2,7).

The data of the TBP curves well illustrate the tendency; the TBP curve of the product obtained over the Co-Mo/Al<sub>2</sub>O<sub>3</sub> catalyst has a greater slope than that of the product obtained over Ni-W/Al<sub>2</sub>O<sub>3</sub>. The Ni-Mo/Al<sub>2</sub>O<sub>3</sub> has an intermediate position between the two former catalysts. This can be explained by the ratio of the hydrogenation activity and acidity of the catalyst and by the acid site distribution [6].

### Conclusions

The results on the hydrocracking of resin free pyrolysis oil under severe conditions can be summarized as follows:

1. All the three catalysts were suitable for the hydrocracking of the pyrolysis oil under laboratory conditions. The Co-Mo/Al<sub>2</sub>O<sub>3</sub> catalyst exhibits the highest selectivity for the light fraction. The Ni-W/Al<sub>2</sub>O<sub>3</sub> catalyst can be used for the hydrocracking of residues and at the same time the amount of the light fraction is also satisfactory. The use of the Ni-W/Al<sub>2</sub>O<sub>3</sub> catalyst is appro-

priate when higher conversion should be achieved or when raw material with higher resin content (with higher end boiling point) should be processed. The catalysts maintained their activities even after a long period of time on stream.

2. The optimum parameters were stated as follows:

temperature: 450°C  
hydrogen pressure: 125 bar  
liquid load: 0,75 cm<sup>3</sup>/cm<sup>3</sup> hr  
H/CH molar ratio: 30

3. The composition of the product mixture is the following on the basis of the fractionation:

light fraction: 40–45 m/m%  
medium fraction: 50–55 m/m%  
heavy fraction: 0–5 m/m%  
residue: 0 m/m%

which indicate significant changes compared to the composition of the raw material (light fraction: 14 m/m%, medium fraction: 61 m/m%, heavy fraction: 21 m/m% and residue: 4 m/m%).

4. The products have high stability; the light fractions have good octane numbers due to their high aromatic hydrocarbon content. These light fractions meet the requirements of commercial utilization, because of the high octane number and good stability, except for the density. These fractions can be used as motor fuel components or aromatic hydrocarbon source.

#### REFERENCES

1. KUN-SZABÓ T., GÁRDOS GY. és SZATMÁRI E.: *MKL* 1989, 14, (4), 166-171.
2. Study on the hydrogenation of pyrolysis oil. Research Report, Veszprém, 1986.
3. "Shell Catalysts", "Shell Hydrotreating Catalysts Presulphiding Procedure". Technical Bull., 1985.
4. ERLEMEIR, R. und MEISENBURG, E.: *Erdöl und Kohle*, 1972, 25, (4), 183-187.
5. ADLER – MAKAROVA – GRANOVSKIJ: Plainrovaine eksperimenta pri poiske optimalnich uslovii, Moscow, Khimiya, 1976.
6. KUN-SZABÓ T.: Production of motor fuel components on the basis of brown coal extracts. Candidate Thesis, Leningrad–Veszprém, 1988.

## EQUILIBRIUM RESTRICTIONS IN METHANOL-TO-GASOLINE CONVERSION

J. KRAMARZ, and A. WYCZESANY

(Instytut Chemii i Technologii Organicznej, Politechnika Krakowska,  
ul. Warszawska 24, 31-155 Kraków).

Received: September 26, 1989

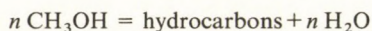
Problems related to equilibrium compositions in the methanol-to-gasoline process were studied in detail. The system under consideration consisted of 153 species and included all components resulting in amounts over 1 wt%. The Gibbs free energy minimization method was used to compute the equilibrium composition. The results of published bench scale process studies were subjected to searching examination in order to find and impose some compositional restrictions upon the model. The restricted model describes quite accurately the yield and distribution of hydrocarbons resulting in the methanol-to-gasoline process and facilitates the outlining of prospective suggestions for process improvement.

### Introduction

In many processes, experimental or commercial results show that some of the thermodynamically possible reactions do not run into the equilibrium state, because of being too slow to occur. Such systems reach only a pseudo-equilibrium or restricted equilibrium state, i.e. an equilibrium state with some compositional constraints imposed. This problem becomes very important when the calculated and experimentally found compositions are to be compared. Therefore, it is not surprising that restricted equilibrium was discussed by several authors. The general approach to this problem was presented in review papers [1-2]. Some case problems were also studied in detail. In 1965, JANICZEK and BLASIAK [3] presented an interesting equilibrium study of the nitrogen oxides-water-oxygen system. The correspondence of the experimental values with the calculated ones was obtained after assuming that some of the thermodynamically probable reactions do not occur. In the equilibrium model of the catalytic reforming of naphthas [4] the hydrocracking reactions are omitted. These reactions are thermodynamically preferred, but they are too slow to complete. The restrictions imposed upon the model include the elimination of

any reactions between hydrocarbons of different carbon atom numbers and deleting all hydrocracking products from the list of species. The restricted model provides facilities for the very accurate and precise calculation of the composition of commercial reformates. Similar restrictions with the same effect, are imposed on the equilibrium model of commercial hydroisomerization processes of light naphthas. In both cases, the unrestricted models result in a false product composition (a mixture of  $H_2$  and  $CH_4$  or  $CH_4$  and  $C_6H_6$  depending on the H/C atom ratio in the feed). In the equilibrium model of the KOPPERS-TOTZEK coal gasification process [11] the BOUDOUARD reaction assuming an equilibrium state between C, CO and  $CO_2$  must not be taken into consideration. The restricted model becomes thereby an efficient tool to compute the yield and composition of the gasification products and to forecast the effect of coal composition and operating conditions on the gas quality and its yield. Another example is methanol produced from synthesis gas. In this process, methane is thermodynamically preferred. However, commercial experience and kinetic investigations show that at temperatures and pressures typical for methanol synthesis, the reaction of methane formation is very slow. Therefore, this reaction has to be erased from the equilibrium model, otherwise methane will top the equilibrium list of products unlike the commercial experience.

It is not surprising that in the first place processes involving a great number of species will not reach the true equilibrium state. A large number of species implicates a large number of independent reactions of different rate constants and therefore, some of them being too slow, will not complete. Processes with a great number of species are typical for hydrocarbon conversion (such as the above mentioned catalytic reforming and hydroisomerization) and hydrocarbon synthesis. A novel process for the hydrocarbon synthesis is the conversion of methanol to gasoline over a selective zeolite catalyst [5-8]. Both fixed and fluid bed processes were studied. In the fixed bed process, two reactors are used and a single reactor in the fluid bed process. Irrespective of the process concept, the conversion of methanol to hydrocarbons and water according to overall reaction



is complete and virtually stoichiometric. The resulting hydrocarbons represent, however, a highly complex mixture consisting of  $C_1$ - $C_{10}$  paraffins,  $C_2$ - $C_{10}$  olefins,  $C_5$ - $C_{10}$  naphthenes and  $C_6$ - $C_{11}$  aromatics. The reaction product also includes equivalent amounts of  $H_2O$ , unreacted  $CH_3OH$ , intermediate product  $(CH_3)_2O$ , small amounts of CO,  $CO_2$  and  $H_2$ , and coke. It is a rather arduous procedure to calculate equilibrium composition of such a large system. Therefore, the published papers [7-8] are only fragmentary and they do not include detailed information about all components of the system. YURCHAK et al. [8] presented a comparison of the experimental results with equilibrium values. The comparison is, however, limited to pentenes and aromatics distribution only.

The objective here is to present an equilibrium model, including all possible components resulting in significant amounts (over 1 wt%) in the methanol-to-gasoline process.

### Model Formulation

The outlet mixture of the methanol-to-gasoline reactors consists of over 150 components. Of course, it is inevitable that some restrictions must be imposed upon the equilibrium model describing such a complex system. These restrictions, exceeding any thermodynamic formalism, should be rooted in the intimate knowledge of the problem. Unfortunately no material appears to be available in literature concerning the commercial data of the methanol-to-gasoline process. Therefore, the results of the fixed bed bench scale process studies [8] were subjected to particular analysis in order to find some general regularities facilitating the imposition of compositional restrictions upon the model. The investigations reported were conducted in a two-stage reactor system with a recycle to the second stage. The reported operating conditions were: 2 MPa, 686 K, feed composition 83% CH<sub>3</sub>OH and 17% H<sub>2</sub>O by wt., and the gas recycle to methanol mole ratio 9 : 1. The restrictions due to the accurate analysis of the reported data can be reduced to only two statements:

- 1st: Species resulting in quantities below 1 wt% such as C, CO, CO<sub>2</sub>, H<sub>2</sub>, CH<sub>4</sub>, C<sub>2</sub>H<sub>4</sub>, C<sub>2</sub>H<sub>6</sub> and C<sub>10+</sub> PON hydrocarbons must not be included into the model  
 2nd: The H/C atomic ratio in the mixture of the C<sub>3</sub>-C<sub>9</sub> paraffins equals 2.4

Following species were, therefore, taken into consideration: H<sub>2</sub>O, unreacted CH<sub>3</sub>OH and (CH<sub>3</sub>)<sub>2</sub>O, 73 C<sub>3</sub>-C<sub>9</sub> paraffins (from propane to tetramethylpentanes), 23 aromatics (from benzene to pentamethylbenzene), 31 olefins (from propene to nonene) and 23 naphthenes (from cyclopentane to trimethylcyclohexanes), in sum 153 species. The equilibrium model covers all the species published in thermodynamic data tables [9]. Not all isomers of the C<sub>7</sub>-C<sub>9</sub> olefins, C<sub>8</sub>-C<sub>9</sub> naphthenes and C<sub>10</sub>-C<sub>11</sub> aromatics are listed in these tables. Nevertheless these hydrocarbons occur in the equilibrium mixture in such insignificant quantities that the error resulting from the lack of some isomeric forms can be neglected.

Many of the resulting species are isomers and resulting from this fact the number of independent components can be drastically reduced. The equilibrium composition of isomers depends on the temperature and thermodynamic properties of individual species only, being totally independent of other operating conditions, such as pressure, initial feed composition and the amount of inerts. The proportion of any component in an equilibrium mixture of isomers is given by:

$$x_i = \frac{\exp(z_i^0 + z_1^0)}{\sum_i \exp(z_i^0 - z_1^0)} \quad (1)$$

where:

$$z_i = \frac{\Delta G_{f_i}^0}{RT} \quad (2)$$

The average Gibbs free energy of formation of such a mixture of isomers is defined as:

$$\overline{\Delta G_f^0} = \sum_i x_i \cdot \Delta G_{f_i}^0 + RT \cdot \sum_i x_i \cdot \ln x_i \quad (3)$$

where  $\overline{\Delta G_f^0}$  is the average value of the Gibbs free energy of formation of an equilibrium mixture of isomers.

The main advantage of such an approach is that in the calculating procedure, the equilibrium mixture of the isomers can be regarded as an individual species with exactly thermodynamic properties, thus involving a considerable reduction of independent components. This approach was put to successful use in calculating the complex equilibrium composition of reformates [4].

Thereby the whole multicomponent reaction mixture of the methanol-to-gasoline process, consisting of 153 species, can be regarded as a mixture of only 23 components ( $\text{CH}_3\text{OH}$ ,  $(\text{CH}_3)_2\text{O}$ ,  $\text{H}_2\text{O}$ , 7 paraffins  $\text{C}_3\text{--C}_9$ , 6 aromatics  $\text{C}_6\text{--C}_{11}$ , 2 olefins  $\text{C}_3\text{--C}_4$ , and 5 olefins and naphthenes  $\text{C}_5\text{--C}_9$ ), with recycle gas treated as an inert. The most efficient way to calculate the equilibrium composition of systems containing above 20 components is by using the Gibbs free energy minimization method.

It is now possible to formulate the equilibrium model of the methanol-to-gasoline process:

$$\min g = \sum_i n_i \cdot \left( \mu_i^0 + RT \cdot \ln \frac{P}{P^0} \right) + RT \sum_i n_i \cdot \ln \frac{n_i}{\sum_i n_i} \quad (4)$$

subject to:

the elemental abundance:

$$\sum_i A_{ij} \cdot n_i = B_j \quad j = 1, 2, 3 \text{ for C, H, O resp.} \quad (5)$$

and non-negativity constraints:

$$n_i > 0$$

and to the additional restriction due to the 1st statement in the form of a list of species excluded, and to the additional restriction due to the 2nd statement:

$$\frac{8 \cdot n_{\text{C}_3\text{H}_8} + 10 \cdot n_{\text{C}_4\text{H}_{10}} + \dots + 20 \cdot n_{\text{C}_9\text{H}_{20}}}{3 \cdot n_{\text{C}_3\text{H}_8} + 4 \cdot n_{\text{C}_4\text{H}_{10}} + \dots + 9 \cdot n_{\text{C}_9\text{H}_{20}}} = 2.4 \quad (6)$$

It must be remembered that in the above Equations (4–6) symbols  $n_i$  and  $\mu_i^0$  not only represent mole numbers and chemical potentials of individual species, such as propane or benzene, but also the corresponding values for the equilibrium mixtures of isomers (e.g. all  $\text{C}_9\text{H}_{20}$  paraffins).

The SUMT algorithm [10] was adopted to minimize the objective function (4).

### Model Verification

The calculations were executed for the above listed parameters reported by YURCHAK [8]. The comparison of experimental hydrocarbon distribution with the calculated equilibrium composition has been a rather difficult task, because of changes in product distribution during individual cycles and from cycle to cycle. With all the differences in product distribution reported by YURCHAK, some common regularities can, however, be observed. For the purpose of illustration, we shall compare the results reported by YURCHAK for the second cycle and 94 hrs. on stream. The detailed results of equilibrium calculations regarding all species of the model are presented in *Table 1*, and the confronta-

*Table 1.*

Detailed results of equilibrium calculations, wt%

1. methanol	0.0	43. 2-methyloctane	0.5
2. water	0.0	44. 3-methyloctane	0.6
3. dimethyl ether	0.0	45. 4-methyloctane	0.6
4. propane	8.5	46. 3-ethylheptane	0.2
5. n-butane	8.2	47. 4-ethylheptane	0.2
6. isobutane	5.6	48. 2,2-dimethylheptane	0.2
7. n-pentane	4.4	49. 2,3-dimethylheptane	0.2
8. isopentane	9.4	50. 2,4-dimethylheptane	0.4
9. neopentane	0.9	51. 2,5-dimethylheptane	0.4
10. n-hexane	2.6	52. 2,6-dimethylheptane	0.2
11. 2-methylpentane	3.8	53. 3,3-dimethylheptane	0.3
12. 3-methylpentane	2.0	54. 3,4-dimethylheptane	0.1
13. 2,2-dimethylbutane	1.8	55. 3,5-dimethylheptane	0.1
14. 2,3-dimethylbutane	1.1	56. 4,4-dimethylheptane	0.1
15. n-heptane	1.5	57. 2-methyl-3-ethylhexane	0.1
16. 2-methylhexane	2.0	58. 2-methyl-4-ethylhexane	0.1
17. 3-methylhexane	2.1	59. 3-methyl-3-ethylhexane	0.1
18. 3-ethylpentane	0.3	60. 4-methyl-3-ethylhexane	0.1
19. 2,2-dimethylpentane	0.6	61. 2,2,3-trimethylhexane	0.0
20. 2,3-dimethylpentane	2.1	62. 2,2,4-trimethylhexane	0.0
21. 2,4-dimethylpentane	0.4	63. 2,2,5-trimethylhexane	0.2
22. 3,3-dimethylpentane	0.6	64. 2,3,3-trimethylhexane	0.0
23. 2,2,3-trimethylbutane	0.1	65. 2,3,4-trimethylhexane	0.0
24. n-octane	0.8	66. 2,3,5-trimethylhexane	0.1
25. 2-methylheptane	0.7	67. 2,4,4-trimethylhexane	0.0
26. 3-methylheptane	0.9	68. 3,3,4-trimethylhexane	0.0
27. 4-methylheptane	0.3	69. 3,3-diethylpentane	0.0
28. 3-ethylhexane	0.4	70. 2,2-dimethyl-3-ethylpentane	0.0
29. 2,2-dimethylhexane	0.2	71. 2,3-dimethyl-3-ethylpentane	0.0
30. 2,3-dimethylhexane	0.1	72. 2,4-dimethyl-3-ethylpentane	0.0
31. 2,4-dimethylhexane	0.4	73. 2,2,3,3-tetramethylpentane	0.0
32. 3,5-dimethylhexane	0.3	74. 2,2,3,4-tetramethylpentane	0.0
33. 3,3-dimethylhexane	0.2	75. 2,2,4,4-tetramethylpentane	0.0
34. 3,4-dimethylhexane	0.2	76. 2,3,3,4-tetramethylpentane	0.0
35. 2-methyl-3-ethylpentane	0.1	77. benzene	5.0
36. 3-methyl-3-ethylpentane	0.0	78. toluene	11.8
37. 2,2,3-trimethylpentane	0.0	79. ethylbenzene	0.8
38. 2,2,4-trimethylpentane	0.1	80. m-xylene	4.7
39. 2,3,3-trimethylpentane	0.0	81. o-xylene	2.2
40. 2,3,4-trimethylpentane	0.0	82. p-xylene	2.1
41. 2,2,3,3-tetramethylpentane	0.0	83. n-propylbenzene	0.1
42. n-nonane	0.4	84. isopropylbenzene	0.0

85. 1-methyl-2-ethylbenzene	0.2	121. 3-methyl-tr.-2-pentene	0.0
86. 1-methyl-3-ethylbenzene	0.6	122. 4-methyl-cis-2-pentene	0.0
87. 1-methyl-4-ethylbenzene	0.4	123. 4-methyl-tr.-2-pentene	0.0
88. 1,2,3-trimethylbenzene	0.2	124. 2-ethyl-1-butene	0.0
89. 1,2,4-trimethylbenzene	1.6	125. 2,3-dimethyl-1-butene	0.0
90. 1,3,5-trimethylbenzene	0.6	126. 3,3-dimethyl-1-butene	0.0
91. n-butylbenzene	0.0	127. 2,3-dimethyl-2-butene	0.0
92. 1,2-diethylbenzene	0.0	128. 1-heptene	0.0
93. 1,3-diethylbenzene	0.0	129. 1-octene	0.0
94. 1,4-diethylbenzene	0.0	130. 1-nonene	0.0
95. 1,2,3,4-tetramethylbenzene	0.1	131. cyclopentane	0.1
96. durene	0.1	132. cyclohexane	0.0
97. isodurene	0.2	133. methylcyclopentane	0.1
98. n-pentylbenzene	0.0	134. ethylcyclopentane	0.0
99. pentamethylbenzene	0.0	135. 1,1-dimethylcyclopentane	0.0
100. propene	0.7	136. 1,cis-2-dimethylcyclopentane	0.0
101. 1-butene	0.0	137. 1,trans-2-dimethylcyclopentane	0.0
102. cis-2-butene	0.0	138. 1,cis-3-dimethylcyclopentane	0.0
103. trans-2-butene	0.0	139. 1,trans-3-dimethylcyclopentane	0.0
104. 2-methylpropene	0.0	140. methylcyclohexane	0.0
105. 1-pentene	0.0	141. n-propylcyclopentane	0.0
106. cis-2-pentene	0.0	142. ethylcyclohexane	0.0
107. trans-2-pentene	0.0	143. 1,1-dimethylcyclohexane	0.0
108. 2-methyl-1-butene	0.0	144. 1,cis-2-dimethylcyclohexane	0.0
109. 3-methyl-1-butene	0.0	145. 1,trans-2-dimethylcyclohexane	0.0
110. 2-methyl-2-butene	0.1	146. 1,cis-3-dimethylcyclohexane	0.0
111. 1-hexene	0.0	147. 1,trans-3-dimethylcyclohexane	0.0
112. cis-2-hexene	0.0	148. 1,cis-4-dimethylcyclohexane	0.0
113. trans-2-hexene	0.0	149. 1,trans-4-dimethylcyclohexane	0.0
114. cis-3-hexene	0.0	150. n-butylcyclopentane	0.0
115. trans-3-hexene	0.0	151. n-propylcyclohexane	0.0
116. 2-methyl-1-pentene	0.0	152. 1,cis-3-cis-5-trimethylcyclohexane	0.0
117. 3-methyl-1-pentene	0.0	153. 1,cis-3,trans-5-trimethylcyclohexane	0.0
118. 4-methyl-1-pentene	0.0		
119. 2-methyl-2-pentene	0.0		
120. 3-methyl-cis-2-pentene	0.0		
			Total 99.6

Note: 0.0 means below 0.05 wt%.

tion with experimental hydrocarbon distribution in *Tables 2* through 5. The most convenient characterization of a complex hydrocarbon mixture is its class and group distribution, i.e. the contribution of hydrocarbons with the same carbon atom number (class distribution) and the contribution of hydrocarbons

Table 2.

Comparison of experimental hydrocarbon group distribution with equilibrium values, wt%.

	exptl.	equil.
methane, ethane, propane	8.1	8.5
butanes	13.0	13.8
pentanes	13.1	14.7
C <sub>2</sub> -C <sub>5</sub> olefins	3.1	0.8
cyclopentane	0.3	0.1
C <sub>6+</sub> nonaromatics	31.5	31.5
C <sub>6</sub> -C <sub>11</sub> aromatics	30.8	30.6
naphthalenes	0.1	0.0
Total	100.0	100.0

Table 3.

Light hydrocarbons distribution. Comparison of experimental and equilibrium values, wt%.

Detailed distribution of the C <sub>5</sub> - hydrocarbons	exptl.	equil.
methane	0.9	—
ethane	0.6	—
propane	6.6	8.5
n-butane	3.7	8.2
isobutane	9.3	5.6
n-pentane	1.7	4.4
isopentanes	11.4	10.3
ethene	0.0	—
propene	0.2	0.7
butenes	1.0	0.0
pentenes	1.9	0.1
cyclopentane	0.3	0.1
Total	37.6	37.9
isobutane/n-butane	2.51	0.68
isopentanes/n-pentane	6.71	2.34

Table 4.

C<sub>6</sub>+ nonaromatics distribution. Comparison of experimental and equilibrium values, wt%.

	exptl.	equil.
Class distribution		
C <sub>6</sub>	13.8	11.4
C <sub>7</sub>	8.4	9.8
C <sub>8</sub>	6.3	5.0
C <sub>9</sub>	2.3	5.3
C <sub>10</sub> +	0.7	—
Total	31.5	31.5
Group distribution		
C <sub>6</sub> -C <sub>9</sub> n-paraffins	1.1	5.3
C <sub>6</sub> -C <sub>9</sub> isoparaffins	16.7	26.0
C <sub>6</sub> -C <sub>9</sub> olefins	6.0	0.1
C <sub>6</sub> C <sub>9</sub> naphthenes	7.0	0.1
C <sub>10</sub> + PON	0.7	—
Total	31.5	31.5
isoparaffins/n-paraffins	15.2	4.9

Table 5.

Comparison of experimental aromatics distribution with equilibrium values, wt%.

Aromatic distribution	exptl.	equil.
C <sub>6</sub>	0.2	5.0
C <sub>7</sub>	2.0	11.8
C <sub>8</sub>	10.0	9.8
C <sub>9</sub>	11.1	3.6
C <sub>10</sub>	6.7	0.4
C <sub>11</sub>	0.8	0.0
Total	30.8	30.6
ethylbenzene	6.0	8.2
p- and m-xylenes	74.0	69.4
o-xylene	20.0	22.4
Total C <sub>8</sub> aromatics	100.0	100.0
trimethylbenzenes	73.9	66.6
methylethylbenzenes	25.2	30.6
propylbenzenes	0.9	2.8
Total C <sub>9</sub> aromatics	100.0	100.0
durene	62.7	28.8
isodurene	6.0	51.5
1, 2, 3, 4-tertamethylbenzene	3.0	11.6
other C <sub>10</sub> benzenes	28.3	8.1
Total C <sub>10</sub> aromatics	100.0	100.0

belonging to the same group, such as paraffins, olefins, naphthenes and aromatics.

The amounts of gaseous hydrocarbons C<sub>1</sub> and C<sub>2</sub> are so insignificant that these compounds can, as mentioned above, be excluded from the model. The content of propane, butanes, pentanes and C<sub>6+</sub> nonaromatics is in reasonable agreement with the computed values. Considerable differences occur in the isobutane/n-butane mole ratio, 2.51 and 0.68 in the experimental product and in the equilibrium mixture, resp. The content of isopentanes is approximately the same, but the equilibrium contribution of n-pentane is about 2.5 times greater when compared with the experimental data. Equilibrium amounts of the C<sub>3</sub>-C<sub>5</sub> olefins are below 1 wt% and decrease with increasing carbon number in the molecule. In the product, the amounts of these olefins are 3.1 wt% and increase with the increasing carbon number. The contribution of the C<sub>6+</sub> nonaromatics to the total is 31.5 wt% in the product as well as in the equilibrium mixture and hydrocarbon class distribution is similar. Both in the equilibrium mixture and in the experimental product, the contribution of hydrocarbons decreases with increasing carbon number in the molecule. Significant differences occur in the hydrocarbon group distribution. Equilibrium mixture in the C<sub>6+</sub> nonaromatics consists of paraffins accompanied by trace amounts of olefins and

naphthenes. The experimental products exhibited different group composition with significant amounts of olefins and naphthenes, 6.0 and 7.0 wt%, resp. The equilibrium isoparaffins/n-paraffins mole ratio is 4.9 as compared to 15.2 in the product, but nevertheless the contribution of the high octane number isoparaffins to all  $C_{6+}$  nonaromatics is higher in the equilibrium mixture than in the product.

Significant amounts of aromatics are produced, this fact being in good accordance with equilibrium calculations, but the detailed aromatics distribution exhibits some differences. Only small quantities of benzene and toluene are produced, 2.2 wt% in the experimental product compared to 16.8 wt% in the equilibrium mixture. According to equilibrium calculations, toluene is favoured and the fraction of alkyl substituted benzenes decreases with the increasing chain carbon/ring carbon ratio. In the experimental product, the  $C_8$  and  $C_9$  aromatics dominate. The fractions of the individual isomers in the  $C_8$  and  $C_9$  aromatics are similar in the experimental product as well as in the equilibrium mixture. The  $C_{10}$  aromatics are produced in significant amounts, unlike the equilibrium composition. Among the  $C_{10}$  aromatics, mainly durene is produced, this fact being undesirable, because of its high melting point. Taking into consideration the gasoline quality requirements (octane number, vapour pressure and boiling range) the equilibrium distribution of aromatics is more advantageous compared to experimental results.

Comparative computations covering a large region of pressures and temperatures (0.15–5.0 MPa and 560–740 K) exhibited a minor effect of the operating conditions on the equilibrium yield and hydrocarbon distribution. The point of a possible process improvement is, therefore, in an improvement of the catalyst selectivity.

### Conclusions

The comparison of the equilibrium and the experimental hydrocarbon distribution suggests prospective directions in catalyst improvement. The conversion of methanol to hydrocarbons and water is complete and in this respect the properties of the catalyst are excellent. The calculations exhibit, however, that the conversion of olefins to paraffins and aromatics is thermodynamically favoured. In spite of this fact, experimental results show, however, that the reactions of the olefins formed as intermediate compounds do not proceed to a complete conversion. Some of them remain unchanged and some are transformed to naphthenes only. The departure from the equilibrium state is in this case disadvantageous, because naphthenes replace the high octane number aromatics and the unchanged olefins deteriorate the stability of gasoline. In contrast to this, the isoparaffins/n-paraffins mole ratio is less advantageous in the equilibrium mixture as compared to experimental data. These facts indicate that from all complex properties of the catalyst, in the first place its dehydrocyclization power must be improved. Such an improvement will result in a greater yield of aromatics accompanied by a reduction of olefins and as a consequence in a

higher octane number and better stability of gasoline. Some shift of the distribution of aromatic hydrocarbons according to the equilibrium calculations towards toluene and benzene will also be desirable. On the other hand, the isomerization properties of the catalyst must not be too high, because the equilibrium iso-paraffins/n-paraffins mole ratio is less advantageous.

The most significant result of the presented study is in demonstrating that it is feasible to formulate an equilibrium model for such a large and complex system and to outline prospective suggestions for process improvement.

### Acknowledgment

The study was sponsored by the Polish Academy of Science. Project No. CPBP-01.16.

### SYMBOLS

$A_{ij}$	number of atoms of the element $j$ in component $i$
$B_j$	gramatoms of element $j$ in feed
$g$	Gibbs free energy, kJ
$\Delta G_{fi}^0$	standard molar Gibbs free energy of formation, kJ/mole
$n_i$	number of moles of species $i$ or isomer mixture
$P, P^0$	total and standard pressure, respectively, MPa
PON	paraffins + olefins + naphthenes
$R$	gas constants, kJ/(mole · K)
$T$	temperature, K
$x_i$	mole fraction of isomer $i$
$\mu_i^0$	standard chemical potential of species $i$

### REFERENCES

- GAUTAM, R., and SEIDER, W. D.: *AIChE J.* 1979, 25, 991.
- SMITH, W. R.: *Ind. Eng. Chem. Fund.* 1980, 19, 1.
- JANICZEK, W. and BLASIAK, E.: *Chimie et Industrie* 1965, 94, 478.
- KRAMARZ, J.: *Zeszyty Naukowe Pol. Krak., Chemia, Z.* 15, 1981, Krakow.
- MEISEL, S. L., MCCULLOUGH, J. P., LECHTHALER, C. H., and WEISZ, P. B.: *CHEMTECH*, 1976, 6, 86.
- WISE, J. J., and SILVESTRI, A. J.: *Oil and Gas J.*, 1976, Nov. 22, 141
- CHANG, C. D., KUO, J. C. W., LANG, W. H., JACOB, S. M., WISE, J. J., and SILVESTRI, A. J.: *Ind. Eng. Chem. Proc. Des. Dev.*, 1978, 17, 255
- YOURCHAK, S., STERLING, E. W., and WARNER, J. P.: *Ind. Eng. Chem. Proc. Des. Dev.*, 1979, 18, 527.
- STULL, D. R., WESTRUM, E. F., and SINKE, G. C.: *The Chemical Thermodynamics of Organic Compounds*. Wiley, New York, 1969.
- KUESTER, J. L., and MIZE, J. H.: *Optimization techniques with FORTRAN*. McGraw-Hill, Inc. 1973.
- KRAMARZ, J., WYCZESANY, A., and WOLFF, A., presented for printing in this Journal.

## THERMODYNAMIC MODEL OF COAL AND PETROLEUM FEEDS GASIFICATION

J. KRAMARZ, A. WYCZESANY, and A. WOLFF

(Instytut Chemii i Technologii Organicznej, Politechnika Krakowska, ul. Warszawska 24, 31-155  
Kraków)

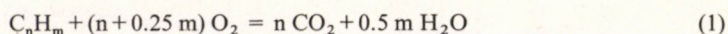
Received: September 26, 1989

The feature of the presented model is its significantly good agreement with experimental data resulting in long term runs of commercial Koppers-Totzek and Shell gasification units. Such an agreement is the consequence of very accurate analysis of all possible reactions, i. e. combustion, gasification and gas reactions. The result of a large number of competing reactions is that some of them, being too slow, will not complete. Therefore, the gasification process is regarded as a system of restricted chemical equilibrium. The comparison of computed equilibrium compositions with commercial data showed that the Boudouard reaction must not be taken into consideration. This correction, taking into account the kinetic restrictions, results in a thermodynamic model consistent with the experimental data and as a consequence, good predictive ability.

### Introduction

The present-day processes of coal mining produce huge quantities of fine coal unsuitable in direct use, but suitable in the Koppers-Totzek gasification process. The resulting fuel gas has a medium heating value and is free of pollutants. It can also be appropriate stock for the SNG process, methanol or  $\text{NH}_3$  synthesis (gasification with air). The Koppers-Totzek gasification is also very attractive for lignite conversion. Another possibility is the application of Shell or Texaco gasification [1] in refineries short in hydrogen. These plants are fed with low value crude residues and asphalts.

The coal and petroleum feed gasification is based on reactions of carbon or hydrocarbons and heterocomponents respectively with steam and oxygen according to following reactions: – feed combustion reactions



– gasification reactions



– gas combustion reactions



– gas reactions



The process as a whole is autothermic, because its endothermic gasification reactions are balanced by exothermic effects of combustion.

### Thermodynamic model

The presented method assumes that coal or crude residue of known composition is gasified with known amounts of gasification agents (steam and oxygen, steam and air or steam and air enriched in oxygen). The oxygen is not present at the equilibrium state, because of its complete consumption. The conversion of carbon is not complete, but the unreacted carbon is not in a chemical equilibrium with the gas phase and from thermodynamic point of view it is regarded as an inert. This is an essential novelty in the previous approach relating to thermodynamic gasification models assuming that reactions 4–6 achieve chemical equilibrium.

Some preliminary calculations exhibited, however, very inaccurate prediction of gas composition for the model assuming the chemical equilibrium between the gas phase and the unreacted carbon. One example of such calculations is presented in *Table 1*.

This representative example points out that the agreement of the computed gas composition with commercial data occurs only when reactions 4–6 are regarded as the restricted ones. In this connection, in the presented model, the chemical equilibrium of the gasification concerns the gas phase only. In process conditions, sulphur is converted totally to  $\text{H}_2\text{S}$ , therefore, amounts of  $\text{H}_2\text{S}$  depend only on the sulphur content in the feed. The small quantities of produced COS are to be neglected.

With these assumption, the chemical equilibrium can be described by two independent reactions 9 and 10. The mathematical model, therefore, includes two equations of chemical equilibrium constants of reactions 9 and 10 and three equations of mass balance of the elements (C, H, O). Independent variables of the model are mole numbers of  $\text{H}_2\text{O}$ ,  $\text{H}_2$ ,  $\text{CO}$ ,  $\text{CO}_2$ ,  $\text{CH}_4$  at equilibrium.

Table 1.

Comparison of equilibrium composition in coal gasification. Case 1 – restricted equilibrium.  
Case 2 – unrestricted equilibrium

Feed comp. %wt			
C	56.8		
H	3.6		
S	1.0		
O	7.2		
N	0.7		
Moisture	1.0		
Ash	29.7		
Oxygen cons. Nm <sup>3</sup> /t of feed	563		
Steam cons. kg/t of feed	300		
Inlet temp. °C			
Oxygen	104		
Steam	121		
Feed	71		
Pressure, MPa	0.1		
Carbon conv. %	98.0		
Dry gas comp. %mol	Plant	Case 1	Case 2
H <sub>2</sub>	28.7	28.9	37.9
CO	57.9	57.6	50.9
CO <sub>2</sub>	11.1	11.3	8.7
CH <sub>4</sub>	0.1	0.0	1.0
N <sub>2</sub>	2.2	2.2	1.5
Gas yield, Nm <sup>3</sup> /kg of feed	1.53	1.53	1.71

One mole of dry ash-free coal (DAF) is the most convenient reference state in calculations of the process mass and heat balance. The gasified raw coal consists of carbon, hydrogen, sulphur, oxygen, nitrogen, moisture and ash and their weight fractions are defined as  $g_C, g_H, g_S, g_O, g_N, g_M, g_A$ , respectively. One mole of DAF is described by the following formula:  $C_1H_aS_bO_cN_d$  and each gram-atom of carbon in raw coal corresponds to  $e$  moles of moisture (M) and  $f$  moles of ash (A). Quantities of gram-atoms of elements and values  $e$  and  $f$  are given below:

$$i = \frac{g_i \cdot M_c}{g_c \cdot M_i} \quad i = a, b, c, d, e, f \quad (11)$$

The equation of chemical equilibrium constants of reaction (9) and (10) have the following form:

$$K_1 = \frac{n_{CH_4} \cdot n_{H_2O} \cdot \left( \sum_i n_i \right)^2 \cdot (P^0)^2}{n_{CO} \cdot n_{H_2}^3 \cdot P^2} \quad (12)$$

$$K_2 = \frac{n_{\text{CO}_2} \cdot n_{\text{H}_2}}{n_{\text{CO}} \cdot n_{\text{H}_2\text{O}}} \quad (13)$$

where:

$$\sum_i n_i = n_{\text{H}_2\text{O}} + n_{\text{H}_2} + n_{\text{CO}} + n_{\text{CO}_2} + n_{\text{CH}_4} + n_{\text{N}_2} + n_{\text{H}_2\text{S}} \quad (14)$$

$$n_{\text{N}_2} = 0.5 \cdot d \cdot V \cdot n_{\text{O}_2}^0 \quad (15)$$

$$n_{\text{H}_2\text{S}} = b \quad (16)$$

Equations of mass balance of elements:

$$n_{\text{CO}} + n_{\text{CO}_2} + n_{\text{CH}_4} = \alpha_C \quad (17)$$

$$2 \cdot n_{\text{H}_2\text{O}} + 2 \cdot n_{\text{H}_2} + 4 \cdot n_{\text{CH}_4} = 2 \cdot n_{\text{H}_2\text{O}}^0 + 2 \cdot e + a - 2 \cdot b \quad (18)$$

$$n_{\text{H}_2\text{O}} + n_{\text{CO}} + 2 \cdot n_{\text{CO}_2} = n_{\text{H}_2\text{O}}^0 + e + 2 \cdot n_{\text{O}_2}^0 + c \quad (19)$$

where:

$\alpha_C$  carbon conversion according to literature data

$$0.59 < \alpha_C < 0.99$$

The equilibrium constants  $K_1$  and  $K_2$  are functions of temperature  $T$ . On the basis of data [2] the reactions  $\Delta G f_T^0 = f(T)$  for  $\text{H}_2\text{O}$ ,  $\text{CO}$ ,  $\text{CO}_2$  and  $\text{CH}_4$  were derived in form:

$$\Delta G f_T^0 = A_0 + A_1 \cdot T + A_2 \cdot T^2 + A_3 \cdot T^3 + A_4 \cdot T \cdot \ln T \quad (20)$$

leading to following analytical expression for  $K_1$  and  $K_2$ :

$$K_1 = \exp \frac{188.1 + 0.2467 \cdot T + 42.75 \cdot 10^{-6} \cdot T^2 - 3.999 \cdot 10^{-9} \cdot T^3 - 72.46 \cdot 10^{-3} \cdot T \cdot \ln T}{8.3147 \cdot 10^{-3} \cdot T} \quad (21)$$

$$K_2 = \exp \frac{43.45 - 0.0816 \cdot T + 5.01 \cdot 10^{-6} \cdot T^2 - 0.8742 \cdot 10^{-9} \cdot T^3 + 5.366 \cdot 10^{-3} \cdot T \cdot \ln T}{8.3147 \cdot 10^{-3} \cdot T} \quad (22)$$

Industrial gasification plants are operated at autothermal conditions. Typically, coal and oxygen (air) are fed at 298 K and steam at 623 K. Products leaving the generator are gas and ash containing unreacted carbon. The process proceeds with some heat losses to surroundings, which are equal to about 5% of the heating value of coal.

The equilibrium temperature is not known in advance. This temperature results from the energy balance covering heat of all reactions, heat losses and enthalpy of the substrate and product streams. Since the equilibrium temperature and equilibrium composition are interrelated they must be determined simultaneously. Our task of finding the outlet temperature includes the determination of all outlet conditions, i. e. composition and temperature, which give an enthalpy change that satisfies the overall energy balance.

$$H = n_{\text{H}_2\text{O}} \cdot \Delta H f_{\text{H}_2\text{O}(\text{g})}^0 + n_{\text{CO}} \cdot \Delta H f_{\text{CO}}^0 + n_{\text{CO}_2} \cdot \Delta H f_{\text{CO}_2}^0 + n_{\text{CH}_4} \cdot \Delta H f_{\text{CH}_4}^0 + n_{\text{H}_2\text{S}} \cdot \Delta H f_{\text{H}_2\text{S}}^0 -$$

$$\begin{aligned}
& -1 \cdot \Delta H_{\text{DAF}}^0 - e \cdot \Delta H_{\text{H}_2\text{O}(1)}^0 - n_{\text{H}_2\text{O}}^0 \cdot \Delta H_{\text{H}_2\text{O}(\text{g})}^0 + n_{\text{H}_2\text{O}} \cdot (H_{\text{T}}^0 - H_{298}^0)_{\text{H}_2\text{O}} + \\
& + n_{\text{H}_2} \cdot (H_{\text{T}}^0 - H_{298}^0)_{\text{H}_2} + n_{\text{CO}} \cdot (H_{\text{T}}^0 - H_{298}^0)_{\text{CO}} + n_{\text{CO}_2} \cdot (H_{\text{T}}^0 - H_{298}^0)_{\text{CO}_2} + n_{\text{CH}_4} \cdot (H_{\text{T}}^0 - H_{298}^0)_{\text{CH}_4} + \\
& + n_{\text{N}_2} \cdot (H_{\text{T}}^0 - H_{298}^0)_{\text{N}_2} + n_{\text{H}_2\text{S}} \cdot (H_{\text{T}}^0 - H_{298}^0)_{\text{H}_2\text{S}} + (1 - \alpha_{\text{C}}) \cdot (H_{\text{T}}^0 - H_{298}^0)_{\text{C}} + f \cdot (H_{\text{T}}^0 - H_{298}^0)_{\text{ash}} - \\
& - n_{\text{H}_2\text{O}} \cdot (H_{623}^0 - H_{298}^0)_{\text{H}_2\text{O}(\text{g})} + Q_{\text{losses}} + f \cdot \Delta H_{\text{m,ash}}^0 \quad (23)
\end{aligned}$$

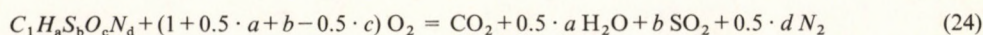
Moisture in the coal is regarded as liquid water. The temperature dependence of thermodynamic functions  $(H_{\text{T}}^0 - H_{298}^0)_i$  are represented in the form of a trinomial. The coefficients of these trinomials (Table 2) are computed on the basis of the JANAF Tables [2] by the least square method.

Table 2.

The  $\Delta H_{298}^{\circ}$  values and coefficients of equation  $(H_{\text{T}}^0 - H_{298}^0) = a_0 + a_1 T + a_2 T^2$

Compound	$\Delta H_{298}^{\circ}$ , kJ/mol	$a_0$ , kJ/mol	$a_1 \cdot 10^3$ , kJ/mol/K	$a_2 \cdot 10^6$ , kJ/mol/K
H <sub>2</sub> O <sub>(g)</sub>	-241.827	-9.36192	29.65961	5.75384
H <sub>2</sub>	0.0	-7.99745	26.90680	1.76634
CO	-110.529	-8.77405	28.16026	2.36695
CO <sub>2</sub>	-393.522	-14.58670	42.49790	5.37585
CH <sub>4</sub>	-74.873	-13.88831	35.23254	17.19109
N <sub>2</sub>	0.0	-8.56968	27.70628	2.38674
H <sub>2</sub> S	-20.418	-10.68922	32.44855	6.35738
C	0.0	-5.57410	14.25162	3.22740
O <sub>2</sub>	0.0	-9.51951	30.07902	2.20283
H <sub>2</sub> O <sub>(l)</sub>	-286.030	-	-	-

The standard enthalpy of formation  $\Delta H_{\text{DAF}}^0$  is calculated using the Hess law. The combustion of one mole of DAF in oxygen undergoes as follows:



Semiempirical formula [3] is used to calculate the heating value of DAF in kJ/g of DAF:

$$Q_{\text{DAF}}^1 = \frac{33.913 \cdot g_{\text{C}} + 102.995 \cdot g_{\text{H}} - 10.886 \cdot (g_{\text{O}} - g_{\text{S}})}{g_{\text{C}} + g_{\text{H}} + g_{\text{S}} + g_{\text{O}} + g_{\text{N}}} \text{ [kJ/g]} \quad (25)$$

and:

$$Q_{\text{DAF}} = Q_{\text{DAF}}^1 \cdot M_{\text{DAF}} \text{ [kJ/g]} \quad (26)$$

The standard enthalpy of formation of one mole of DAF is calculated from stoichiometry of reaction (24):

$$\Delta H_{\text{DAF}}^0 = \Delta H_{\text{CO}_2}^0 + 0.5 \cdot a \cdot \Delta H_{\text{H}_2\text{O}(\text{g})}^0 + b \cdot \Delta H_{\text{SO}_2}^0 + Q_{\text{DAF}} \quad (27)$$

The term  $(H_{623}^0 - H_{298}^0)_{\text{H}_2\text{O}(\text{g})}$  in Equation (23) taken from the steam tables [4] equals 11.322 kJ/mol.

Heat losses in the overall heat balance of the generator are the function of  $Q_{\text{DAF}}$  and coal conversion:

$$Q_{\text{losses}} = 0.05 \cdot Q_{\text{DAF}} \cdot \alpha_{\text{C}} \quad (28)$$

At a process temperature higher than the fusion point of ash (1200 °C) the heat balance of the generator additionally includes the heat of fusion ( $\Delta H_{m,ash}^0 = 20.77$  kJ/mol) [3].

The heat balance is a function of temperature  $T$  and equilibrium composition of the reaction mixture. For autothermic conditions  $H=0$ . Thus, we look for such a temperature  $T$ , which together with the equilibrium composition leads to a zero value of the left side of the Equation (23). This is a relative simple matter, because an increase of  $T$  (starting from a low enough temperature level) and corresponding changes in equilibrium composition, cause the  $H$  value to change monotonically from negative values to positive ones. As a result, there must be the temperature  $T$  at which the  $H$  value is close to zero and this temperature is searched for.

The presented model derived for coal gasification can also be applied for the description of petroleum feed gasification. These feeds can also be represented by one chemical compound of the formula  $C_1H_aS_bO_cN_d$  and its standard enthalpy of formation is calculated identically as in the case of coal.

### The Model Checking.

The model verification was carried on the basis of the commercial data of 8 coal [5–10] and 4 petroleum feed gasification plants [1]. The wide range of the operating parameters of the considered commercial plants, summarized in *Table 3* show the model flexibility.

*Table 3.*  
Range of changes of industrial plant parameters

Parameter	Min. value	Max. value
Ash, %wt	0.0	35.1
Moisture, %wt	0.0	8.0
Sulphur, %wt	0.1	6.6
Atomic ratio C/H	0.44	6.71
Oxygen (95%vol) cons. Nm <sup>3</sup> /t of feed	338	875
Steam consumption kg/t of feed	100	500
Pressure, MPa	0.1	5.8

The differences in the type of feed (from coal to light naphtha) expressed in the  $C/H$  atomic ratio should be emphasized.

The results of calculations of the gas compositions in compared to commercial plant results are presented in *Tables 1 and 4*. These results indicate the high predicting ability of the thermodynamic model. This model provides evidence that an approach based on chemical equilibrium only is sufficiently adequate without resorting to any kinetic considerations. Such an approach must, however, be preceded by a thorough analysis of all possible reactions in order to determine which of them achieve chemical equilibrium. In the case of high temperature gasification processes, these are the gas phase reactions only.

### The Effect of Different Types of Coal on the Process Outcome

From the practical point of view it is interesting to predict the yield and heating value of the gas resulting from different types of coal. *Table 5* illustrates the gasification of 5 different coals from lignite to anthracite, however, having the same content of moisture and ash. The process conditions like steam and oxygen consumption for 1 mole of DAF are also the same.

It can clearly be seen that the influence of coal grade on the gas yield and its heating value is low. Thus, the most advantageous solution is to process commercially low grade coals, for example, lignites.

### The Desired Gas Quality Versus the Process Conditions

Dry gas from Koppers–Totzek gasification plant mainly contains CO and  $H_2$ . The ratio of these two components and the gas heating value change to a small degree for all coals. It is interesting to know whether these small changes are characteristic features of the Koppers–Totzek process or they result from the process parameters.

The manufacturing of gas of the required ratio  $H_2$  : CO (RMR) is an important problem when producing gas for chemical syntheses. For the process such as OXO, methanol or SNG syntheses this ratio should be between 1.3 and 3.2.

In order to investigate how and if it is possible to produce gases of desired levels of  $H_2$  : CO ratio or of desired heating values, two types of programmes were adopted.

The first case requires only building into the base model the Equation (29), while the second one only the Equation (30).

$$n_{H_2} = RMR \cdot n_{CO} \quad (29)$$

$$n_{H_2} \cdot 10.80 + n_{CO} \cdot 12.64 + n_{CH_4} \cdot 35.84 = RHV \cdot (n_{H_2} + n_{CO} + n_{CO_2} + n_{CH_4} + n_{N_2}) \quad (30)$$

As a result, both model structures have one more unknown variable, namely  $n_{O_2}^0$ .

The set of calculations to show the range of possible changes of RMR is presented in *Table 7* for coal defined in *Table 6*.

As can be seen the gas from the typical Koppers–Totzek process is an unsuitable feed for chemical syntheses. From the thermodynamical point of view it is possible, of course, to produce gas of RMR = 1.3, but this is technically unpracticable. To work at a temperature higher than the fusion point of ash it would be necessary to use extremely high quantities of gasification agents. From the above, it follows that the Koppers–Totzek process permits the control the RMR value in a very narrow range. More interesting is the gasification of crude residues (conf. data in *Table 4*) as its  $H_2$  : CO ratio is close to 1 for typical consumption of steam and oxygen. A possible solution is to get the RMR value between 1.3 and 3.2 in the utilization of gas shift conversion.

Table 4.

Comparison of thermodynamic calculations of gas composition (%mol) with commercial plant

Method, ref.	K-T [6]		K-T [7]		K-T [7]		K-T [8]		K-T [8]	
Feed	coal									
Feed comp. %wt										
C	49.4		56.8		61.9		55.2		79.9	
H	3.8		4.2		4.4		3.2		1.0	
S	0.1		0.7		4.9		0.8		0.8	
O	12.8		13.2		6.7		3.8		1.5	
N	0.7		1.0		1.0		0.9		0.3	
Moisture	7.8		2.0		2.0		1.0		1.0	
Ash	25.4		22.1		19.1		35.1		15.5	
Oxygen cons. Nm <sup>3</sup> /t of feed	483		455		494		548		701	
Steam cons. kg/t of feed	100		124		246		321		409	
Inlet temp. °C										
Oxygen	25		25		25		25		25	
Steam	350		350		350		350		350	
Feed	25		25		25		25		25	
Pressure, MPa	0.1		0.1		0.1		0.1		0.1	
Carbon conv. %	95.0		98.0		100.0		96.0		95.4	
Dry gas comp	Plant	Calc								
H <sub>2</sub>	31.0	31.7	33.0	33.3	35.3	35.9	31.2	29.6	21.1	21.3
CO	56.0	56.1	58.9	60.0	56.5	56.9	55.5	57.2	66.1	68.0
CO <sub>2</sub>	11.0	10.1	7.0	5.6	7.2	6.2	11.9	10.9	11.8	8.8
CH <sub>4</sub>	0.1	0.0	0.0	0.0	0.0	0.0	0.1	0.0	0.1	0.0
N <sub>2</sub>	1.9	2.2	1.1	1.1	1.0	1.0	1.3	2.3	0.9	1.9
Gas yield Nm <sup>3</sup> /kg of feed	1.28	1.32	1.39	1.60	1.60	1.83	1.52	1.51	1.90	1.94

The effect of the steam: oxygen ratio on the gas heating value was exemplified with the production of gas having a heating value 12.1 and 16.7 MJ/Nm<sup>3</sup>. The necessary calculations presented in *Table 8* were executed for coal defined in *Table 6* previously heated to 473 K to remove moisture, because in this case the gasification of moist coal results in temperatures below the fusion point of ash.

The production of gas with required heating value RHV = 12.1 MJ/Nm<sup>3</sup> is possible only for very small quantities of steam. The increase of the process pressure is not conducive to better results, because in temperatures higher than the ash melting point the equilibrium composition of reaction 9 strongly shifts to the left. The production of gas with RHV = 16.7 MJ/Nm<sup>3</sup> is impossible under atmospheric pressure. An increase of the process pressure does not ensure the required temperature and at the same time the RHV of gas. The possibilities of the process are limited to the production of gas with RHV equal about 11.0 MJ/Nm<sup>3</sup>.

From the above thermodynamic consideration it follows that Koppers-Totzek gasification is inflexible from the gas properties point of view.

results of Koppers-Totzek [5-10] and Shell [1] types

K-T [9]		K-T [10]		Shell [1]		Shell [1]		Shell [1]		Shell [1]	
coal		coal		light naphtha		fuel oil		vacuum residue		propane asphalt	
67.0		40.4		84.0		82.7		80.4		81.3	
4.9		3.1		16.0		11.0		9.7		9.1	
4.1		1.7		0.0		3.5		4.9		6.6	
7.0		15.7		0.0		1.5		2.3		1.5	
1.1		1.2		0.0		1.0		2.0		1.0	
2.0		8.0		0.0		0.2		0.6		0.4	
13.9		29.9		0.0		0.1		0.1		0.1	
590		338		875		721		721		665	
298		143		400		450		500		500	
25		25		246		246		246		246	
350		350		313		313		313		313	
25		120		25		246		246		246	
0.1		0.1		5.8		5.8		5.8		5.8	
95.0		98.0		97.0		97.0		97.0		97.0	
Plant	Calc	Plant	Calc	Plant	Calc	Plant	Calc	Plant	Calc	Plant	Calc
34.9	33.3	29.3	30.1	52.1	52.5	47.7	46.7	45.8	44.7	45.5	44.3
53.8	56.9	56.6	56.5	41.8	41.7	47.1	46.1	48.2	47.4	49.0	47.5
10.1	8.6	12.0	11.5	5.3	5.3	4.4	5.9	5.2	6.9	4.7	6.7
0.0	0.0	0.1	0.0	0.6	0.3	0.6	0.9	0.6	0.2	0.6	0.9
1.2	1.2	2.0	1.9	0.2	0.2	0.2	0.4	0.2	0.8	0.2	0.6
1.71	1.81	1.05	1.03	3.01	3.21	2.80	2.83	2.71	2.67	2.64	2.64

Table 5.

The influence of type of coal on the gasification process results.  $n_{O_2}^0 = 0.475$  mol  $O_2$ /mol DAF,  $n_{H_2O}^0 = 0.3$  mol  $H_2O$ /mol DAF, ash = 8 wt%, moisture = 10 wt%.

Coal type	Coal composition, wt%					kg $H_2O$ kg coal	kg $O_2$ kg coal	gasyield $Nm^3$ kg coal	gas heating value MJ/ $Nm^3$	equil temp $^{\circ}C$
	C	H	S	O	N					
lignite	70.2	5.3	0.8	22.7	1.0	0.259	0.726	1.543	9.957	1464
bituminous	80.3	4.7	0.3	13.1	1.6	0.296	0.877	1.745	10.268	1498
bituminous	82.3	5.1	0.4	10.6	1.6	0.304	0.893	1.827	10.376	1457
anthracite	91.0	4.1	0.7	2.8	1.4	0.336	0.988	1.953	10.581	1526
anthracite	92.0	3.2	1.3	2.1	1.5	0.339	0.989	1.896	10.537	1609

Table 6.

Coal composition.

Component	C	H	S	O	N	M	A
wt. fract.	0.6585	0.0385	0.0025	0.1074	0.0131	0.1000	0.0800

Table 7.

The possible range of molar ratio  $H_2/CO$  changes in gasification process of Koppers-Totzek type.

RMR	$n_{H_2O}^0$ mol $H_2O$ mol DAF		$n_{O_2}^0$ mol $O_2$ mol DAF		dry gasyield $\frac{Nm^3}{kg\ coal}$	dry gas compos., %mol					equil temp °C
	$H_2$	CO	$CO_2$	$CH_4$		$N_2$					
1.3	1.3	0.454	2.103	41.46	31.90	24.74	0.00	1.90	1061		
	1.6	0.498	2.045	39.65	30.50	27.76	0.00	2.09	1165		
1.0	1.0	0.556	1.991	38.14	38.14	21.69	0.00	2.03	1177		
	1.5	0.649	1.884	34.31	34.31	28.91	0.00	2.47	1382		
0.5	0.1	0.419	1.772	30.65	61.28	5.95	0.00	2.12	1207		
	0.25	0.473	1.731	28.83	57.66	11.14	0.00	2.37	1512		
	0.5	0.546	1.676	26.21	52.41	18.65	0.00	2.73	1770		

Table 8.

The gasification with steam and oxygen to achieve RHV of gas.

RHV MJ/ $Nm^3$	P MPa	$n_{H_2O}^0$ mol $H_2O$ mol DAF		$n_{O_2}^0$ mol $O_2$ mol DAF		gas yield $Nm^3/kg\ coal$	equilib. temp. °C
12.1	0.1	0.05	0.391	1.882	1250		
		0.10	0.365	1.942	994		
	3.0	0.05	0.394	1.877	1280		
		0.10	0.381	1.921	1153		
16.7	0.1	0.05	0.399	1.871	1321		
		0.10	0.389	1.911	1223		
	3.0	0.05	0.303	1.387	1248		
		0.10	0.274	1.433	978		
16.7	6.0	0.05	0.303	1.387	1248		
		0.10	0.275	1.433	984		

### Heat Losses Estimation Via the Thermodynamic Model

The presented thermodynamic model was used to describe autothermic gasification process. This model can, however, also be used to solve another problem. If the process temperature is known from the measurement, then heat losses may be directly calculated from the overall heat balance equation. Such computations were executed for coal from *Table 1* (the final temperature of gasification is equal 1500 °C). The estimated heat losses are equal to 6.1% of the heating value of DAF being in good accordance with the commercial results (4–7% of heating value of DAF [11]). As a result, the model presented can also be used for estimating the consistency of published data and commercial reports.

## Conclusions

The presented thermodynamic model of coal and crude residue gasification precisely describes all the important phenomena occurring in the Koppers-Totzek and Shell processes. It was proved by the comparisons the calculated compositions with commercial plant data.

The clear influence on the correctness of the results exhibits the degree of carbon conversion, affecting in the first place the heat balance equation. When the degree of carbon conversion is not known from industrial data, then  $\alpha_c = 0.97$  is recommended.

The important conclusion resulting from the thermodynamic calculations is that Koppers-Totzek and Shell gasification processes can be used for very different feeds. The coal type has a minor influence on gas composition. The process technology is, however, not flexible enough to manufacture gases of different compositions. The heating value of the gas does not depend on the process parameters. At typical process temperatures, the reaction (9) is shifted to the left, resulting in low methane amounts and consequently in a low heating value of the manufactured gases.

## Symbols

$A_0$ – $A_4$	constants in Equation 20
$a, b, c, d$	amounts of H, S, O, N gramm-atoms corresponding to one mole of gasified coal, respectively
$e, f$	amounts of moisture and ash moles corresponding to one mole of gasified coal, respectively
$\Delta G_f^0$	standard Gibbs free energy of formation, kJ/mol
$g$	weight fraction
$\Delta H_f^0$	standard enthalpy of formation, kJ/mol
$\Delta H_{m, ash}^0$	ash fusion enthalpy, kJ/mol
$H_T^0 - H_{298}^0$	standard enthalpy difference in temperatures T and 298 K, kJ/mol
$K$	equilibrium constant
$M$	atomic or molecular weight, g/mol
$M_{DAF}$	molecular weight of one mole of dry ash-free coal, g/mol
$n$	number of moles at equilibrium
$n^0$	number of moles in feed corresponding to one mole of gasified coal
$P, P^0$	process and reference pressure, respectively, bar
$Q_{DAF}$	heating value of dry ash-free coal, kJ/mol
$Q_{losses}$	heat losses, kJ/mol
RHV	required heating value, MJ/Nm <sup>3</sup>
RMR	required molar ratio of $H_2$ : CO
$T$	temperature, K
$V$	mole ratio of $N_2$ : $O_2$ in technical oxygen or in air
$\alpha_c$	carbon conversion

## References

1. KUHRE, C. J. and REED C. L.: *Oil and Gas Journal* 1976, 74, 2, 110.
2. STULL, D. R. and PROPHET, H.: *JANAF Thermochemical Tables NSRDS-NBS 37*, Washington, 1971.
3. CHANIN, J. M. and JUSZYN, W. W.: *Bilans materiałowy i ciepłoty pieców koksowniczych*, PWT, Warszawa, 1952.
4. RAZNIEVICZ, K.: *Handbook of Thermodynamic Tables*, Hemisphere Publishing, London, 1976.
5. OSTHAUS, K. H.: *Coke and Gas*, 1962, 24, 279, 315.
6. WINNACKER, J. and KUHLER, J.: *Chemische Technologie*, Vol 3. Carl Hanser Verlag, Munich, 1971.
7. FARNWORTH, J. F., LEONARD, H. F., MITSAH, D. M. and WINTRELL, R.: *V Symp. SNG*, Chicago, 1973, Vol 1, p. 21.
8. OSTHAUS, K. H. and AUSTEN, T. W.: *Gas World* 1963, 12 Jan., p. 98.
9. MICHAELIS, H. J., and LEONARD, H. F.: *Chem. Eng. Progr.* 1978, 74, 8, 35.
10. STAEGE, H.: *Die Kohlevergasung nach Koppers-Totzek Sonderdruck nach dem Beitrag in Technic International*.
11. KOWALSKI, J.: *Wytwarzanie gazu do syntezy*, PWT, Warszawa, 1954.

## OPTIMAL LOAD OF ENERGY SUPPLY SYSTEMS (ESS) DURING THE PERFORMANCE OF MULTIPURPOSE CHEMICAL PLANS\*

B.B. IVANOV, MS.N.GR. VAKLIEVA-BANCHEVA, and CHR. B. BOYADJIEV

(Bulgarian Academy of Sciences, Institute of Chemical Engineering, "Acad. Bonchev" str. b.  
103, Sofia 1040, Bulgaria)

Received: October 5, 1989

\*The project was completed with the financial support of the Ministry of Culture, Science and Education of Bulgaria under the contract No. 162.

A description of a method to optimize the load of the energy supply system [ESS] for the parallel production of several products in a multipurpose batch chemical plant for a fixed period of time is proposed.

The energy consumption for a single production – the partial energy consumption and for all  $N$  productions – and the total energy consumption are assumed to be periodic functions of time. The methods of Fourier analysis were used to formulate and solve the corresponding mathematical model. An optimization problem was formulated as a nonlinear programming problem without restrictions. Standard procedures were used to solve a problem.

The brief description of FORTRAN-77 implementation of the method and a simple test example are also discussed.

### Introduction

During the last years, economy problems and reasonable utilization of energy became increasingly important in the chemical industry. Chemical engineers and designers currently develop methods for the design of chemical plants with decreased energy consumption and for the optimal energy consumption of existing plants.

The synthesis problems for recuperative heat exchanger subsystems of chemical plants were studied in the special literature. Problems concerning the synthesis of flexible energy supply subsystems [1, 2] are currently investigated.

Reports on the design of batch chemical plants with decreased energy consumption were published only recently. KNOPF et. al. [3] introduced in the

problem for the optimal design of batch plants correlation accounting for the energy consumption. VASELENAK et. al. [4] proposed a method for energy recuperation by an appropriate heat integration of batch processes. This method is useful to obtain estimates for the degree of energy utilization in multi-product chemical plants.

The problems concerning the optimal operational control of multipurpose batch chemical plants, accounting for the capabilities of the corresponding energy supply subsystem (ESS) have not been discussed in the available literature, although they are particularly important for the effective utilization of energy in the existing multipurpose batch chemical plants.

The aim here is to present a method for the control of a set of batch chemical productions. The method guarantees optimal loading of the ESS of multipurpose batch chemical plants.

### Batch Chemical Plants as Energy Consumers

To clarify this, it is necessary to discuss what is a batch chemical plant as an energy consumer and which are the factors determining its energy consumption.

Generally, a batch plant can be considered as a set of batch production lines, characterized by particular energy consumptions for fixed periods of time. The lines are interrelated with respect to their individual energy consumptions, because they have hard connections with the ESS of the batch plant. The total energy consumption of the plant, *Fig. 1*, is determined by the joint performance of the production lines.

Consequently, the production line is a basic element, the performance of which determines the energy consumption of the batch plant. For the purpose

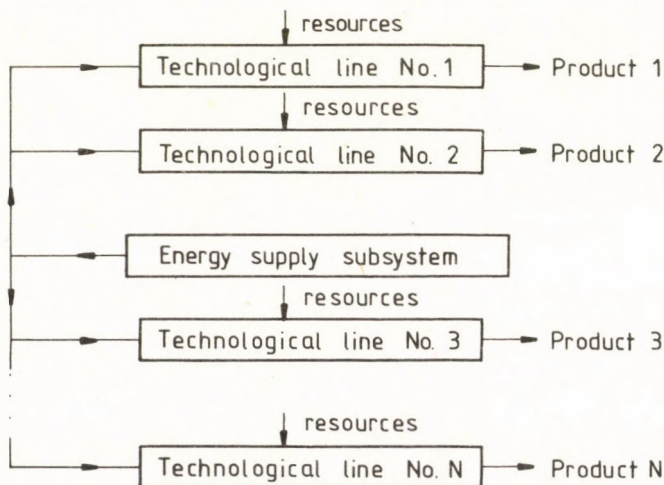


*Fig. 1*

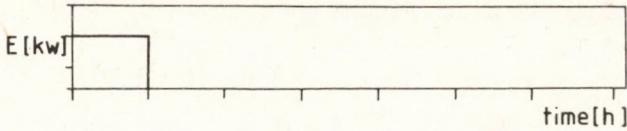


Fig. 2a.

The local energy consumption – time curve for a single stage

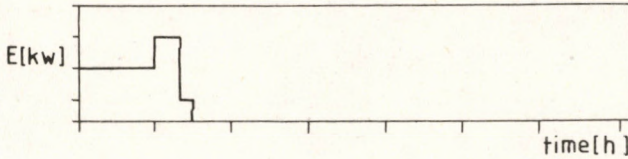


Fig. 2b.

The partial energy consumption – time curve for a single technological line necessary to produce one batch of the product

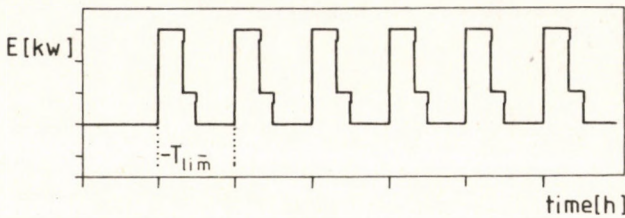


Fig. 2c.

The partial energy consumption – time curve for an overlapping operation batch chemical line

of energy consumption control, the production line can be considered as consisting of production units. In each of these, some production stage is being realized. Each production stage is characterized by some particular energy consumption – the local energy consumption. If it is assumed that the stage is realized in a single unit with constant energy consumption, the relationship between local energy consumption and time is of the form, shown in Fig. 2a. In practice, this relationship is much more complicated, but for simplicity it will be assumed that the fluctuations of energy consumption for one stage are small and can be neglected. If the energy consumption curves for all stages are known, one can determine the energy consumption for the whole line, necessary to produce one (Fig. 2b) or more batches of the product (Fig. 2c) called the partial energy consumption function.

Because the whole equipment is loaded periodically, the partial energy consumption function can also be considered periodic. Among all stages of the production line, a particular stage can be found, which performs longer than

the rest. This stage is called the limiting stage, and the time necessary for it – the limiting time [5]. The limiting time determines the period of the partial energy consumption curve for an overlapping operation batch chemical line, *Fig. 2c*.

It is known [5] that depending on their structure and performance, batch chemical plants can be classified as multiproduct and multipurpose batch plants. If a fixed sequence of production units is used to produce only one product at a time, one has a multiproduct batch plant. If a set of production units is used in different arrangements to produce one or more products at a time, one has a multipurpose batch plant. Consequently, for multipurpose plants, the groups of products and the equipment for their production can vary in one planning period.

It is natural to assume that in the course of parallel production of two or more products in a multipurpose batch chemical plant, the load of the ESS is the sum of the partial energy consumption of the separate batch periodic lines. In such cases, the energy consumption curve – called the total energy consumption curve – often has peaks, which overrun the capacity of ESS, *Fig. 3a*. Thus, one has to solve the problem: how to control the performance of the multipurpose batch

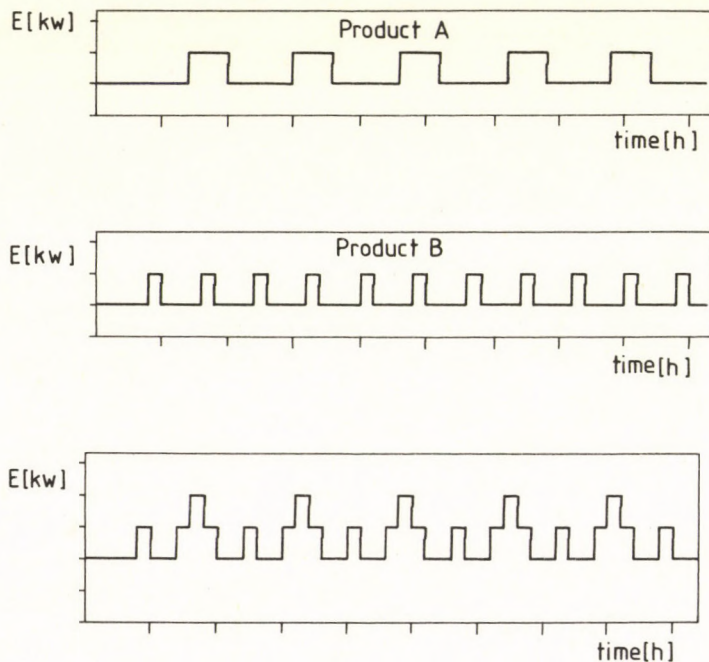


*Fig. 3a.*

The partial energy consumption-time curve to produce a product A.

The partial energy consumption-time curve to produce a product B.

The total energy consumption for a parallel production of products A and B without shifts.

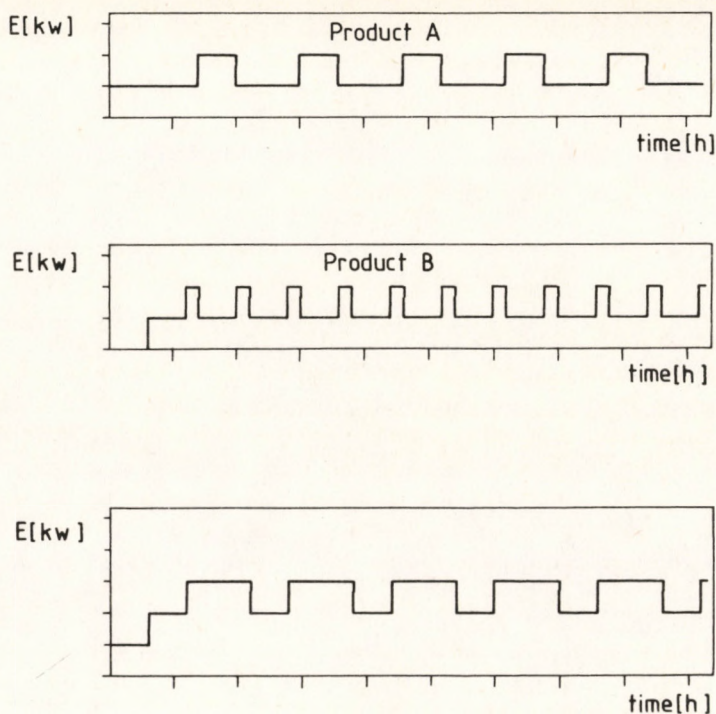


*Fig. 3b.*

The partial energy consumption-time curve to produce a product A.  
 The partial energy consumption-time curve to produce a product B. with shift  
 The total energy consumption-time curve for parallel production of products A and B with shift.

plants so that the load of the ESS is as uniform as possible. One solution to this problem is to find appropriate phase shifts for the starting times of the productions of the separate products, which will result in the smoothing of the total energy consumption curve, *Fig. 3b*. A solution will be referred to for control at this level of a production line.

Consequently, the control at the level of a production line of the multipurpose batch chemical plants with a criterion – the uniform load of the ESS – can be realized by an appropriate choice of the starting times of the separate productions.

### Method for Control of Multipurpose Batch Chemical Plants with Optimal Loads of the ESSs

The goal of this method for control of the multipurpose batch chemical plants guaranteeing optimal loads of the ESSs is to find such starts  $x_i$ ,  $i = 1, N-1$  ( $N$  is the number of parallel-working production lines in a fixed

period of time) of the partial energy consumption curves (with respect to one of them, which is assumed to be the reference curve) so that the load of the ESS (the total energy consumption curve) is as uniform as possible. As far as the partial energy consumption functions of the separate productions are assumed periodic for some time interval, the total energy consumption function (for all productions) will be assumed to be periodic, too. This enables the use of the methods of Fourier analysis to obtain the corresponding functions in an analytic form. Thus a periodic function can be expanded in an infinite series and can be represented as the sum of a constant component plus the cosine and sine components of the different harmonics. In practice a finite number of harmonics are used and the accuracy of the truncated representation of a particular function depends on the number of harmonics used in the truncated expansion.

To find an analytic expression for the energy consumption function of a particular production – the partial energy function, it is necessary to introduce the energy consumption functions for each stage of the production – the local energy functions and determine the coefficients in the Fourier expansion. By summing these coefficients for the harmonics of all stages, one obtains the Fourier coefficients for the partial energy consumption function of the particular production. This can be done for all  $N$  production lines to obtain the analytic expressions for the total energy consumption.

The total energy consumption function for  $N$  parallel-working batch production lines can be obtained through the Fourier expansion of the sum of the partial energy consumption functions.

Next, it is necessary to determine the optimal time shifts of the partial energy consumption functions subject to the additional requirement that the total energy consumption function for all production lines has a minimal amplitude of the oscillations. To do this, one tries to localize the minimum  $P$  of the area  $F$  enclosed by the constant and the variable components of the periodic function, thus determining the optimal shifts  $x_i$ ,  $i = 1, 2, \dots, N-1$ , of the partial functions with respect to the reference one:

$$P = \min_{x_1, x_2, \dots, x_{N-1}} F(x_1, x_2, \dots, x_{N-1}). \quad (1)$$

The values of the arguments  $(x_1^0, x_2^0, \dots, x_{N-1}^0)$  corresponding to the minimum value  $P$  of  $F$  define the optimum starting times of the production lines.

### The Mathematical Model

It is known [6] that every periodic function  $\psi(t) = \psi(t+T)$  with period  $T > 0$  can be expanded in a Fourier series:

$$\psi(t) \approx \frac{y_0}{2} + \sum_{k=1}^g [A_k \sin(k\omega t) + B_k \cos(k\omega t)], \quad -T \leq t \leq T, \quad (2)$$

where  $y_0$  is the constant component;  $A_k$  and  $B_k$  – the Fourier coefficients. The latter are defined by:

$$A_k = \frac{2}{T} \int_0^T \psi(t) \sin(k\omega t) dt \quad (3)$$

$$B_k = \frac{2}{T} \int_0^T \psi(t) \cos(k\omega t) dt \quad (4)$$

$$y_0 = \frac{2}{T} \int_0^T \psi(t) dt \quad (5)$$

The partial energy consumption function  $F_{\text{par}}^i(t^i)$  for  $i$ -th technological line, Fig. 2c is a periodic function with period  $T_{\text{lim}}^i$ . So it can be expanded as a Fourier series, (Eq. (2)), too. To have the function  $F_{\text{par}}^i(t^i)$  completely determined, one has to know the values of the coefficients  $A_k^i$  and  $B_k^i$ . The coefficients of the partial function  $F_{\text{par}}^i(t^i)$  can be obtained as sums of the Fourier coefficients of the functions  $f_j^i(t_j)$ , reflecting the local energy consumption-time relationship for stages  $j, j = 1, 2, \dots, m^i$ .

The Fourier coefficients of the local energy consumption function  $f_j^i(t_j)$  for the  $j$ -th stage of the  $i$ -th production can be written as:

$$A_{jk}^i = \frac{2}{T_{\text{lim}}^i} \int_0^{T_j^i} f_j^i(t_j) \sin(k\omega^i t_j) dt_j \quad (6)$$

$$B_{jk}^i = \frac{2}{T_{\text{lim}}^i} \int_0^{T_j^i} f_j^i(t_j) \cos(k\omega^i t_j) dt_j \quad (7)$$

$$y_{j0}^i = \frac{2}{T_{\text{lim}}^i} \int_0^{T_j^i} f_j^i(t_j) dt_j \quad (8)$$

where  $\omega^i = \frac{2\pi}{T_j^i}$  is angular frequency [ $s^{-1}$ ];  $k$  - the order of the harmonic;  $t_j$  - time [ $s$ ];  $T_j^i$  - the time necessary to realize the  $j$ -th stage of the  $i$ -th production;  $f_j^i(t_j)$  - the value at time  $T_j^i$  of the  $j$ -th energy consumption function [ $W$ ],  $0 \leq t_j \leq T_j^i$ , which is assumed to be constant:

$$f_j^i(t_j) = E_j^i = \text{const}, \quad 0 \leq t_j \leq T_j^i$$

The dimensions of  $A_{jk}^i$ ,  $B_{jk}^i$  and  $y_{j0}^i$  are the same of  $f_j^i(t_j)[W]$ .

Under the latter assumption Eqs. (6)-(8) yield:

$$A_{jk}^i = \frac{E_j^i \left[ 1 - \cos\left(k \frac{2\pi}{T_{\text{lim}}^i} T_j^i\right) \right]}{k\pi} \quad (9)$$

$$B_{jk}^i = \frac{E_j^i \cdot \sin\left(k \frac{2\pi}{T_{\text{lim}}^i} T_j^i\right)}{k\pi} \quad (10)$$

$$y_{j0}^i = \frac{E_j^i T_j^i}{T_{\text{lim}}^i}. \quad (11)$$

Thus, for the Fourier coefficients of the partial function  $F_{\text{par}}^i(t^i)$ , which is the energy consumption of the  $i$ -th production line one has:

$$A_k^i = \sum_{j=1}^{m^i} A_{jk}^i = \sum_{j=1}^{m^i} \frac{E_j^i \left[1 - \cos\left(k \frac{2\pi}{T_{\text{lim}}^i} T_j^i\right)\right]}{k\pi} \quad (12)$$

$$B_k^i = \sum_{j=1}^{m^i} B_{jk}^i = \sum_{j=1}^{m^i} \frac{E_j^i \cdot \sin\left(k \frac{2\pi}{T_{\text{lim}}^i} T_j^i\right)}{k\pi} \quad (13)$$

$$y_0^i = \sum_{j=1}^{m^i} y_{j0}^i = \sum_{j=1}^{m^i} \frac{E_j^i \cdot T_j^i}{T_{\text{lim}}^i} \quad (14)$$

while for the partial function:

$$F_{\text{par}}^i(t^i) = y_0^i + \sum_{k=1}^m (A_k^i \sin(k\omega^i t^i) + B_k^i \cos(k\omega^i t^i)), \quad 0 \leq t^i \leq T_{\text{lim}}^i. \quad (15)$$

The analytic expression for the total energy consumption  $F_{\text{gen}}(t)$  reflecting the parallel performance (for some fixed period of time) of  $N$  production lines is:

$$F_{\text{gen}}(t) = \sum_{i=1}^N F_{\text{par}}^i(t^i), \quad 0 \leq t \leq T_{\text{gen}}: \quad (16)$$

$$F_{\text{gen}}(t) = \sum_{i=1}^N \left( y_0^i + \sum_{k=1}^m (A_k^i \sin(k\omega^i t^i) + B_k^i \cos(k\omega^i t^i)) \right), \quad (17)$$

$$F_{\text{gen}}(t) = \sum_{i=1}^N y_0^i + \sum_{i=1}^N \sum_{k=1}^m (A_k^i \sin(k\omega^i t^i) + B_k^i \cos(k\omega^i t^i)), \quad (18)$$

$$F_{\text{gen. c}} = \sum_{i=1}^N y_0^i,$$

$$F_{\text{gen. v}}(t) = \sum_{i=1}^N \sum_{k=1}^m (A_k^i \sin(k\omega^i t^i) + B_k^i \cos(k\omega^i t^i))$$

$$F_{\text{gen}}(t) = F_{\text{gen. c}} + F_{\text{gen. v}}(t).$$

The function  $F_{\text{gen. v}}(t)$  is the time-dependent component of the energy consumption and it represents the oscillations of the energy consumption around the constant component  $F_{\text{gen. c}}$ . Next, it is necessary to locate the minimum of  $F_{\text{gen. v}}$  as a function of the control variables  $x_1, x_2, \dots, x_{N-1}$ ,

$$F_{\text{gen. v}}(t) = > F_{\text{gen. v}}(\tau) \Rightarrow F(x_1, x_2, \dots, x_{N-1}).$$

To do this we introduce in Eq. (18) the parameters  $x_i$ , according to the shifts of the partial functions, thus changing the independent variable  $t$  by  $\tau = t^N$  and  $t^i = \tau - x_i$  for  $i = 1, 2, \dots, N-1$ ,  $0 \leq \tau \leq T_{\text{gen}}$ .

$$F_{\text{gen}, v}(\tau) = \sum_{i=1}^{N-1} \sum_{k=1}^m [A_k^i \sin(k\omega^i(\tau - x_i)) + B_k^i \cos(k\omega^i(\tau - x_i))] + \sum_{k=1}^m [A_k^N \sin(k\omega^N \tau) + B_k^N \cos(k\omega^N \tau)], \quad (19)$$

Next we integrate the variable component  $F_{\text{gen}, v}(\tau)$  in the limits  $0 \leq \tau \leq \frac{3T_{\text{gen}}}{4}$ , where  $T_{\text{gen}}$  is the period of  $F_{\text{gen}}$  to obtain the function  $F(x_1, x_2, \dots, x_{N-1})$ :

$$F = \sum_{i=1}^{N-1} \sum_{k=1}^m \left\{ \frac{1 - \cos\left(k\omega^i \frac{3T_{\text{gen}}}{4}\right)}{k\omega^i} [A_k^i \cos(k\omega^i x_i) + B_k^i \sin(k\omega^i x_i)] + \frac{\sin\left(k\omega^i \frac{3T_{\text{gen}}}{4}\right)}{k\omega^i} [B_k^i \cos(k\omega^i x_i) - A_k^i \sin(k\omega^i x_i)] \right\} + \sum_{k=1}^m \left\{ \left[ 1 - \cos\left(k\omega^N \frac{3T_{\text{gen}}}{4}\right) \right] A_k^N + \sin\left(k\omega^N \frac{3T_{\text{gen}}}{4}\right) B_k^N \right\} \quad (20)$$

The function  $F$ , Eq. (20), is nonlinear in its variables and it is not subject to any restrictions. One can use gradient methods to locate its extrema, because the expressions for its partial derivatives are readily available:

$$\frac{\partial F}{\partial x_i} = \sum_{i=1}^{N-1} \sum_{k=1}^m \left[ 1 - \cos\left(k\omega^i \frac{3T_{\text{gen}}}{4}\right) \right] [B_k^i \cos(k\omega^i x_i) - A_k^i \sin(k\omega^i x_i)] - \sum_{i=1}^{N-1} \sum_{k=1}^m \sin\left(k\omega^i \frac{3T_{\text{gen}}}{4}\right) [B_k^i \sin(k\omega^i x_i) + A_k^i \cos(k\omega^i x_i)], \quad i = 1, 2, \dots, n-1. \quad (21)$$

Formally the minimum  $P$  of  $F$  will correspond to a situation when the time variable component  $F_{\text{gen}, v} \leq F_{\text{gen}, c}$ ,  $0 \leq t \leq T_{\text{gen}}$ . This has no physical sense and, therefore, we try to localize the minimum  $P$  of the function  $F^2$ .

### The Programme Implementation and an Illustrative Example

The method for controlling a group of parallel-working batch chemical lines guaranteeing an optimal load of the ESS of multipurpose batch plants was programmed in FORTRAN-77. The package developed comprises 12 computing and processing programme units, which perform on PC IBM/AT and compatibles. They allow for dialogue input and correction of input data and also for control and analysis of the solution obtained. The design of the package allows the organization of the calculations in an overlay structure, which results

in a considerable decrease of the core memory requirements with an insignificant increase of the computational time.

The package was first tested with simple data, making a check of the output results easy and enabling one to observe in detail how the method and the programme units work.

The following simple example concerns three productions AAA1, BBB1 and CCC1 with overlapping operation times to illustrate the method for controlling a group of parallel-working batch production lines with an optimal load of the ESS of the multipurpose batch chemical plant. The input data are listed in *Table 1*.

*Table 1*

name of technology	AAA1		BBB1		CCC1	
	1	2	1	2	1	2
No of stage	1	2	1	2	1	2
time for performing stage [h]	2	6	3	6	4	6
energy consumption of stage [kW]	$3 \cdot 10^2$	$10^2$	$3 \cdot 10^2$	$2 \cdot 10^2$	$2 \cdot 10^2$	$10^2$

*Fig. 4a* shows the load of the ESS, when all three productions are started simultaneously. In the course of one period, the maximum load is  $12.7 \cdot 10^2$  [kW], and the minimum –  $3.38 \cdot 10^2$  [kW].

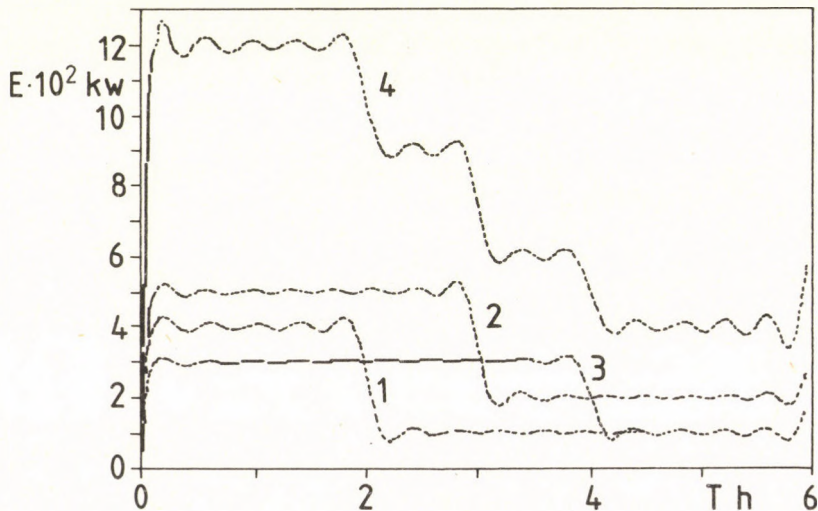


*Fig. 4a.*

Energy consumption – time functions  
 1 – for production AAA1 without shift  
 2 – for production BBB1 without shift  
 3 – for production CCC1 without shift  
 4 – total function without shifts.

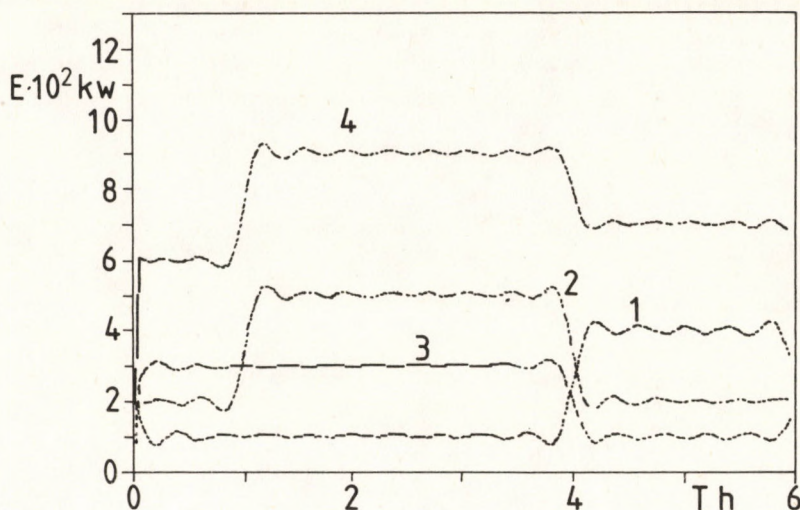


Fig. 4b.

Energy consumption - time functions  
 1 - for production AAA1 without shift  
 2 - for production BBB1 without shift  
 3 - for production CCC1 without shift  
 4 - total function with shifts.

The optimal load of the ESS when the three productions work in parallel is obtained when production CCC1 is switched on at the (conditional) zero of the time, production BBB1 - one hour later and production AAA1 - 3 hours after BBB1. In this case the maximum load of ESS is  $9.12 \cdot 10^2$  [kW] while the minimum is  $5.78 \cdot 10^2$  [kW]. The total energy consumption function for the system under optimal loading is shown on Fig. 4b.

### Conclusions

We propose a method for the control of batch chemical lines working in parallel with the optimal load of the ESS of a multipurpose chemical plant. It is valid for control at the level of a production line with an optimality criterion directly reflecting the energy consumption of the N production lines for a given period of time. The control variables are the switch-on times for the separate productions.

The method is based on the following assumptions: the local energy consumption (of a production stage) is constant; the partial energy consumptions (of a single technological line) is periodic; the total energy consumption (of N parallel-working technological lines at a given period of time) is periodic too. A mathematical model for the total energy consumption is developed and solved

with the methods of Fourier analysis. An optimal control problem is formulated like a nonlinear optimization problem without restrictions.

A programme package was developed to implement the method on a computer and the test results with a simple set of data are discussed.

#### References

1. PAPOULIAS S. A., GROSSMANN I. E.: 18th IECEC, 2066-2071
2. PAPOULIAS S. A., GROSSMANN I. E.: *Computers & Chem. Eng.*, 1983, 7, (6) 695-706.
3. KNOPF F. C. and OKOS M. R., REKLAITIS B. V.: *Ind. Eng. Chem. Process Des. Dev.*, 1982, 21 (1), 79-86.
4. VASELENAK J. A., GROSSMANN I. E., and WESTERBERG A. W., *Ind. Eng. Chem. Process Des. Dev.*, 1986, 25 (2), 257-366.
5. SPARROW R. E., RIPPIN D. W. T., and FORDER G. J., *Chem. Eng.*, 1974, No. 289, 520-525.
6. KORN G. A., and KORN T. M., *Mathematical handbook*, McGraw-Hill Book Company, New York, San Francisco, Toronto, London, Sydney, 1968.

## **SIMULATION OF CARBON DIOXIDE ABSORPTION INTO SODIUM HYDROXIDE SOLUTION IN A NUTTER-VALVE PLATE COLUMN**

E. BÉKÁSSY-MOLNÁR\*, W. MONIUK, H. MUSTAFA\*, and R. POHORECKI

(\* Department of Chemical Engineering, Technical University of Budapest, H-1521, Budapest, Hungary. Institute of Chemical and Process Engineering, Warsaw Technical University, Waryńskiego I, PL-00-645 Warsaw, Poland)

Received: October 16, 1989

The profiles of temperature, concentrations and hydrodynamic parameters along the column height were simulated for the absorption of carbon dioxide into a sodium hydroxide solution of total concentration up to 4.4 N in a Nutter-valve plate column. The influence of the CO<sub>2</sub> concentration in the gas phase on the temperature and concentration profiles was estimated. The results of simulation were compared to an experiment for the case of low concentration of CO<sub>2</sub> in the gas phase (~1%) and low concentration of NaOH solution (~1 N). Comparison of the Nutter-valve and sieve plate columns is also presented.

### **Introduction**

In the work [1] a general method permitting the evaluation of the point and Murphree plate efficiencies for absorption with first, pseudo-first and second order chemical reactions was presented. In an earlier paper [2] the above method was verified experimentally for the absorption of carbon dioxide into aqueous sodium hydroxide solutions in a sieve plate column.

The aim of the present work was to simulate the process of CO<sub>2</sub> absorption into a NaOH solution in a Nutter-valve plate column. The results of simulation were compared with an experiment for the case of low concentrations of CO<sub>2</sub> in the gas phase and not highly concentrated NaOH solution.

A comparison of the Nutter-valve and sieve plate columns is also presented.

The measurements were carried out in a column with 5 Nutter-valve plates with downcomers. The internal diameter of the column was 400 mm, tray spacing - 350 mm. A sketch of the apparatus was given in an earlier paper [2].

The arrangement of the valves on a plate is shown in *Fig. 1*. The geometrical characteristics of the Nutter-valve and the sieve plates are given in *Tables 1* and *2*. The measured quantities were the following: temperature, gas and liquid flow rates, concentrations of the liquid and gas phases, total pressure drop across a plate, clear liquid height, liquid weeping rate, and froth height.

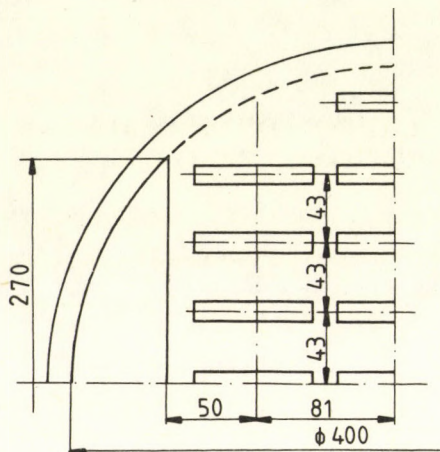


*Fig. 1.*

The arrangement of the valves on a plate.

*Table 1.*

Geometrical characteristics of Nutter-valve plates

	$f_a$ (%)	$f$ (%)	$h_w$ (mm)	number of valves	valve weight (g)	valve hole size (mm × mm)	valve size (mm × mm)
1	18.5	14.7	25	23	19.9	68 × 12	68 × 15
2	18.5	14.7	50	23	19.9	68 × 12	68 × 15

*Table 2.*

Geometrical characteristics of sieve plates

	$f_a$ (%)	$f$ (%)	pitch (mm)	$d_o$ (mm)	$h_w$ (mm)	number of holes
1	4.5	3.6	18	4.3	25	309
2	4.5	3.6	18	4.3	50	309
3	9.6	7.6	14.5	4.9	25	509
4	9.6	7.6	14.5	4.9	50	509
5	14.4	11.5	14.5	6.0	25	509
6	14.4	11.5	14.5	6.0	50	509

The working conditions of the column with the Nutter-valve plates were as follows:

temperature: 16–18 °C

gas pressure: 1,008–1,031 bar

initial concentration of CO<sub>2</sub> in the gas phase: 1.02% vol.

gas flow rate: 0.074–0.251 m<sup>3</sup>/s ( $u_g = 0.5$ –2.0 m/s)

liquid flow rate: (0.26–6.94) 10<sup>-4</sup> m<sup>3</sup>/s

initial concentration of the solutions:

NaOH: 0.65–1.07 kmol/m<sup>3</sup>

Na<sub>2</sub>CO<sub>3</sub>: 0.005–0.22 kmol/m<sup>3</sup>

A detailed description of the apparatus and a measuring technique can be found in reference [3].

### Method of Simulations

The method of simulations of the absorption process in the column is based on the "plate efficiency" concept, making use of the point efficiency, defined as:

$$E_{og} = \frac{y_{n-1} - y}{y_{n-1} - y_n^*} \quad (1)$$

and Murphree plate efficiency, defined as:

$$E_{MV} = \frac{y_{n-1} - y_n}{y_{n-1} - y_n^*} \quad (2)$$

In the process of CO<sub>2</sub> absorption into aqueous sodium hydroxide solutions, in considered conditions, the reaction of CO<sub>2</sub> with OH<sup>-</sup> ions could be treated as a fast irreversible pseudo-first order reaction (appropriate criteria are given in references [4, 5]).

In this case ( $y^* = 0$ ), the Murphree plate efficiency can be determined from the diagrams [1]:

$$\frac{E_{MV}}{E_{og(1)}} = f[E_{og(1)}, Pe, \lambda_{(1)}^*] \quad (3)$$

where:

$$E_{og(1)} = 1 - \exp \left[ \frac{-1}{1/N_g + 1/N_{L(1)}^*} \right] \quad (4)$$

$$N_g = \frac{k_g a P h_f}{G_M} \quad (5)$$

$$N_{L(1)}^* = \frac{\sqrt{D_A k_{OH^-} - c_{BO(1)}} a h_f P H}{G_M} \quad (6)$$

$$Pe = \frac{u_L l}{D_E} \quad (7)$$

$$\lambda_{(1)}^* = \frac{bG_M y_{n-1}}{S(1-\varepsilon)u_L c_{BO(1)}} \quad (8)$$

Typical diagram valid for the considered conditions of this work are given in reference [2].

The physical mass transfer coefficients in the gas and liquid phases (necessary for the evaluation of the reaction regime) were calculated from the correlations [6]:

$$k_g a = G_M / Ph_f (1565 \sqrt{D_g / u_g} + 6.09 h_f + 19.9 h_w + 1.56) \sqrt{\mu_g / (\mu_g + \mu_L)} \quad (9)$$

$$k_L a = L / Ah_f (4388 + 7265 F) \left( \frac{h_f l}{V_L / z} \right)^{0.8364 D_A^{0.5}} \quad (10)$$

where

$$F = u_g \sqrt{\rho_g} \quad (11)$$

The axial dispersion coefficient was estimated from the correlation [6]:

$$\frac{u_L^{0.6}}{D_E} = 190 (V_L / z)^{0.54} \frac{500 V_L / z}{5.2 h_w + 0.02} - 28.6 F \left( \frac{V_L}{z} \right)^{0.5} \quad (12)$$

The interfacial area per unit froth volume on the plate was measured experimentally [3].

The values of the Henry's and reaction rate constants as well as the properties of gas and liquid phases were calculated from the relationships given in reference [2].

For higher concentrations of  $\text{CO}_2$  in the gas phase, more concentrated solutions and in cases, when gas is not saturated by solvent before entering the first plate, one should take into account the heat balance equation (allowing for heat effects of absorption, reaction and solvent evaporation):

$$V_L \rho_L c_p \Delta t = N_{\text{CO}_2} q + N_{\text{H}_2\text{O}} q_w \quad (13)$$

The molar flux of carbon dioxide and water vapour can be calculated from the relationships:

$$N_{\text{CO}_2} = G'_M (y_{n-1} - y_n) \quad (14)$$

$$N_{\text{H}_2\text{O}} = k_g a Ah_f (p_r - p_{\text{H}_2\text{O}}) \quad (15)$$

In the work [7] the value of the equilibrium pressure of water vapour over concentrated aqueous sodium hydroxide and sodium carbonate solutions (total concentration up to 4.4 N) was determined. Using the Dühring method, the following dependence of water vapour pressure on temperature was established for the above solutions.

$$\log p_r = 6.066 - \frac{2283.4}{T} \quad (16)$$

This relationship is valid in the range of temperatures 20–45 °C.

In the process of CO<sub>2</sub> absorption in NaOH solutions the heat of dissolution of CO<sub>2</sub> equals [8]:

$$q_A = 19.4 \cdot 10^3 \text{ kJ/kmol}$$

and the heat of reaction [8]:

$$q_R = 89.2 \cdot 10^3 \text{ kJ/kmol}$$

Hence the total heat effects equals:

$$q = q_A + q_R = 108.6 \cdot 10^3 \text{ kJ/kmol} \quad (17)$$

The heat of water vaporization was determined from relationship [9]:

$$q_w = 40,620 \left( 2.3615 - \frac{T}{274.1} \right)^{0.38} \quad (18)$$

Specific heat of the above solutions equals [10]:

$$c_p = 3.6 \text{ kJ/kgK}$$

Making use of Eqns. (3) and (13) and assuming for the next (n) plate:

$$c_{\text{BO}(1)(n)} = c_{\text{BO}(1)(n-1)} + 2N_{\text{CO}_2}/V_L \quad (19)$$

$$c_{\text{DO}(1)(n)} = c_{\text{DO}(1)(n-1)} - N_{\text{CO}_2}/V_L \quad (20)$$

$$y_n = y_{n-1}(1 - E_{\text{MV}}) \quad (21)$$

$$t_{(n)} = t_{(n-1)} + \Delta t \quad (22)$$

$$V_{g(n)} = V_{g(n-1)} + \Delta V_g \quad (23)$$

$$V_{L(n)} = V_{L(n-1)} + \Delta V_L \quad (24)$$

we obtain the profiles of concentrations, temperature and flow rates along the column.

Simulation of the absorption process in the column was started at the bottom plate (n = 1).

The input data were as follows:

- the outlet liquid flow, composition and temperature,
- the inlet gas flow, composition, temperature and pressure.

Calculations, simulating the process of CO<sub>2</sub> absorption, were carried out for NaOH solution of total concentration 4.4 N, varying the gas concentration at the inlet of column from 1 to 20%. The calculations were performed assuming as a starting value of the liquid temperature at the outlet of column equal to 40 °C.

### Results and Discussion

Typical temperature and concentration profiles together with the relevant values of hydrodynamic and physicochemical parameters along the column are shown in *Table 3*.

Table 3.

Profiles of temperature, concentration and hydrodynamic parameters along the column height  
 ( $P=1.031$  bar;  $h_w=0.025$  m;  $h_L=0.044$  m;  $h_t=0.100$  m;  $a=291$  m<sup>2</sup>/m<sup>3</sup>)

Plate	No	1	2	3	4	5
$V_{L(1)} \cdot 10^4$	m <sup>3</sup> /s	6.111	6.111	6.117	6.100	6.079
$V_{g(in)} \cdot 10^2$	m <sup>3</sup> /s	7.389	7.687	7.584	7.414	7.260
$y_{n-1}$	%	20.00	18.16	16.46	14.92	13.55
$t_{(1)}$	°C	40.0	40.7	38.7	36.4	34.3
$c_{BO(1)}$	kmol/m <sup>3</sup>	2.400	2.576	2.745	2.897	3.031
$c_{DO(1)}$	kmol/m <sup>3</sup>	1.000	0.912	0.827	0.751	0.684
$k_g a$	kmol/m <sup>3</sup> s bar	0.2613	0.2716	0.2654	0.2567	0.2490
$k_L a$	s <sup>-1</sup>	0.1047	0.1088	0.1038	0.0977	0.0924
$D_{A(1)} \cdot 10^{10}$	m <sup>2</sup> /s	8.967	9.297	8.610	7.844	7.197
$H_{(1)} \cdot 10^3$	kmol/m <sup>3</sup> bar	6.229	6.134	6.406	6.750	7.087
$D_E \cdot 10^3$	m <sup>2</sup> /s	8.35	8.36	8.38	8.40	8.41
$E_{og(1)}$	%	9.02	9.21	9.14	9.03	8.91
$Pe$	—	1.17	1.17	1.17	1.16	1.16
$\lambda_{(1)}^*$	—	0.798	0.700	0.592	0.503	0.432
$E_{MV}$	%	9.20	9.39	9.32	9.21	0.09
$y_n$	%	18.16	16.46	14.92	13.55	12.32
$V_{L(0)} \cdot 10^4$	m <sup>3</sup> /s	6.111	6.117	6.100	6.079	6.061
$V_{g(out)} \cdot 10^2$	m <sup>3</sup> /s	7.687	7.584	7.414	7.260	7.129
$t_{(0)}$	°C	40.7	38.7	36.4	34.3	32.5
$c_{BO(0)}$	kmol/m <sup>3</sup>	2.576	2.745	2.897	3.031	3.150
$c_{DO(0)}$	kmol/m <sup>3</sup>	0.912	0.827	0.751	0.684	0.625

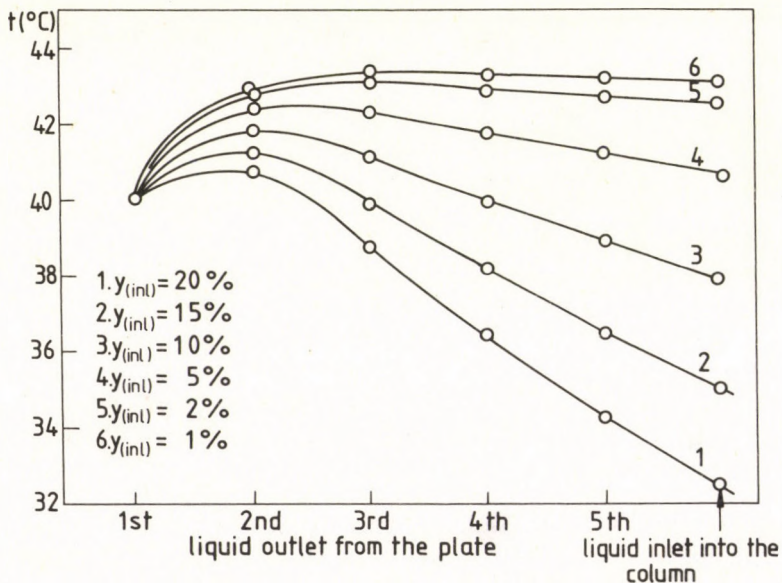


Fig. 2.  
 Temperature profiles along the column.

The temperature profiles along the column are shown in *Fig. 2*. As it is seen from Eq. (13), three heat effects, namely, dissolution and reaction as well as solvent vaporization, have an influence on the total change of liquid temperature. Gas absorption causes an increase of liquid temperature, whereas solvent evaporation – a decrease of liquid temperature. As shown in *Fig. 2* the liquid temperature reaches its maximal value in the middle of the column.

For concentrated gases (10–20% vol.  $\text{CO}_2$ ) an increase of temperature resulting from the absorption dominates the solvent vaporization. For diluted gases (1–5% vol.  $\text{CO}_2$ ) the heat effects of solvent vaporization predominate.

For diluted gases the change of liquid temperature along the column, results only from the heat effects of dissolution and reaction (gas being saturated by  $\text{H}_2\text{O}$  before entering the first plate) being small and amounting to 0.4 °C (1% vol.  $\text{CO}_2$  in a gas phase) and 2 °C (5% vol.  $\text{CO}_2$  in a gas phase).

The changes in the gas phase flow along the column range from 4% (20% vol.  $\text{CO}_2$ ) to 7% (1% vol.  $\text{CO}_2$ ). The changes in the liquid phase flow were less than 1%.

The calculations were also carried out for the case of a low concentration of NaOH solution (1N).

The results of the calculations were compared with experimental data for diluted gases (1% vol.  $\text{CO}_2$ ). The gas was saturated by  $\text{H}_2\text{O}$  before entering the

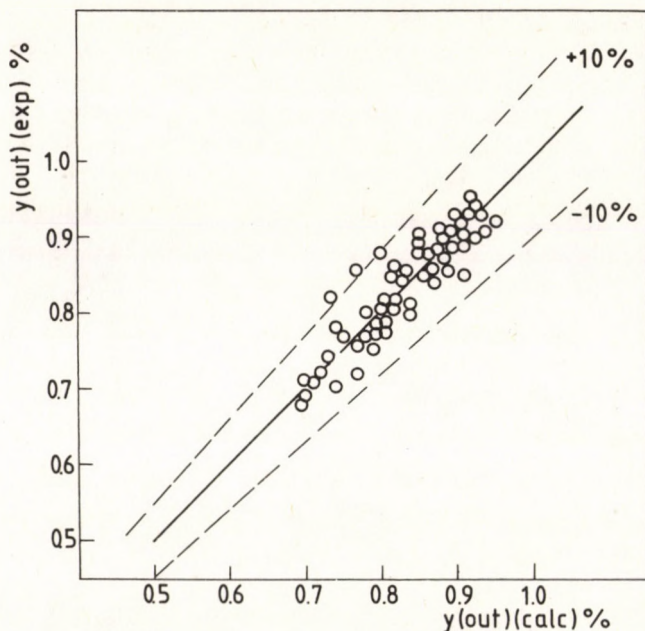


*Fig. 3.*

Comparison of the experimental values of the  $\text{CO}_2$  mole fraction at the column outlet  $y_{(out)}(exp)$  with those calculated  $y_{(out)}(calc)$

Table 4.

Concentration profiles along the column height

( $P = 1.031$  bar;  $y_{(\text{in})} = 1.02\%$ ;  $t = 18^\circ\text{C}$ ;  $V_g = 7.39 \cdot 10^{-2}$  m<sup>2</sup>/s;  $V_L = 6.11 \cdot 10^{-4}$  m<sup>3</sup>/s;  $h_L = 0.044$  m;  $h_T = 0.100$  m;  $h_W = 0.025$  m;  $a = 291$  m<sup>2</sup>/m<sup>3</sup>)

Plate	No	1	2	3	4	5
$y_{n-1}$	%	1.02	0.95	0.88	0.82	0.76
$c_{\text{BO}(1)}$	kmol/m <sup>3</sup>	0.630	0.637	0.644	0.651	0.657
$c_{\text{DO}(1)}$	kmol/m <sup>3</sup>	0.230	0.226	0.223	0.220	0.217
$k_g a$	kmol/m <sup>3</sup> s bar	0.3240	0.3242	0.3244	0.3246	0.3248
$D_{A(1)} \cdot 10^9$	m <sup>2</sup> /s	1.231	1.233	1.234	1.236	1.237
$H_{(1)} \cdot 10^2$	kmol/m <sup>3</sup> bar	2.878	2.879	2.879	2.879	2.879
$E_{\text{og}(1)}$	%	6.88	6.92	6.96	7.00	7.03
$D_E \cdot 10^3$	m <sup>2</sup> /s	8.35	8.35	8.35	8.35	8.35
$Pe$	—	1.18	1.18	1.18	1.18	1.18
$\lambda_{(1)}^*$	—	0.167	0.153	0.141	0.130	0.119
$E_{\text{MV}}$	%	7.01	7.06	7.10	7.14	7.17
$y_n$	%	0.95	0.88	0.82	0.76	0.71
$y_{\text{out}(exp)}$	%	—	—	—	—	0.71

first plate and constant values of temperature and flows of gas and liquid along the column height could be assumed.

A comparison of the CO<sub>2</sub> mole fraction values at the column outlet found experimentally,  $y_{(\text{out})(exp)}$  with those simulated, and  $y_{(\text{out})(calc)}$  is presented in Fig. 3. The average relative error for all the measurements (with respect to the experimental values) was 2.7% (max. error was 11%).

Typical concentration profiles and the values of physicochemical properties and hydrodynamic parameters along the column height are given in Table 4.

The liquid flow on a plate approaches the ideal mixing liquid flow and the influence of the degree of liquid mixing on the value of plate efficiency was very small (1–4%).

### Comparison of the Nutter-Valve – and Sieve-Plate Columns

In order to compare the performance of the Nutter-valve and sieve plate column, the values of column efficiencies were calculated for the same working conditions.

The values of column efficiencies for a sieve plate column are generally higher than those for a Nutter-valve column. Only for low gas velocities ( $u_g = 0.5$  m/s) the values of column efficiencies are a little higher (~5%) for a column with Nutter-valve plates, as for those conditions the interfacial gas-liquid area on Nutter-valve plates is a little higher than that on sieve plates [3]. In the considered working conditions, the values of column efficiencies for a sieve plate column are on the average 15–20% higher than those for a Nutter-valve plate.

In addition, the Nutter-valve plates have a more complicated design and are more expensive.

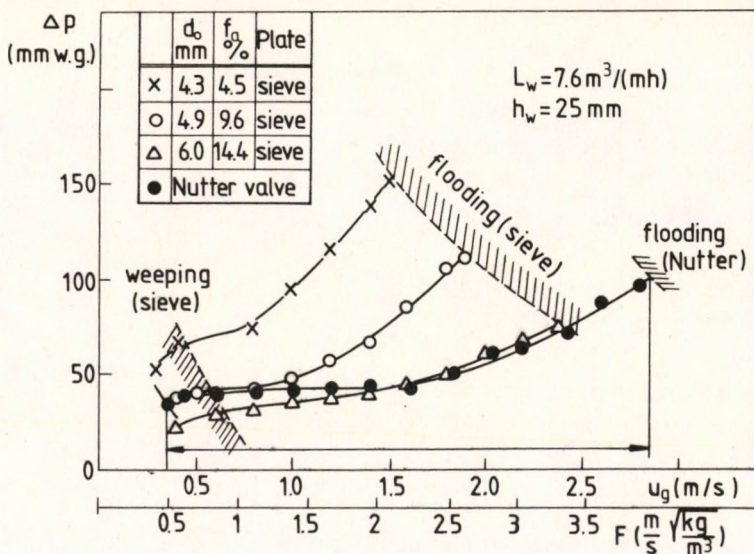


Fig. 4.

Dependence of the total pressure drop across the plate on the gas velocity.

The superiority of the valve plates lies in their hydrodynamic parameters. The results of hydrodynamic measurements are as follows:

1. The pressure drop is smaller on the Nutter-valve plate, hence it is energetically more favourable than the sieve plate.

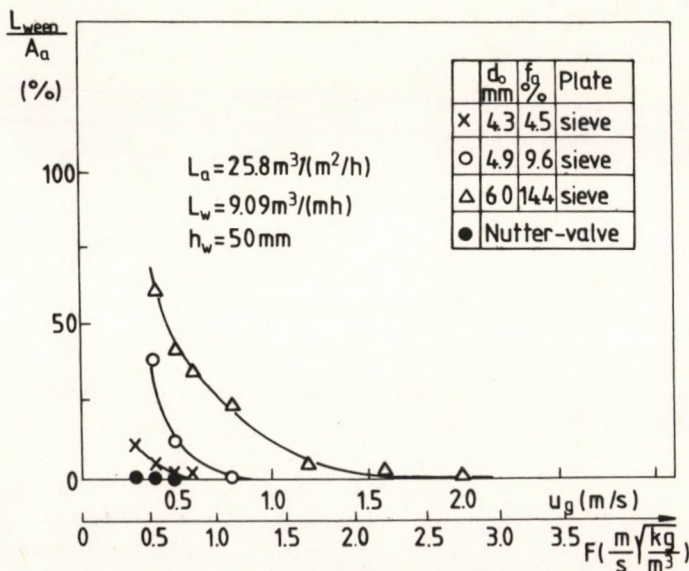


Fig. 5.

Dependence of the liquid weeping on the gas velocity.

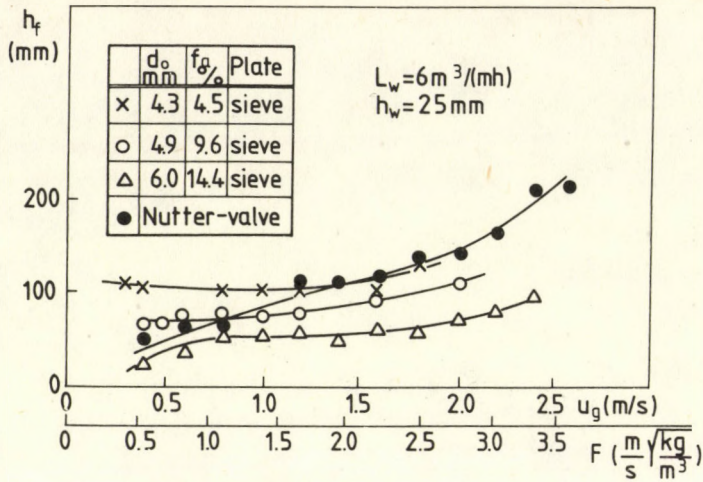


Fig. 6.

Dependence of the froth height on the gas velocity.

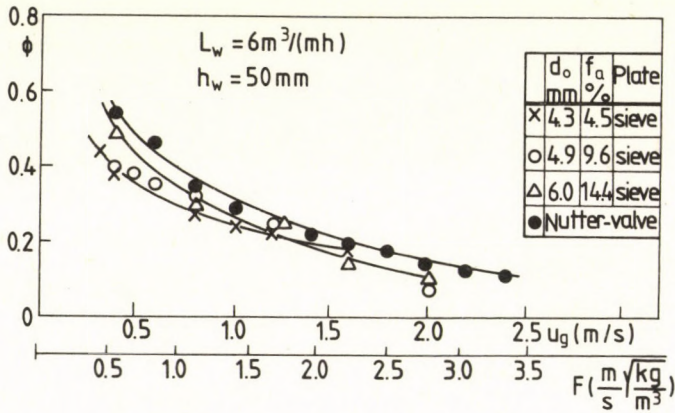


Fig. 7.

Dependence of the relative froth density on the gas velocity.

The pressure drop on the valve plate barely changes with increasing gas velocity (see Fig. 4). This is because the valves open gradually, thus the plate operates more flexibly.

- The operating range of the valve plate is much larger than that of the sieve plate (see Fig. 4). Flooding on the valve plate occurs at an essentially higher gas velocity.

The relationship between the maximum and minimum velocities on the trays is as follows:

$$\left(\frac{F_{\max}}{F_{\min}}\right)_{\text{valve}} = 8-10; \quad \left(\frac{F_{\max}}{F_{\min}}\right)_{\text{sieve}} = 4-5$$

3. There is practically no weeping on the valve plate, whereas the weeping on the sieve plate at small gas velocities is not negligible (see *Fig. 5*). This decreases the efficiency of the plate.
4. The liquid hold-up, the froth height and the relative froth density on the valve and sieve plates are practically the same (see *Fig. 6-7*).

Conclusion: Hydrodynamically, the Nutter-valve plate is much more favourable than the sieve plate.

The same advantages were emphasized by ANDERSON et al. [11].

#### SYMBOLS

$a$	interfacial area unit volume of froth ( $\text{m}^2/\text{m}^3$ )
$A$	plate area ( $\text{m}^2$ )
$b$	stoichiometric coefficient
$c_{\text{BO}}$	concentration of the liquid phase reactant ( $\text{kmol}/\text{m}^3$ )
$c_{\text{DO}}$	concentration of the liquid phase product ( $\text{kmol}/\text{m}^3$ )
$c_p$	specific heat of the solution ( $\text{kJ}/\text{kg} \cdot \text{K}$ )
$d_0$	hole diameter (mm)
$D_A$	diffusivity of the absorbed gas in the liquid phase ( $\text{m}^2/\text{s}$ )
$D_E$	axial dispersion coefficient ( $\text{m}^2/\text{s}$ )
$D_g$	diffusivity of the absorbed gas in the gas phase ( $\text{m}^2/\text{s}$ )
$E_{0g}$	point efficiency
$E_{\text{MV}}$	Murphree plate efficiency
$f$	plate free area referred to the total area of plate (%)
$f_a$	plate free area referred to the active area of plate (%)
$F$	gas velocity factor, defined by Eq. (11) ( $\text{m}/\text{s} \cdot \sqrt{\text{kg}/\text{m}^3}$ )
$g$	valve weight (g)
$G_M$	molar gas flow rate per unit plate area ( $\text{kmol}/\text{m}^2 \cdot \text{s}$ )
$G'_M$	molar gas flow rate ( $\text{kmol}/\text{s}$ )
$h_f$	froth height (m)
$h_L$	clear liquid height (m)
$h_w$	weir height (m)
$H$	Henry's constant ( $\text{kmol}/\text{m}^3 \cdot \text{bar}$ )
$k_{g,a}$	volumetric gas-film mass transfer coefficient per unit volume of froth ( $\text{kmol}/\text{m}^3 \cdot \text{s} \cdot \text{bar}$ )
$k_{L,a}$	volumetric liquid-film mass transfer coefficient per unit volume of froth ( $\text{s}^{-1}$ )
$l$	length of liquid path along the tray (m)
$L_a$	liquid flow rate per unit active area of plate ( $\text{m}^3/\text{m}^2 \cdot \text{h}$ )
$L_w$	liquid flow rate per unit weir height ( $\text{m}^3/\text{m} \cdot \text{h}$ )
$L_{\text{weep}}$	liquid weeping rate per unit active area of plate ( $\text{m}^3/\text{m}^2 \cdot \text{h}$ )
$n$	number of plate
$N$	molar flux ( $\text{kmol}/\text{s}$ )
$N_g$	number of gas-phase transfer units (Eq. 5)
$N_{L(1)}^*$	number of liquid-phase transfer units for the process of absorption with chemical reaction (Eq. 6)
$p$	partial pressure (Tr, bar)
$\Delta p$	total pressure drop across the plate (mm w.g.)
$p_r$	equilibrium pressure of water vapour (bar)

$P$	total pressure (bar, N/m <sup>2</sup> )
$Pe = u_L l / D_E$	Peclet number
$q$	total heat effect of absorption and reaction (kJ/kmol)
$q_A$	heat of absorption (kJ/kmol)
$q_R$	heat of reaction (kJ/kmol)
$q_w$	heat of vaporization of water (kJ/kmol)
$S$	cross-section area of froth (m <sup>2</sup> )
$T$	absolute temperature (K)
$u$	linear velocity (m/s)
$V$	volumetric flow rate (m <sup>3</sup> /s)
$y$	mole fraction of the component A in the gas phase
$y_{n-1}$	mole fraction of the component A in the inlet gas
$y_n$	mole fraction of the component A in the outlet gas
$y^*$	equilibrium mole fraction of the component A in the gas phase
$y^{(in)}$	mole fraction of CO <sub>2</sub> at the column inlet
$y^{(out)}$	mole fraction of CO <sub>2</sub> at the column outlet
$z$	plate width (m)

## GREEK SYMBOLS

$\varepsilon$	porosity of froth
$\Phi$	relative front density $\left( \Phi = \frac{h_L}{h_f} \right)$
$\lambda_{(1)}^*$	parameter defined by Eq. (8)
$\mu$	viscosity (mPas)

## SUBSCRIPTS

g	gas
L	liquid
o	bulk liquid
(0)	liquid inlet
(1)	liquid outlet
(in)	column inlet
(max)	maximum
(min)	minimum
(out)	column outlet

## REFERENCES

1. POHORECKI, R. and MONIUK, W.: *Chem. Eng. J.*, 1989; 38 (1); 27–35.
2. MONIUK, W., MRS. BÉKÁSSY-MOLNÁR, E., MUSTAFA, H. and POHORECKI, R.: *Hung. J. Ind. Chem.* 1989, 17, 93–105
3. MUSTAFA, H.: *Hydrodynamics and Mass Transfer on Sieve Plates and Mutter Valve Plates*, Ph. D. Thesis, Technical University of Budapest, Budapest, 1988 (in Hungarian).
4. POHORECKI, R. and MONIUK, W.: *Chem. Eng. Sci.*, 1988; 43 (7); 1677–1684.
5. POHORECKI, R. and MONIUK, W.: *Chem. Eng. J.*, 1988; 39 (1); 37–46.
6. KUŹNIAR, J., KUBISA R. and PAŠKO, Z.: *Efficiency of Industrial Distillation Plate*, Papers of 9th National Scientific Conference of Chemical and Process Engineering, Part I, p.p. 110–117, Warsaw, 13–16. 09. 1977 (in Polish).
7. POHORECKI, R. and MONIUK, W.: *Investigations of the Kinetics of Natrium Formate Synthesis*, Research Report, Institute of Chemical Engineering, Warsaw Technical University, Warsaw, 1983 (in Polish).

8. BARETT, P. V. L.: Gas Absorption on a Sieve Plate, Ph. D. Thesis, University of Cambridge, Cambridge, 1966.
9. POHORECKI, R., MONIUK, W., KRUSZEWSKI, J. and KONARSKI, W.: Kinetic Model of the Absorption-Desorption in the Benfield Process, Research Report, Institute of Chemical and Process Engineering, Warsaw Technical University, Warsaw, 1988 (in Polish).
10. PERRY, J. H.: Chemical Engineer's Handbook, IV Ed., McGraw-Hill Book Co., New York, 1963.
11. ANDERSON, R. H., GARRETT, G. and VAN WINKLE, M.: Ind. Eng. Chem. Process Des. Dev., 1976; 15 (1) 96-100.



## A STUDY OF KETO-ENOL TAUTOMERISM IN METHYL-ETHYL-KETONE + CARBON TETRACHLORIDE MIXTURES, USING LINEAR AND NON-LINEAR DIELECTRIC METHODS

I. SZALAI and F. RATKOVICS

(Department of Physical Chemistry Veszprém University of Chemical Engineering  
P.O. Box 158. Veszprém H-8201 Hungary)

Received: October 23, 1989

The static relative permittivity  $\varepsilon(0)$ , Piekara factor  $\lambda$ , density  $\rho$ , refractive index referred to the sodium D-line  $n_D$ , and vapour-liquid equilibrium data of a methyl-ethyl-ketone + carbon tetrachloride mixtures were determined at different temperatures.

The results obtained for a mixture of methyl-ethyl-ketone + carbon tetrachloride lend support to the idea that the equilibrium of keto-enol tautomerism is displaced by the non-polar carbon tetrachloride towards the enol formation, i.e. in the direction of the formation of keto-enol association complexes. Based on a dielectric model, the dipole moment ( $\mu_{KE} = 0.81 \times 10^{-30}$  Cm) and relative quantity of the resulting association complex were determined. Based on this model, an explanation could be given of the dipole moment of the methyl-ethyl-ketone molecule measured in a non-polar solvent at infinite dilution.

The equilibrium constant calculated on the basis of the dielectric model ( $K_1 = 0.13$ ) agrees well with the result based on a different model, obtained earlier (RATKOVICS and co-workers [1]).

### Introduction

In the methyl-ethyl-ketone its free enol content is negligible [2]. The enol molecules are linked to a keto molecule being stabilized by an inter-molecular hydrogen bridge, forming a keto-enol associate. If it is mixed with a non-polar component, the keto-enol equilibrium is displaced in the direction of the formation of associates (RATKOVICS and PALÁGYI-FÉNYES [3]). The joining use of the classical dielectric and non-linear dielectric methods is one of the likely methods for studying this equilibrium process. The former one yields the static relative permittivity of the liquid phase  $\varepsilon(0)$ , and the latter the Piekara factor  $\lambda = \Delta\varepsilon/\bar{E}^2$ , a characteristic of the dependence of the static relative permittivity on the

electric field  $\bar{E}$ . Supposing a formation of an association complex, i.e. a dimer, we encounter two unknowns in the study of the equilibrium, the concentration of the associate and its dipole moment. In this study, these quantities and the equilibrium constant of association was determined on the basis of an association model, from the dielectric properties of the methyl-ethyl-ketone + carbon tetrachloride systems.

### Experimental

The chemicals used were Reanal products. The dehydration of carbon tetrachloride and diethyl-ether was made by phosphor pentoxide, that of methyl-ethyl-ketone by sodium sulphate. They were then rectified on a column corresponding to about 15 theoretical plates using a reflux ratio of 1 : 10.

The purity of the materials was checked by density measurements and gas chromatography. Neither water nor any other impurity could be detected.

### Measurement Methods

Density was measured with a digital density meter (Anton-Paar system). Refractive index was determined with a Zeiss Abbé-type refractometer. The vapour-liquid equilibrium measurements were made with a circulation apparatus made according to the description of STAGE [4]. The static relative permittivity was measured with a Siemens impedance bridge (Model Rel 3R-277 A). The Piekara factor of pure materials and mixtures was measured with an apparatus made at our department, based on the principles known in published literature (MAŁECKI [5]).

The experimental arrangement used here was described previously [6].

The Piekara factor was calculated according to the:

$$\lambda = \frac{\Delta\epsilon}{\bar{E}^2} \quad (1)$$

relationship, where  $\Delta\epsilon$  is the change of the permittivity in the high electric field  $\bar{E}$ .

Table 1.

Non-linear effects of liquids

Liquid	$\lambda/(10^{-19} \text{ V}^{-2} \text{ m}^2)$	
	This work	Other sources
carbon tetrachloride	1.50	1.61 [11]
diethyl ether	-35.0	-34.7 [12]
nitrobenzene	31.7	31.5 [13]

### Experimental Results

Table 1 includes the Piekara factors of pure materials measured in our apparatus, compared with data found in literature. The agreement is good, proving the proper functioning of the apparatus. The densities  $\rho$ , refractive indices  $n_D$ , static relative permittivities  $\epsilon(0)$ , Piekara factors  $\lambda$ , and vapour-liquid equilibrium data measured in methyl-ethyl-ketone + carbon tetrachloride systems are presented in Tables 2-5. Due to the rather high specific conductance of the mixture, the Piekara factor could not be measured in the  $0.6 < x_1$  interval of molar fractions.

### The Model Used

The basic ideas were the following:

- i. Three real species are distinguished in mixtures of methyl-ethyl-ketone + carbon tetrachloride. K is ketone in keto form, KE is the keto-enol association

Table 2.

Density of the methyl-ethyl-ketone (1) + carbon tetrachloride (2) mixtures at 293.15 K and 313.15 K.

$x_1$ (mol/mol)	$\rho$ (kg/m <sup>3</sup> )	
	T = 293.15 K	T = 313.15 K
0.0000	1594.1	1554.9
0.0863	1531.8	1493.9
0.1930	1451.8	1415.2
0.2920	1377.4	1342.2
0.3944	1299.0	1265.7
0.4903	1224.4	1192.7
0.6010	1136.7	1107.1
0.6959	1059.5	1031.9
0.8034	971.2	945.6
0.8920	896.8	873.3
1.0000	805.0	783.9

Table 3.

The static relative permittivity ( $\epsilon(0)$ ) of the methyl-ethyl-ketone (1) + carbon tetrachloride (2) mixtures at 293.15 K and 313.15 K.

$x_1$ (mol/mol)	$\epsilon(0)$	
	T = 293.15 K	T = 313.15 K
0.0000	2.23	2.20
0.0863	3.15	2.99
0.1930	4.43	4.15
0.2920	5.77	5.33
0.3944	7.27	6.67
0.4903	8.79	8.01
0.6010	10.65	9.68
0.6959	12.33	11.17
0.8034	14.37	12.99
0.8920	16.20	14.62
1.0000	18.51	16.56

Table 4.

The Piekara constant ( $\lambda$ ) and the refractive index ( $n_D$ ) of the methyl-ethyl-ketone (1)+carbon tetrachloride (2) mixtures at 293.15 K and 313.15 K.

$x_1$ (mol/mol)	$\lambda_{273.15K}$ ( $10^{19} V^{-2} m^{-2}$ )	$x_1$ (mol/mol)	$n_D$	
			T=293.15 K	T=313.15 K
0.000	1.5	0.0000	1.4605	1.4484
0.112	- 45.1	0.0863	1.4542	1.4422
0.191	- 126	0.1930	1.4462	1.4342
0.287	- 212	0.2920	1.4388	1.4269
0.352	- 278	0.3944	1.4308	1.4189
0.402	- 368	0.4903	1.4230	1.4115
0.556	- 561	0.6010	1.4137	1.4023
0.593	- 740	0.6959	1.4060	1.3946
		0.8034	1.3967	1.3855
		0.8920	1.3889	1.3780
		1.0000	1.3792	1.3689

Table 5.

Vapour-liquid equilibrium data the methyl-ethyl-ketone (1)+carbon tetrachloride (2) mixtures at 313.15 K

$x_1$ (mol/mol)	$y_1$ (mol/mol)	$P$ (kPa)	$\ln f_1$	$\ln f_2$
0.000	0.000	28.49	0.750	0.000
0.090	0.125	29.95	0.558	0.010
0.187	0.210	30.59	0.366	0.042
0.227	0.237	30.62	0.294	0.058
0.300	0.293	30.67	0.229	0.083
0.375	0.343	30.43	0.156	0.115
0.523	0.455	29.76	0.084	0.176
0.685	0.595	28.29	0.031	0.244
0.773	0.695	27.15	0.025	0.247
0.840	0.765	26.24	0.004	0.302
0.898	0.852	25.24	0.005	0.251
1.000	1.000	23.80	0.000	0.375

complex, and A is the non-polar constituent. It is supposed that the enol-form itself is not sufficiently stable, and consequently it can be considered absent from the mixture.

ii. The association reaction:



The equilibrium constant of the reaction:

$$K_1 = \frac{x_{KE}}{x_K^2} \cdot \frac{f_{KE}}{f_K^2} = K_{1x} \cdot K_{1f} \quad (3)$$

where  $x_{KE}$  is the real mole fraction of the keto-enol associate,  $x_K$  that of the keto-form,  $f_{KE}$  and  $f_K$  are the corresponding activity coefficients.  $K_{1x}$  is the equilibrium constant including real mole fractions, while  $K_{1f}$  is that involving activity coefficients.

- iii. The dielectric properties of the mixture can be discussed according to the Onsager theory of dielectrics.
- iv. As in a pure methyl-ethyl-ketone the quantity of associates containing the enol-form is negligible, and there is practically no free enol-form, there is no chemical interaction between the molecules in the keto-form, it may be supposed that the  $R_p$  correlation coefficient characteristic for the intensity of the interaction (see relationship (8)) is unity in the pure ketone. Based on the  $R_p = 1$  condition, the dipole moment calculated from relationship (9) can evidently be considered the dipole moment of the keto form.

It is well known that the relationship between the static relative permittivity and the electric field is given by the following equation:

$$\varepsilon(\bar{E}) = \varepsilon(\bar{0}) + \lambda \bar{E}^2 \quad (4)$$

It is a property of the vector of electric polarization that:

$$\bar{P}(-\bar{E}) = -\bar{P}(\bar{E}) \quad (5)$$

so that in (4) no uneven exponent in  $\bar{E}$  can occur. The method of calculating the Piekara factor (1) follows directly from relationship (4).

A consideration of the non-linear dielectric effect in the theory of dielectrics is possible [7] as follows. Neglecting the interaction between dipoles, the average value of the dipole moments in the direction of the field is:

$$\langle \mu^E \rangle = \mu L \left( \frac{\mu F}{kT} \right)$$

where:

$\mu$  molecular dipole moment

$k$  Boltzmann constant

$F$  part of the internal field exerting a directing effect

$T$  temperature

$L(x) = \text{cth } x - \frac{1}{x}$ : Langevin-function

In the region of small fields (linear behaviour), in taking the series expansion in (6) it is sufficient to retain the first member of the series. If, however,  $10^5 \text{ V/m} < F$ , then the second member of the series also gives a considerable contribution to the value of  $\langle \mu^E \rangle$ . Then we get:

$$\langle \mu^E \rangle = \frac{\mu^2}{3kT} F - \frac{\mu^4}{45k^3 T^3} F^3 \quad (7)$$

The contribution of the new member to  $\langle \mu^E \rangle$  is negative, this is called the normal saturation effect.

The interaction of dipoles can be taken into consideration in (7) by the correlation coefficients  $R_p$  and  $R_s$  mentioned earlier.

$$\langle \mu^E \rangle = \frac{\mu^2}{3kT} R_p F - \frac{\mu^4}{45k^3 T^3} R_s F^3 \quad (8)$$

The phenomenological Onsager theory yields the following relationships for  $R_p$  and  $R_s$  correlation coefficients:

$$R_p = \frac{27\epsilon_0 k T (2\epsilon(0) + n_2^2)^2}{N_A \mu^2 x_1 (2\epsilon(0) + 1) (n_2^2 + 2)^2} \left\{ \frac{(M_1 x_1 + M_2 x_2) (\epsilon(0) - 1)}{3Q\epsilon(0)} - \frac{M_1 x_1 (n_1^2 - 1)}{Q_1 (2\epsilon(0) + n_1^2)} - \frac{M_2 x_2 (n_2^2 - 1)}{Q_2 (2\epsilon(0) + n_2^2)} \right\} \quad (9)$$

$$R_s = \frac{45\epsilon_0 k^3 T^3 (2\epsilon(0) + n^2)^2}{N_A \mu^4 x_1 \epsilon(0)^2 (n^2 + 2)^2} \left\{ \frac{(2\epsilon(0) + n^4) (M_1 x_1 + M_2 x_2)}{\epsilon(0)^2 (n^2 + 2)^2 Q} \lambda - \frac{(2\epsilon(0)_2^2 + n_2^4) M_2 x_2}{\epsilon(0)_2^2 (n_2^2 + 2)^2 Q_2} \cdot \lambda_2 \right\} \quad (10)$$

where:

- $x_i$  mole fraction of substance  $i$
- $\epsilon_0$  static permittivity of vacuum
- $N_A$  the Avogadro number
- $M_i$  molar mass of component  $i$
- $\mu$  dipole moment of the polar component.

Index 1 refers to the polar component, index 2 to the non-polar one, the quantities bearing no index refer to the mixture.

Let us introduce the following notations.

- $N$  number all the ketone molecules
- $N_K$  number of molecules in the keto-form
- $N_{KE}$  number of associated keto-enol molecules
- $\mu_{KE}$  dipole moment of the associate
- $\mu_K$  dipole moment of the keto-form

It is evident that:

$$N = N_K + 2N_{KE} \quad (11)$$

In studying the effect of the electric field on chemical equilibria, MAŁECKI [8] expressed the  $R_p$  and  $R_s$  correlation coefficients with molecular characteristics too. Applying his theory to reaction (2) the following relationships were obtained:

$$R_p = z_K + \frac{z_{KE} \mu_{KE}^2}{2\mu_K^2} \quad (12)$$

$$R_s = \frac{1}{\mu_K^4} \left\{ z_K \mu_K^2 \left( \mu_K^2 - \frac{5}{2} \frac{z_{KE} (\mu_{KE}^2 - 2\mu_K^2)}{1 + z_{KE}} \right) + \frac{z_{KE}}{2} \mu_{KE}^2 \left( \mu_{KE}^2 - \frac{5}{2} \frac{z_K (\mu_{KE}^2 - 2\mu_K^2)}{1 + z_{KE}} \right) \right\}$$

Where:

$$z_K = \frac{N_K}{N_K + 2N_{KE}} \quad (13)$$

$$z_{KE} = \frac{2N_{KE}}{N_K + 2N_{KE}} \quad (14)$$

From these, the following equations are obtained for the unknowns  $z_{KE}$  and  $\mu_{KE}$

$$z_{KE}^3 + (4R_p - R_s - 2)z_{KE}^2 + (7R_p^2 - R_s - 10R_p + 4)z_{KE} + 6R_p - 3R_p^2 - 3 = 0 \quad (15)$$

$$\mu_{KE}^2 = \frac{2\mu_K^2(R_p - 1 + z_{KE})}{z_{KE}} \quad (16)$$

Equations (15) and (16) were solved by the Newton-Raphson method, after  $R_p$  and  $R_s$  were calculated from (9) and (10). A transition from the  $z_K$  and  $z_{KE}$  fractions to the molar ratios  $x_K$  and  $x_{KE}$  of a three component mixture is possible by the following relationships.

$$x_K = z_K \left( z_K + \frac{z_{KE}}{2} + \frac{1-x_1}{x_1} \right) - 1 \quad (17)$$

$$x_{KE} = z_{KE} \left( z_K + \frac{z_{KE}}{2} + \frac{1-x_1}{x_1} \right) - 1$$

### Evaluation of the Results

Fig. 1 presents the dependence of the  $R_p$  and  $R_s$  correlation coefficients on the nominal ketone mole fraction. The course of  $R_p$  indicates an associate of small dipole moment, the interaction is decreased on increasing the temperature. In the studied interval of molar ratios  $0 < R_s$ , i.e. a normal saturation effect was found. For the dipole moment of the keto-form  $\mu_K = 10.4 \times 10^{-30}$  Cm (3.14 D) was found at both temperatures.

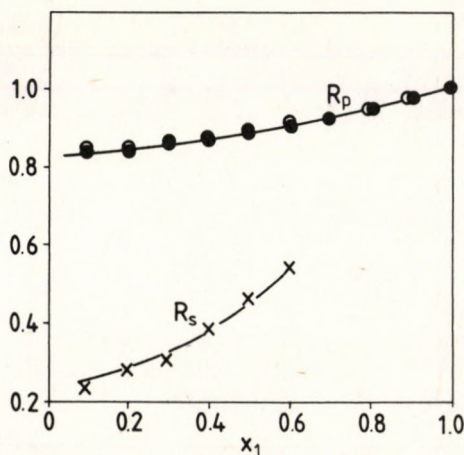


Fig. 1.

The  $R_p$  and  $R_s$  correlation coefficients in the function of the nominal ketone molar fraction at 293.15 K

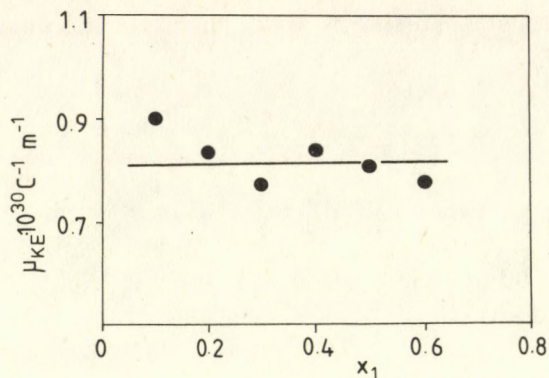


Fig. 2.

Dipole moment of the KE association complex

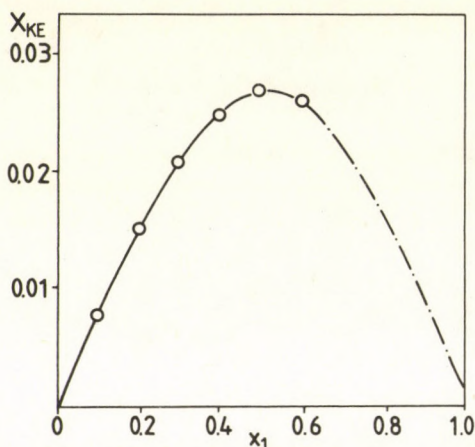


Fig. 3.

The molar fraction of the association at 293.15 K

The dependence of the dipole moment of the KE associate on the ketone mole fraction is seen in Fig. 2.

As  $\mu_{KE}$  can be considered – with a good approximation – constant, this supports our idea that the methyl-ethyl-ketone + carbon tetrachloride mixture can be considered a three component one. We found that  $\mu_{KE}$  is by one order of magnitude smaller than the dipole moment of polar molecules, i.e. the KE association complex has a non-polar character ( $\mu_{KE} = 0.81 \times 10^{-30}$  Cm (0.25 D)). A dependence of the KE associate on the nominal ketone mole fraction is shown in Fig. 3.

It is evident on the Figure that the mole fraction of the KE associate has a maximum in the vicinity of  $x_1 = 0.5$  nominal mole fraction. The agreement with the result obtained by RATKOVICS and co-workers [1] concerning mixtures of methyl-ethyl-ketone + n-heptane and methyl-ethyl-ketone + c-hexane is good in

order of magnitude. As expected from the paper of RATKOVICS and PALÁGYI-FÉNYES [3], reaction (2) is displaced by carbon tetrachloride toward the formation of KE associates. Based on our results, the dipole moment of the methyl-ethyl-ketone molecule in a non-polar solvent at infinite dilution can be explained as follows:

Our model gives for infinite dilution:

$$z_{KE}^{\infty} = \lim_{x_1 \rightarrow 0} z_{KE} = 0.16$$

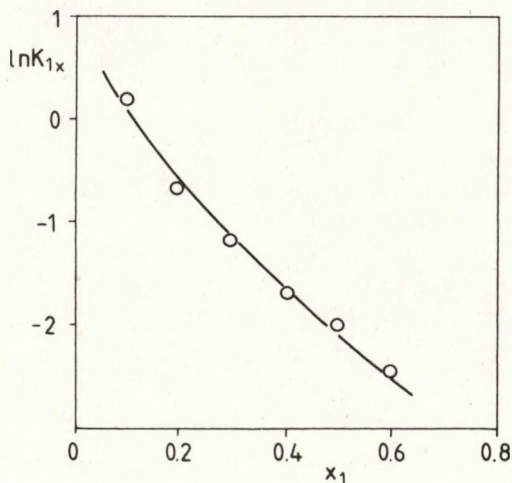


Fig. 4.

The  $K_{1x}$  equilibrium constant in the function of the nominal ketone molar fraction at 293.15 K

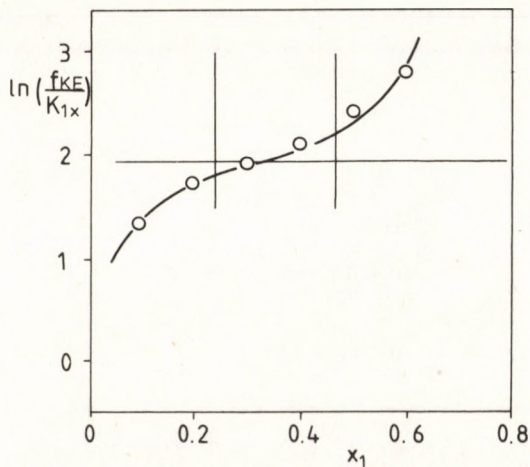


Fig. 5.

The dependence of  $\ln f_{KE} - \ln K_{1x}$  on the nominal ketone molar fraction at 293.15 K

Consequently, at infinite dilution, using the additivity of directional polarization, the dipole moment of the methyl-ethyl-ketone molecule can be calculated from the:

$$\mu_{\text{MEK}}^2 = x_{\text{K}}\mu_{\text{K}}^2 + x_{\text{KE}}\mu_{\text{KE}}^2$$

relationship.

The result obtained:  $\mu_{\text{MEK}} = 9.57 \times 10^{-30}$  Cm (2.87 D) agrees well with those measured by PINKUS [9] in benzene  $\mu_{\text{MEK}} = 9.53 \times 10^{-30}$  Cm (2.86 D), and by ARONEY [10] in carbon tetrachloride  $\mu_{\text{MEK}} = 9.47 \times 10^{-30}$  Cm (2.84 D).

This reasoning leads us to the conclusion that – contrary to the view widespread in literature – the dipole moment of the methyl-ethyl-ketone molecule measured in non-polar solvent at infinite dilution cannot be ascribed to the pure keto-form.

The dependence of the  $K_{1x}$  equilibrium constant of reaction (2) on the nominal ketone mole fraction is seen in *Fig. 4*.

The fact that  $K_{1x}$  varies with  $x_1$  can be explained by the dependence of activity coefficients on the composition. As in the  $0.1 < x_1 < 0.4$  range of mole fraction  $x_{\text{KE}}$  is smaller than  $x_1$  by an order of magnitude, the activity coefficient of the keto-form can be considered with a good approximation identical with that of the ketone in the nominally binary mixture. Taking the activity coefficients from *Table 4*, based on the results of RATKOVICS and co-workers [1], for the dependence of the  $\ln f_{\text{KE}} - \ln K_1$  function on the nominal keton mole fraction, the results shown in *Fig. 6* were obtained. (In *Table 4* the activity coefficients are given at 313.15 K, but this does not introduce any remarkable error, as such differences in temperature do not affect  $f_{\text{KE}}$  considerably.)

Using the results obtained by RATKOVICS and co-workers [1] that  $f_{\text{KE}} = 1$  in the  $0.1 < x_1 < 0.4$  range,  $\ln K_1 = -2.0$  was obtained. Based on another model, [1] obtained in mixtures of methyl-ethyl-ketone + *c*-hexane and methyl-ethyl-ketone + *n*-heptane  $\ln K_1 = -2.1$ . This agreement is very good, proving that the thermodynamic equilibrium constant of the formation of keto-enol association complexes  $K_1 = 0.13$  regardless of non-polar solvent, and this justifies the applicability of these models.

#### LITERATURE

1. RATKOVICS, F., PALÁGYI-FÉNYES, B. and WILDE, L.: *Magy. Kem. Foly.* 1984, 90, 64.
2. GERO, A.: *J. Org. Chem.* 1955, 20, 1960.
3. RATKOVICS, F. és PALÁGYI-FÉNYES, B.: *Magy. Kem. Foly.* 1983, 89, 269.
4. STAGE, H., MÜLLER, E. and GEMMEHER, L.: *Chem. Z. Chem. App.* 1961, 85, 11.
5. MAŁECKI, J.: *J. C. S. Faraday II.* 1976, 72, 1214.
6. SZALAI, I., LÁSZLÓ-PARRAGI, M. and RATKOVICS, F.: *Monats. Chem.* 1989, 120, 413.
7. BÖTTCHER, C.: *The Theory of Electric Polarisation*. Vol I. Elsevier Scientific Publishing Co. Amsterdam, 1973.
8. MAŁECKI, J.: *J. C. S. Faraday II.* 1976, 72, 104.
9. PINKUS, A. and CUSTORD, H.: *J. Phys. Chem.* 1970, 74, 1042.
10. ARONEY, M., LE FEURE, R. and SINGH, A.: *J. Chem. Soc.* 1965, 564.
11. HELLMANS, D. and MAEYR, J.: *J. C. S. Faraday II.* 1982, 78, 401.
12. BRADLEY, A. and JONES, P.: *Sci. Instrum.* 1974, 7, 449.
13. DUTKIEWICZ, M.: *J. C. S. Faraday II.* 1981, 77, 1301.

## ROBUST CONTROL OF HIGH-ORDER OSCILLATIONS IN CONTINUOUS ISOTHERMAL CRYSTALLISERS

M. CHIDAMBARAM\* and Y. S. N. MALLESWARARAO

(Department of Chemical Engineering  
Indian Institute of Technology, Bombay  
Powai, Bombay-400 076, India)

Received: October 24, 1989

A novel method for the design of a robust nonlinear feedback controller is presented for control of high-order oscillations in continuous isothermal crystallisers. The manipulative variable is the nuclei destruction or seeding and the controlled variable is the number moment. Simulation results show that the control system is robust to modelling errors and to disturbances occurring in the system.

Keywords: Crystalliser, nonlinear control, robustness, oscillatory.

### Introduction

Stability of crystal size distribution (CSD) in continuous crystallisers is not guaranteed, even for steady state material and energy inputs. Long term CSD oscillations (limit cycle behaviour) were observed in industrial ammonium sulphate, ammonium nitrate, and potassium chloride crystallisers [1-4]. RANDOLPH and LARSON [4] showed that for a mixed system mixed product removal (MSMPR) crystalliser with nucleation kinetics of the form,  $\Phi^i$ , a value of  $i$  greater than 21 is required for the CSD to become unstable. Stability analysis pointed out two modes of CSD instabilities: high order cycling, which is caused by discontinuous nucleation phenomena, giving an effective nucleation kinetic order greater than 21 [4, 5], and low-order cycling, which is primarily due to product classification [6, 7].

SAEMAN [8] discussed techniques by which nuclei could be segregated and destroyed as a means to control crystal size distributions. RANDOLPH and

---

\* author to whom correspondence is to be addressed.

LARSON [3] studied dynamic behaviour of continuous, isothermal, mixed suspension, non-classified product crystallisation with respect to step changes in the production rate and in nuclei destruction rate. They discussed control schemes utilizing nuclei destruction based on the measurement of suspension area and nuclei density. SHERWIN et al. [6] analyzed crystal population dynamics based on the work of HULBURT and KATZ [9], and stability in terms of a sensitivity parameter was discussed. These independent works demonstrated that open-loop crystallisation processes may be inherently unstable. HAN [10] described a control scheme based on the manipulation of flow rate. The scheme, however, was not capable of stabilizing inherently high-order oscillatory dynamics.

Stability analysis by LEI et al. [11, 12] showed that high-order cycling in a crystallizer with a fines trap can be eliminated by a proportional control of the flow to the fines trap. They based their control scheme on the measurement of the area density (second moment) in the fines trap.

GUPTA and TIMM [13] proposed a control scheme for stabilizing high-order cycling in MSMPR crystallisers. Their control system initiated fines destruction whenever the number density (as given by the zeroth moment) was above the steady state value and seeded the crystalliser whenever the number density was below the steady state value. Their control system design and simulation results were based on a linearized model for high-order cycling eliminations. A control system design for elimination of low-order cycling was analyzed by BECKMAN and RANDOLPH [14], and ROUSSEAU and HOWELL [15]. A recent review of the work done in dynamics and the control of CSD was given by TRAVARE [16]. In the present work, control for the elimination of high-order cycling is considered. All the methods so far reported in literature for the elimination of high-order cycling do not consider the robustness of the control system to modelling errors and disturbances occurring in the system. Further, all the methods consider only the regulatory problem and do not consider the start-up or servo problem. In the present model, a robust control system design for nonlinear systems reported by BHAT et al. [17] is applied to eliminate high-order oscillations in isothermal continuous crystallizers.

### Model Equations

The dynamics of crystal size distribution (CSD) were presented by various authors in terms of the moments of distribution [3, 6, 10, 13]:

$$\frac{dN}{d\theta} - \phi z^0 + \frac{N}{\tau} = 0 \quad (1)$$

$$\frac{dL}{d\theta} - \phi N + \frac{L}{\tau} = 0 \quad (2)$$

$$\frac{dA}{d\theta} - \phi L + \frac{A}{\tau} = 0 \quad (3)$$

The above variables were made dimensionless concerning the reference steady-state values. As a consequence of the conservation of mass, the growth rate at constant suspension was generated by:

$$\Phi = 1/(\tau A) \quad (4)$$

Nucleation rate was generated by:

$$\Phi z^0 = \Phi^i \quad (5)$$

where  $i$  is the relative kinetic order of crystallisation. With initial steady state values references, the initial conditions are:

$$N(0) = L(0) = A(0) = \tau(0) = 1 \quad (6)$$

The set of nonlinear differential equations with  $i=22$  were solved for a step disturbance in mean residence time at constant suspension density. The open loop response is shown in *Fig. 1*. It is highly oscillatory. The stability analysis on linearized model [4] shows that for  $i=22$  it is unstable (increasing  $N$  with time), whereas the solution of the nonlinear model by the present work shows that for  $i=22$  it is still the sustained oscillatory (limit cycle) in  $N$ . Even for  $i=26$

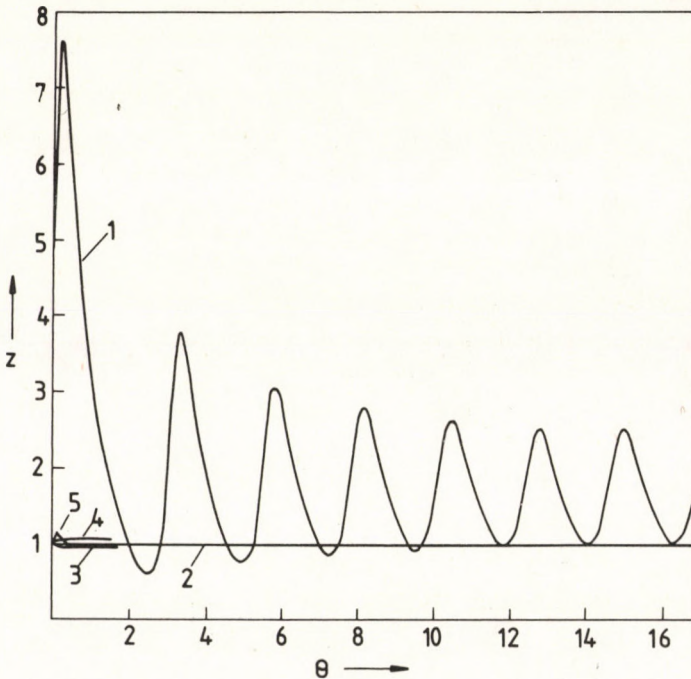


*Fig. 1*

Performance of the control system for regulation.

- 1 - Open-loop system; 2 - Closed-loop using Equation (24); 3 - +40% perturbation in  $\Phi^i$ ; 4 - -40% perturbation in  $\Phi^i$ ; 5 - Closed-loop with Equation (24) and (27) with  $T=0.1$ ;  
 $k = -10.0$ ,  $\lambda_m = -1.0$ ,  $i = 22$

the nonlinear model shows sustained oscillation only. The initial peak value increases steeply as  $i$  increases (not shown in the Figure). For  $i=22$ , the peak value is 7.65 whereas for  $i=30$  it is 17.5. As pointed out by GUPTA and TIMM [13] a disturbance in the mean residence time can result in a surplus or a deficiency of nuclei, assuming the desired product distribution is to remain constant. In the former case, a balance can be achieved through nuclei destruction: in the latter, nuclei have to be added, perhaps by external seeding. The destroyer is assumed to have a negligible time delay. Seeding crystals are of nuclei size and have negligible mass [13]. Hence Equation (1) becomes [13]:

$$\frac{dN}{d\theta} - a\Phi^i + \frac{N}{\tau} = 0 \quad (7)$$

For nuclei destruction  $a < 1$ ; for seeding  $a > 1$ . The feedback loop is shown in Figure 2. Equations (7), (2) and (3) can be rewritten in the standard form as:

$$\dot{x} = f(x) + g(x)u$$

where:

$$f(x) = \begin{bmatrix} -(N/\tau) \\ + (1/(\tau A) - (L/\tau)) \\ 1/(\tau A) - (A/\tau) \end{bmatrix} = \begin{bmatrix} -(x_1/\tau) \\ 1/(\tau x_3) - (x_2/\tau) \\ 1/(\tau x_3) - (x_3/\tau) \end{bmatrix}$$

$$g(x) = \begin{bmatrix} \Phi^i \\ 0 \\ 0 \end{bmatrix} \quad (8)$$

The variable to be controlled is the number moments  $N (= x_1)$ . Thus we have:

$$y = cx \quad (9)$$

where:

$$c = [1 \ 0 \ 0]$$

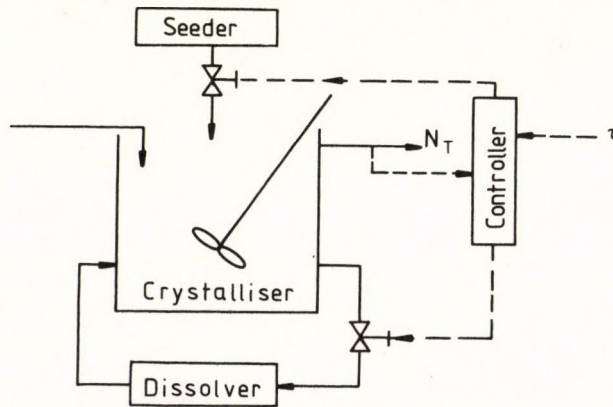


Fig. 2

Schematic sketch of the feedback-feedforward control scheme.

--- Signal- ——— Material flow

Let us now look at the method of designing control schemes for tracking the output to the desired reference value.

### Control System Design

The conventional controller design technique for systems with relatively mild nonlinearities are based on linearization around an operating point and then applying the well established linear control theory to design linear controllers. However, for the regulation of severely nonlinear systems such an approach may yield extremely poor controller performance and the use of a nonlinear control law may be a necessity [18].

Let us briefly discuss the method of BHAT et al. [17] for designing a robust nonlinear feedback controller for trajectory tracking. The system considered is in a state variable form:

$$\dot{x} = f(x) + g(x)u + d(\theta) \quad (10)$$

$$y = cx \quad (11)$$

Here  $x$  is the state vector of size  $n \times 1$  and the vectors  $f(x)$  and  $g(x)$  are the nonlinear function of  $x$ .  $u$  is a scalar manipulative input. The vector  $d(\theta)$  represents in general disturbances and  $y$  is a scalar output and is a linear function of the state variables,  $x$ . Here  $c$  is a constant vector.

Let us assume the reference model in the scalar output  $y$  is given by:

$$\dot{y}_m = \lambda_m y_m + b_m r \quad (12)$$

The scalar  $e$  is defined as the difference between the reference value and the process output:

$$e = y_m - y \quad (13)$$

The control objective is to force the error to vanish with a desired dynamics:

$$\dot{e} = \lambda e \quad (14)$$

where  $\lambda$  is the value for the error system.

Combining Equations (10) to (14), we get:

$$\dot{e} = \dot{y}_m - \dot{y} \quad (15)$$

$$= \lambda_m e + (\lambda_m y + b_m r - cf - cgu - cd) \quad (16)$$

If we make:

$$+ \lambda_m y + b_m r - cf - cgu - cd = ke \quad (17)$$

from which we calculate the control law:

$$u = (cg)^{-1}[b_m r - cf - cd - ke + \lambda_m y] \quad (18)$$

Equation (16) becomes:

$$\begin{aligned}\dot{e} &= (\lambda_m + k)e \\ &= \lambda e\end{aligned}\quad (19)$$

where  $k$  is the scalar error feedback gain.

It is to be noted that Equation (18) is also applicable to a multi-input multi-output system, where the number of the input is equal to the number of the output. In such cases  $c$  and  $g$  are matrices,  $cg$  is a square matrix;  $\lambda_m$  to be replaced by a reference system constant matrix  $A_m$ ;  $b_m r$  to be replaced by  $B_m R_m$  of appropriate sizes in Equation (12).

In Equation (19), the error system eigen value  $\lambda$  can be assigned arbitrarily through proper feedback gain  $k$ . The control law Equation (18) is used to calculate  $u$  in order to get the desired error dynamics.

### Application to Crystallisers

Let us consider the problem of stabilizing the crystalliser at the unstable steady-state when  $i=22$  [ $N=1$ ,  $L=1$ ,  $A=1$ ]. The solution of the reference model Equation (12) with the initial condition  $y_m = x_{1,0}$  at  $\Theta=0$  is given by:

$$y_m(\Theta) = x_{1,0}e^{\lambda_m\Theta} + \left(\frac{-b_m r}{\lambda_m}\right)(1 - e^{\lambda_m\Theta})\quad (20)$$

It is to be noted that  $\lambda_m$  has a negative value and the speed of response of  $y_m$  increases as  $\lambda_m$  increases in the negative direction. The value of  $y_m$  has to reach the steady-state values  $x_1^s$  from whatever may be the initial condition,  $x_{2,0}$ . Thus we have, from Equation (20) under steady-state:

$$-b_m r = x_1^s \lambda_m\quad (21)$$

We have now the reference model as:

$$\dot{y}_m = \lambda_m y_m - \lambda_m x_2^s\quad (22)$$

$$y_m(\Theta=0) = x_{1,0}\quad (23)$$

We will apply the result of an earlier section to design a robust feedback controller. The control law Equation (18) becomes:

$$u = (1/\Phi^i) \left[ b_m r + \frac{y}{\tau} - k(y_m - y) + \lambda_m y \right]\quad (24)$$

Since the knowledge of the disturbance ( $\tau$ ) is required in Equation (24) the control law is essentially a combined feedback-feedforward.

Simulation results of the closed loop system are shown in Figure 1. A perfect regulation is achieved. A similar response is also achieved in  $L$  and  $A$ . The value of the manipulative variable is shown in Figure 3. The robustness of the control system to modelling errors on the performance of the control system is studied

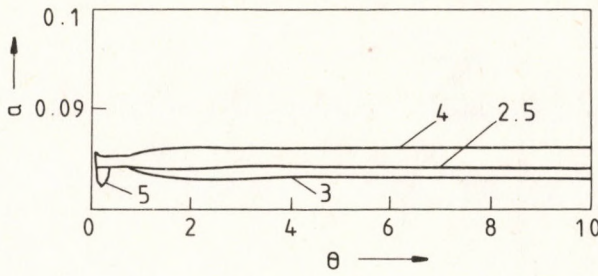


Fig. 3  
Manipulative variable versus time for Figure 1.  
Legend: Same as in Figure 1.

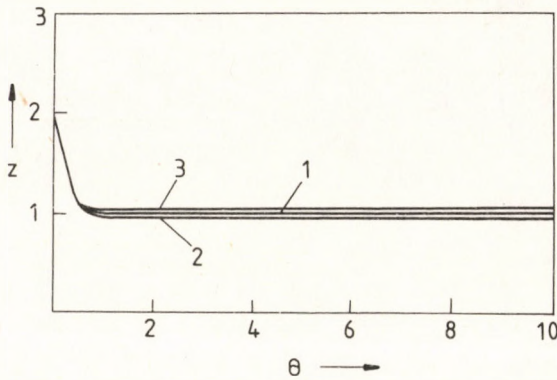


Fig. 4  
Performance of the control system for start-up condition. (at  $\theta=0, N=2.05, L=1.66, A=1.22$ )  
1 - With Equation (24); 2 - +40% perturbation in  $\Phi^i$ ; 3 - -40% perturbation in  $\Phi^i$ ;  
 $k = -10.0, \lambda_m = -1.0$

by giving perturbations +40% and -40% separately in the rate  $\Phi^i$  and the perturbed value is used only in the control law Equation (24). Robustness of the control system is shown in Figure 1.

The performance of the control system for start-up condition is studied by using  $N=2.04, L=1.66, A=1.22$  and  $\tau=0.833$  at  $t=0$  in the crytalliser. The desired values of  $N, L$  and  $A$  are each 1. The performance of the control system is shown in Figure 4. A good response is obtained. The robustness of the control system for perturbation in  $\Phi^i$  of +40% and -40% separately in the control law Equation (24) is studied. A robust response is gained as shown in Figure 4.

To use Equation (24) we require the value of  $\Phi^i$  which depends on the values of  $i, A$  and  $\tau$ . Since the value of  $i$  is greater than 21 for oscillations, even a small error in  $i$  leads to a larger change in  $\Phi^i$ . We can predict  $\Phi^i$  from Equation (7) as follows:

$$\Phi^i(\theta) = (\dot{N}(\theta) + N(\theta)/\tau(\theta))/a(\theta) \tag{25}$$

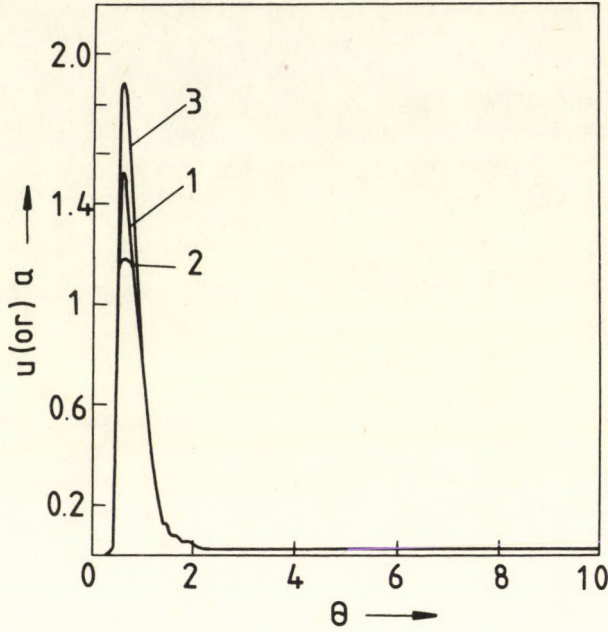


Fig. 5

Manipulative variable versus time for Figure 4. (at  $\Theta=0, a=1$ ). Legend: Same as in Figure 4.

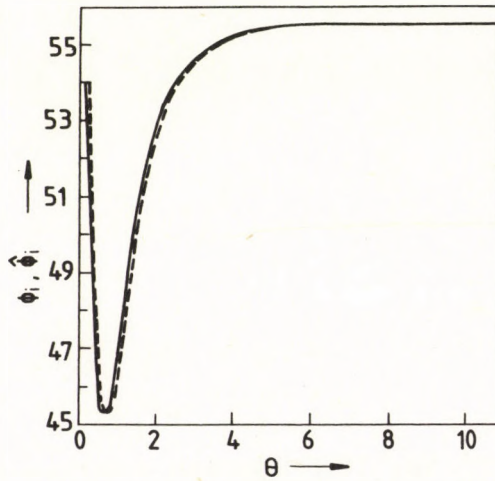


Fig. 6

Predicted and actual dynamics of  $\Phi^i$  ——— actual value of  $\Phi^i$ ; - - - predicted value from Equation (27) with  $T=0.1$  (at  $\Theta=0, \Phi^i=1$ ).

To obtain the estimate of  $\Phi^i$ , it can be assumed that for the small time delay  $T$ , the estimate  $\Phi^i$  at present time  $\Theta$  is close to the value of  $\Phi^i$  at time  $(\Theta - \tau)$  in the past [19]:

$$\Phi^i|_{\Theta} = \Phi^i|_{(\Theta - T)} \quad (26)$$

Using Equation (25) and (26) we can estimate  $\Phi^i$  as:

$$\Phi^i|_{\Theta} = (\dot{N}(\Theta - T) + N(\Theta - T)/\tau(\Theta - T))/a(\Theta - \tau) \quad (27)$$

This predicted value of  $\Phi^i$  is used in the control law Equation (24).

We presume here that the derivative of  $N$  is available from the measurement of  $N$ . Using Equation (27) in Equation (24), we find that the resulting control law does not require the knowledge of the order  $i$  and the measurement on  $A$ . All those required are a measurement of  $N$  and its derivative and the mean residence time. The performance of the control system using Equations (24) and (27) is shown in Figure 1 itself. A robust response is obtained. The actual and the predicted value of  $\Phi^i$  is shown in Figure 5. Since the time derivative of  $N$  is required, the present method of getting  $\dot{N}$  from  $N$  directly is applicable only to the situation where the measurement of  $N$  is not corrupted significantly by noise. For the situation of a significant level of noise presence, we can get the derivative of  $N$  from the measurement of noise corrupted  $N$  by using the differentiating Extended Kalman filter approach suggested by CARLSSON et al. [20].

## Conclusion

The theory and application of a robust nonlinear feedback controller for elimination of oscillations in continuous isothermal crystallisers is presented. The controller is robust to modelling errors and disturbances. The method of BHAT et al. [17] provides a unified frame work for treating nonlinear control problems arising in crystallisers.

## SYMBOLS

$A$	crystalline area moment, dimensionless.
$A_m$	reference system matrix
$a$	factor by which nuclei density changes due to seeding or dissolving
$B_m, b_m$	coefficient matrix or vector of the input in the reference model
$d$	disturbance vector in the nonlinear model
$e$	error, $y_m - y$
$f(x), g(x)$	vector fields characterizing the nonlinear model
$i$	nucleation dependency with respect to growth
$k$	feedback gain
$L$	crystalline length moment, dimensionless
$m$	number of inputs
$n$	order of the state-variable model
$N$	crystalline number moment, dimensionless
$r$	input in the reference model

$t$	time, hr.
$T$	time delay used in the prediction of unknown dynamics
$u$	manipulative input
$x$	state vector
$x_1, x_2, x_3$	elements of $x$ representing respectively $N, L$ and $A$
$x^s$	steady-state value of $x$
$x_{j,0}$	initial value of the $j^{\text{th}}$ state variable
$y$	output variable of the system
$y_m$	reference model output
$z^0$	nuclei population density, dimensionless.

## GREEK SYMBOLS

$\theta$	time, dimensionless
$\tau$	mean residence time, dimensionless
$\phi$	growth rate, dimensionless
$\lambda, \lambda_m$	eigen value of the error system and the reference model respectively.

## LITERATURE

1. SAEMAN, W. C.: *AIChE J.*, 1956, 2, 107.
2. ROBINSON, J. N. and ROBERTS, J. E.: *Can. J. Chem. Eng.*, 1957, 35, 105.
3. RANDOLPH, A. D. and LARSON, M. A.: *Chem. Eng. Prog. Symp. Ser.*, 1965, 61, 147.
4. RANDOLPH, A. D. and LARSON, M. A.: *AIChE J.*, 1962, 8, 639.
5. RANDOLPH, A. D.: *AIChE Symp. Ser.*, 1980, 76, 193.
6. SHERWIN, M. B., SHINNAR, R. and KATZ, S.: *Chem. Eng. Prog. Symp. Ser.*, 1969, 65, 75.
7. RANDOLPH, A. D., BEER, G. L. and KEENER, J. P.: *AIChE J.*, 1973, 19, 1140.
8. SAEMAN, W. E.: *Ind. Eng. Chem.*, 1961, 53, 612.
9. HULBURT, H. M. and KATZ, S.: *Chem. Eng. Sci.*, 1964, 19, 555.
10. HAN, C. D.: *Ind. Eng. Chem. Proc. Des. Dev.*, 1969, 8, 150.
11. LEI, S., SHINNAR, R. and KATZ, S.: *AIChE J.*, 1971, 17, 1459.
12. LEI, S., SHINNAR, R. and KATZ, S.: *Chem. Eng. Prog. Symp. Ser.*, 1971, 67, 129.
13. GUPTA, G. and TIMM, D. C.: *Chem. Eng. Prog. Symp. Ser.*, 1971, 67, 121.
14. BECHMAN, J. R. and RANDLOPH, A. D.: *AIChE J.*, 1977, 23, 510.
15. ROUSSEAU, R. W. and HOWELL, T. R.: *Ind. Eng. Chem. Proc. Des. Dev.*, 1982, 21, 606.
16. TAVARE, N. S.: *AIChE J.*, 1986, 32, 705.
17. BHAT, J., CHIDAMBARAM, M. and MADHAVAN, K. P.: *Chem. Engg. Commun. (1989)* 87, 195.
18. SHINSKEY, F. G.: *Process Control System*, 2nd Ed., McGraw Hill, N. Y., 1979.
19. YOUCEF-TOUMI, K. and ITO, O.: *Ame. Contr. Conf.*, 1987, 836.
20. CARLSSON, B., SODERSTROM, T. and AHLEN, A.: *Digital Differentiating Filters*, Report UPTEC 8792 R, Uppsala Univ., Sweden, 1987.

## ESTIMATION PROCEDURES FOR TWO STOCHASTIC MODELS DESCRIBING PARTITION AND REPLICATION OF PLASMIDS

J. BARANYI\* and T. ILLENI

(Uppsala University Microbiology Department S-75123 Uppsala P.O.Box 581 SWEDEN)

Received: November 1, 1989

A stochastic process describing plasmid replication and partition is introduced. The main advantage of this model is that in the stationary state the plasmids have a Poisson distribution in the plasmid harbouring cells. By means of the explicit results of the model simple estimations are given for some parameters of two other models known from literature.

Keywords: mathematical model, replication, partition, plasmid stability, stochastic process

### Introduction

In the so-called genetically engineered micro-organisms the genetic code for the production of some important proteins is usually located on plasmids. Plasmids can replicate themselves during a cell cycle and their partitioning is a consequence of cell division. These autocatalytic happenings finally lead to a larger production of the target proteins.

Plasmid stability is related to the phenomenon, that at cell divisions, plasmid free (negative) cells can be born, which neglectably rarely revert back to plasmid harbouring (positive) ones. If these negative cells grow at least as fast as the positive cells, they sooner or later outpace the positive variants (the proportion of the positive cells converges to zero).

To study this phenomenon, it is crucial to model the replication and partition of plasmids. The biological mechanism controlling this process is very complex, and so are the mathematical models, which describe it. Therefore, it is desirable

---

\* On leave from:

Technical College for Machinebuilding and Automation Math. Phys. Department  
Izsáki út 10, H-6000 Kecskemét, HUNGARY  
Correspondent author

to give simple estimates for the quantities that can be calculated in a complicated way or by computer simulation only.

A simple basic stochastic process is given as a model, which has some advantageous features:

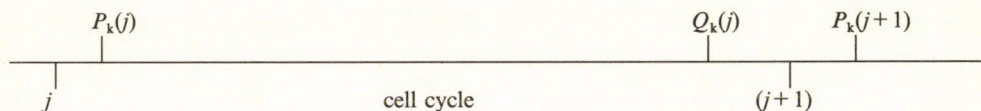
- The model is close to those examined in literature (e.g. [4], [5], [6], [7]).
- In the stationary state of the process, the plasmids have a Poisson distribution in the positive cells. This (or the approximately normal distribution) is frequently assumed in literature (e.g. [5], [7]). In our model, however, this can be proved from the basic assumptions imposed on the replication and partition of the plasmids.
- It is easy to calculate characteristic quantities of the model (e.g. segregation probability, average copy number, and the rate of convergence mentioned above). These expressions can be used as upper or lower boundaries for the correspondent parameters of other models, the stationary state of which is not so easy to calculate.

### Description of an Idealistic Model in the Subpopulation of Plasmid Harboring Cells (Model 1)

In what follows, we refer to plasmid harboring cells as positive, and plasmid free cells as negative variants. First we consider the subpopulation of the positive cells only.

Let the random variables  $X(j)$  and  $Y(j)$  denote the number of plasmids in a positive cell just after the  $j$ -th and just before the  $(j+1)$ -th partitioning, respectively. Define the next (conditional) probabilities:

$$P_k(j) = \text{Prob}(x(j) = k | k \geq 1) \quad Q_k(j) = \text{Prob}(Y(j) = k | k \geq 1) \\ (k = 1, 2, 3, \dots; \quad j = 0, 1, 2, \dots)$$



Let  $\alpha_j(m, n)$  denote the probability that in a cell during the  $j$ -th cell cycle  $m$  replications occur under the condition that the cell contained  $n \geq 1$  plasmids at the beginning of the cell cycle:

$$\alpha_j(m, n) = \text{Prob}(Y(j) - X(j) = m | X(j) = n) \quad (0 \leq m; 1 \leq n; j = 0, 1, 2, \dots)$$

Let  $\beta_j(m, n)$  denote the probability that in a newborn positive cell at the beginning of the  $j$ -th cell cycle, there are  $m$  plasmids under the condition that its mother cell contained  $n$  plasmids before the division:

$$\beta_j(m, n) = \text{Prob}(X(j) = m | Y(j-1) = n) \quad (1 \leq m \leq n; 1 \leq n; j = 1, 2, 3, \dots)$$

The  $X(j)$ ,  $Y(j)$  stochastic process is well defined if for any  $j \geq 0$ ,  $n \geq 1$ :

$$\sum_{m=0}^{\infty} \alpha_1(m, n) = 1 \quad (1.1)$$

$$\sum_{m=1}^n \beta_j(m, n) = 1 \quad (1.2)$$

If the initial distribution of the plasmids,  $P_k(0)$  ( $k = 1, 2, 3, \dots$ ) is given, then the  $P_k(j)$ ,  $Q_k(j)$  ( $k = 1, 2, 3, \dots$ ;  $j = 0, 1, 2, \dots$ ) distributions are uniquely determined by the equations:

$$Q_k(j) = \sum_{i=1}^k P_i(j) \alpha_j(k-i, i) \quad (k = 1, 2, 3, \dots; j = 0, 1, 2, \dots) \quad (1.3)$$

$$P_k(j+1) = \sum_{i=k}^{\infty} Q_i(j) \beta_j(k, i) \quad (k = 1, 2, 3, \dots; j = 0, 1, 2, \dots) \quad (1.4)$$

In our Model 1, we define  $\alpha_j(m, n)$  and  $\beta_j(m, n)$  as generation-independent probabilities:

$$\alpha_j(m, n) = \frac{N^m}{m!} e^{-N} \quad (N > 0 \text{ fixed}; 0 \leq m; 1 \leq n; j = 0, 1, 2, \dots) \quad (1.5)$$

$$\beta_j(m, n) = \left(\frac{1}{2}\right)^{n-1} \binom{n-1}{m-1} \quad (1 \leq m \leq n; 1 \leq n; j = 1, 2, 3, \dots) \quad (1.6)$$

It can be seen that in this model – which is specifically a Markov chain – the number of replications follows the Poisson distribution, with the expected value of  $N$  independently of the actual number of plasmids in the cell. This assumption was used in [5].

Our definition for the partition is not the classical binomial partition, which was assumed in [6] and [7]. There the assumed binomial distribution concerned the positive and negative cells together, while we define this only for positive cells. The possible biological interpretation of this assumption will be discussed later.

It is easy to check that (1.5) and (1.6) satisfy (1.1) and (1.2).

The next theorem shows the stationary state of this Markov chain.

### Theorem 1.1

If

$$P_k(0) = e^{-N} \frac{N^{k-1}}{(k-1)!} \quad (k = 1, 2, 3, \dots) \quad (1.7)$$

then for any  $j \geq 0$ :

$$P_k(j) = e^{-N} \frac{N^{k-1}}{(k-1)!} \quad (k = 1, 2, 3, \dots) \quad (1.8)$$

$$Q_k(j) = e^{-2N} \frac{(2N^{k-1})}{(k-1)!} \quad (k = 1, 2, 3, \dots) \quad (1.9)$$

This theorem is a special case of the one described in [2]. Nevertheless, elementary proof of it is given in the Appendix.

It can be shown – see [1] – that this Markov chain converges to its stationary state, i.e. as  $j \rightarrow \infty$ .

$$P_k(j) \rightarrow P_k = e^{-N} \frac{N^{k-1}}{(k-1)!} \quad (k = 1, 2, 3, \dots) \quad (1.10)$$

$$Q_k(j) \rightarrow Q_k = e^{-2N} \frac{(2N)^{k-1}}{(k-1)!} \quad (k = 1, 2, 3, \dots) \quad (1.11)$$

It can be said that at the  $j$ -th partition, segregation occurs if  $Y(j-1) = n$  and  $X(j) = n$  for some  $n \geq 1$  (i.e. all the plasmids have moved to one of the daughter cells).

*Lemma*

If  $a(j)$  denotes the probability of segregation at the  $j$ -th partition then:

$$a(j) = \sum_{i=1}^{\infty} Q_i(j) \left(\frac{1}{2}\right)^{i-1} \quad (1.12)$$

*Proof*

It is sufficient to see that for any  $n, j \geq 1$ :

$$\text{Prob}(Y(j-1) = n \text{ and } X(j) = n) = Q_n(j) \beta_j(n, n)$$

*Theorem 1.2*

Probability of segregation converges to a positive constant as the process converges to its stationary state, namely:

$$a(j) \rightarrow e^{-N} \quad (j \rightarrow \infty) \quad (1.13)$$

*Proof*

If

$$Q_k(j) \rightarrow e^{-2N} \frac{(2N)^{k-1}}{(k-1)!} \quad (j \rightarrow \infty)$$

then because of the Lemma:

$$a(j) \rightarrow e^{-2N} \sum_{k=1}^{\infty} \frac{(2N)^{k-1}}{(k-1)!} \left(\frac{1}{2}\right)^{k-1} = e^{-2N} \sum_{k=1}^{\infty} \frac{N^{k-1}}{(k-1)!} = e^{-N} \quad (j \rightarrow \infty)$$

### Taking the Negative Cells into Account

Let the probabilities  $p_k(j)$ ,  $q_k(j)$  be introduced just like  $P_k(j)$  and  $Q_k(j)$ , but also taking the plasmid free cells into account:

$$p_k(j) = \text{Prob}(X(j) = k) \quad q_k(j) = \text{Prob}(Y(j) = k) \\ (k = 0, 1, 2, \dots; j = 0, 1, 2, \dots)$$

That is  $p_k(j)$  and  $q_k(j)$  can be interpreted as the proportion of the cells containing exactly  $k$  plasmids ( $k \geq 0$ ) in the joint population of the positive and negative cells.

Suppose that the cell cycle of the negative cells is as long as that of the positive

cells. If  $p_k(0)$  ( $k = 0, 1, 2, \dots$ ) is given, then  $q_k(j)$  and  $p_k(j+1)$  ( $k = 0, 1, 2, \dots$ ;  $j = 0, 1, 2, \dots$ ) can be calculated as:

$$q_k(j) = \begin{cases} p_0(j) & (k=0) \\ Q_k(j)H(j) & (k \geq 1) \end{cases} \quad (2.1)$$

$$p_k(j+1) = \begin{cases} q_0(j) + \frac{1}{2} a(j+1)H(j) & (k=0) \\ P_k(j+1)H(j+1) & (k \geq 1) \end{cases} \quad (2.2)$$

where  $H(j)$  is the probability that a cell is positive in the  $j$ -th generation:  $H(j) = 1 - q_0(j) = 1 - p_0(j)$ . It is clear that because of (1.13)  $q_0(j) \rightarrow 1$  and  $H(j) \rightarrow 0$  as  $j \rightarrow \infty$ . For the rate of this convergence we have:

### Theorem 2.1

As the process converges to its stationary state so:

$$\frac{H(j)}{H(0)(1-a/2)^j} \rightarrow 1 \quad (j \rightarrow \infty) \quad (2.3)$$

where  $a = e^{-N}$ .

### Proof

Since for  $j \geq 1$

$$H(j+1) = H(j) \frac{1-a(j+1)}{2}$$

so we conclude:

$$H(j+1) = \frac{1-a(1)}{2} \frac{1-a(2)}{2} \dots \frac{1-a(j+1)}{2} H(0) \quad (2.4)$$

Because of (1.13) we are ready.

This theorem indicates that the proportion of the positive cells converges to zero as fast as the  $\left(1 - \frac{a}{2}\right)^j$  function.

## Applications

Our results can be used to estimate the correspondent quantities of other models. Two examples for this are given below:

### Estimation for Model 2

Suppose that the number of replications in a cell follows the Poisson distribution with the expected value of  $N$  and partition occurs according to the classical binomial distribution (Model 2, see [6], [7]):

$$q_k(j) = \begin{cases} p_0(j) & (k=0) \\ \sum_{i=1}^k p_i(j) \frac{N^{k-i}}{(k-i)!} e^{-N} & (k \geq 1) \end{cases} \quad (3.1)$$

$$p_k(j+1) = \sum_{i=k}^{\infty} q_i(j) \binom{i}{k} \left(\frac{1}{2}\right)^i \quad (k \geq 0) \quad (3.2)$$

where (just like before):

$$p_k(j) = \text{Prob}(X(j) = k) \quad q_k(j) = \text{Prob}(Y(j) = k) \\ (k = 0, 1, 2, \dots; j = 0, 1, 2, \dots)$$

Let  $H_2(j)$  be the proportion of the positive cells in the  $j$ -th generation:  $H_2(j) = 1 - p_0(j) = 1 - q_0(j)$ . It can be checked that for  $j \geq 0$ :

$$\begin{aligned} p_0(j+1) &= \sum_{i=0}^{\infty} q_i(j) \left(\frac{1}{2}\right)^i = p_0(j) + \sum_{i=1}^{\infty} q_i(j) \left(\frac{1}{2}\right)^i = \\ &= p_0(j) + \sum_{i=1}^{\infty} \left( e^{-N} \sum_{r=1}^i p_r(j) \frac{N^{i-r}}{(i-r)!} \right) \left(\frac{1}{2}\right)^i \\ p_0(j+1) &= p_0(j) + e^{-N} \left( \sum_{i=0}^{\infty} \frac{N^i}{i!} \left(\frac{1}{2}\right)^i \right) \left( \sum_{i=1}^{\infty} p_i(j) \left(\frac{1}{2}\right)^i \right) \end{aligned}$$

We obtain:

$$\begin{aligned} 1 - p_0(j+1) &= 1 - p_0(j) - e^{-N/2} \left( \sum_{i=1}^{\infty} p_i(j) \left(\frac{1}{2}\right)^i \right) \\ H_2(j+1) &= H_2(j) - e^{-N/2} \left( \sum_{i=1}^{\infty} p_i(j) \left(\frac{1}{2}\right)^i \right) \geq \\ &\geq H_2(j) - e^{-N/2} \sum_{i=1}^{\infty} p_i(j) = H_2(j) - e^{-N/2} H_2(j) \\ H_2(j+1) &\geq H_2(j) (1 - e^{-N/2}) \end{aligned}$$

That is:

$$H_2(j) \geq H_2(0) (1 - e^{-N/2})^j \quad (3.3)$$

It is not difficult to prove (for example, by induction) that the probability of segregation is higher in this model than in our Model 1 (see the Discussion), so if the starting proportion of the positive cells is  $H_2(0) = H(0)$  and the process is close enough to its stationary state then:

$$H(0) (1 - e^{-N/2})^j \leq H_2(j) \leq H(j) \approx \left( 1 - \frac{1}{2} e^{-N} \right)^j H(0) \quad (3.4)$$

### Estimation for Model 3

Suppose that at partition, both daughter cells get one plasmid and the rest of the copies are distributed binomially; the replication follows the above described Poisson distribution. This Model 3 is described in [5].

With the notations used previously:

$$q_k(j) = \begin{cases} p_0(j) & (k=0) \\ \sum_{i=1}^k p_i(j) \frac{N^{k-i}}{(k-i)!} e^{-N} & (k \geq 1) \end{cases} \quad (3.5)$$

$$p_k(j+1) = \begin{cases} q_0(j) + \frac{1}{2} q_1(j) & (k=0) \\ \frac{1}{2} q_1(j) + \sum_{i=2}^{\infty} q_i(j) (i-2) \left(\frac{1}{2}\right)^{i-2} & (k=1) \\ \sum_{i=k+1}^{\infty} q_i(j) \binom{i-2}{k-1} \left(\frac{1}{2}\right)^{i-2} & (k \geq 2) \end{cases} \quad (3.6)$$

Let  $H_3(j)$  be the proportion of the positive cells in this model in the  $j$ -th generation. As can be checked, here the probability of segregation is lower than in the previous models, so – supposing that  $H_3(0) = H(0) = H_2(0)$  – we can conclude that if the process is close enough to its stationary state, then  $H(j) \leq H_3(j)$ .

That is:

$$H(0)(1 - e^{-N/2})^j \leq H_2(j) \leq H(j) \approx \left(1 - \frac{1}{2} e^{-N}\right)^j H(0) \leq H_3(j) \quad (3.7)$$

(3.7) shows that by means of Model 1 it is possible to provide a simple estimation of how fast the proportion of the positive cells converges to zero in other models.

Let the next example be mentioned as a demonstration: in [3] the authors reported that in their experiment the value of  $N$  for plasmid R1 in *E. coli* was between 3 and 4. From this it is estimated that approximately  $10^{-2}$  is an upper boundary for their segregation probability ( $e^{-4} = 0.018$ ). The corresponding parameter given by the authors in their Model 3 in [5] is really less than this value.

## Discussion

The Poisson and the binomial distribution are commonly applied to describe random processes such as replication and partition, since these distributions have been frequently observed in nature for growth and separation (see [1]). By means of the assumptions (1.5) and (1.6) it is possible to prove that in Model 1 the stationary distribution of plasmids in the positive cells is Poissonian again.

The distribution of point-like bodies in space (either molecules or stars) frequently proves to be Poissonian [1], therefore, it is reasonable to suppose this kind of distribution for plasmids in the cells. It is worth emphasizing that this distribution is assumed by several authors, while it is a consequence of Model 1.

A physical interpretation for (1.6) can be obtained, if a difference is made between the two daughter cells: one of them is distinguished by a plasmid and it remains positive at any rate. Segregation occurs only if all the plasmids are

involved in this daughter cell so the other daughter cell becomes negative. It is clear that in this way the segregation probability is lower if any of the daughter cells could become plasmid free (Model 2); and higher than if each daughter cell gains one plasmid (Model 3). In this latter case, segregation occurs only if the mother cell has exactly one plasmid before partition.

It should be noted that even if this interpretation does not correspond to any physiological partitioning mechanism, Model 1 can still be useful as a starting point for estimating procedures, as in the case of the examples described above.

Let us examine the relationship of the average copy number to the segregation probability in Model 1.

Let  $E_X(j)$  and  $E_Y(j)$  denote the expected value of  $X(j)$  and  $Y(j)$ , respectively. It can be shown that for  $j = 0, 1, 2, \dots$ :

$$E_Y(j) = E_X(j) + N \quad (4.1)$$

$$E_X(j+1) = \frac{1}{2}(E_Y(j) + 1) \quad (4.2)$$

and as the process converges to its stationary state:

$$E_X(j) \rightarrow N+1, \quad E_Y(j) \rightarrow 2N+1 \quad (j \rightarrow \infty) \quad (4.3)$$

This means that if the process is close to its stationary state, then for the average plasmid copy number  $C$  we have:

$$C \approx \frac{3}{2}N \quad (4.4)$$

On the basis of (1.13) and (4.4) we can express the segregation probability by means of the average copy number:

$$a \approx e^{-(2/3)C} \quad (4.5)$$

(assuming that the process is not far from its stationary state).

According to (4.5) the segregation probability can be expected to be constant only if the average copy number is constant and it decreases exponentially if the average copy number of the positive cells increases. This is in good accordance with their observations [5].

### Acknowledgement

Thanks are due to Professor KURT NORDSTRÖM for making this research possible.

This work was supported by a grant from the National Swedish Board for Technical Development No. 732-88-01813.

### LITERATURE

1. FELLER, W.: An Introduction to Probability Theory and Its Applications John Wiley & Sons, New York, London, 1957.
2. RIGNEY, D. R.: J. Theor. Biol. 1979 76, 453-480.

3. NORDSTRÖM, K., MOLIN S., and AAGARD-HANSEN, H.: *Plasmid* 1980 4, 215-227
4. HASHIMOTO-GOTOH, T. and ISHII, K.: *A New Mon. Gen. Genet.* 1982 187, 523-525
5. NORDSTRÖM, K. and AAGARD-HANSEN, H.: *Mol. Gen. Genet.* 1984 197, 1-7
6. PRIMROSE, S. B., DERBYSHIRE, P., JONES, I. M., ROBINSON, A. and ELLWOOD, D. C.: *The Application of Continuous Culture to the Study of Plasmid Stability* (in: *Continuous Culture 8: Biotechnology, Medicine and Environment*) Ellis Horwood Ltd., London (1984)
7. SEO, J. H. and BAILEY, J.: *Biotechn. Bioeng.* 1985 27, 156-165.

## APPENDIX

A proof is given here for Theorem 1.1:

(1.8) is valid for  $j=0$ . We go on by mathematical induction. Suppose that (1.8) is valid for some  $j \geq 0$ . Then from (1.3), (1.5), and (1.4):

$$\begin{aligned} Q_k(j) &= \sum_{i=1}^k P_i(j) \frac{N^{k-i}}{(k-i)!} e^{-N} = e^{-2N} \sum_{i=1}^k \frac{N^{i-1}}{(i-1)!} \frac{N^{k-1}}{(k-i)!} = \\ &= e^{-2N} \frac{N^{k-1}}{(k-1)!} \sum_{i=1}^k \binom{k-1}{i-1} = e^{-2N} \frac{(2N)^{k-1}}{(k-1)!} \end{aligned}$$

so also (1.9) is valid for this  $j$ . From this and from (1.4), (1.6) and (1.3):

$$\begin{aligned} P_k(j+1) &= \sum_{i=k}^{\infty} Q_i(j) \left(\frac{1}{2}\right)^{i-1} \binom{i-1}{k-1} = e^{-2N} \sum_{i=k}^{\infty} \frac{(2N)^{i-1}}{(i-1)!} \binom{i-1}{k-1} \left(\frac{1}{2}\right)^{i-1} = \\ &= e^{-2N} \sum_{i=k}^{\infty} \frac{N^{k-1}}{(k-1)!} \frac{N^{i-k}}{(i-k)!} = e^{-2N} \frac{N^{k-1}}{(k-1)!} e^N \end{aligned}$$

so the assertion is true for  $(j+1)$ , too. This proves the theorem.



## THEORETICAL MODEL OF THE REACTION EQUILIBRIA FOR THE UREA-PHOSPHORIC ACID SYSTEM AT THE MOLAR RATIO LESS THAN ONE

M. J. BABIN, R. NENADOV\* and Z. ZRNIC\*

(Faculty of Technology, University of Novi Sad,  
\*Fertilizer Industry "Agrohem", Novi Sad, Yugoslavia)

Received: October 26, 1989

A new theoretical model of the reaction equilibria for the urea-phosphoric acid system at a molar ratio less than one is presented.

The following phase mass ratios: urea-phosphoric acid ( $\psi$ ), urea phosphate-mother liquor solution ( $\theta$ ), mother liquor solution-phosphoric acid solution ( $\kappa$ ) as well as efficiency coefficients for  $P_2O_5$  and urea ( $\eta_{P_2O_5}$ ,  $\eta_u$ ) are evaluated.

The correlations derived for these parameters provide better understanding of the process and could be used in design and control of the urea phosphate production process.

### Introduction

The urea phosphate synthesis by the reaction between urea and phosphoric acid at the molar ratio 1 : 1 is well known and described in literature [1-8].

Urea phosphate production is based on the neutralisation reaction between phosphoric acid and the weak base (urea), similarly to the monoammonium phosphate production by neutralisation of the phosphoric acid with ammonia.

In the reaction system  $CO(NH_2)_2 - H_3PO_4 - H_2O$ , for the molar ratio  $CO(NH_2)_2 : H_3PO_4 < 3,2$  at the equilibrium conditions, the monoprotonated product  $[H_2N - CO - NH_3^+] H_2PO_4^-$  (urea phosphate) as a solid crystalline phase is precipitated.

At the molar ratio between 3.2 and 1 the corresponding liquid phase contains urea and urea phosphate, but for a molar ratio less than one, the solution contains phosphoric acid and urea phosphate.

In most references, the urea phosphate production process at the molar urea-phosphoric acid ratio close to one is described [5-7]. Under these conditions, the quantity of the urea phosphate crystals increases with the increase

of the phosphoric acid concentration, but decreases with the temperature increase [8].

With the excess of phosphoric acid, i. e. at the molar ratio  $\text{CO}(\text{NH}_2)_2 : \text{H}_3\text{PO}_4 < 1$  the reaction between phosphoric acid and urea is essentially reduced to the monoprotonation of nitrogen atoms. This reaction is of ionic character and practically is completed when the urea is dissolved. Further separation of the urea phosphate crystals, up to equilibrium with the mother liquor, depends on the solubility of urea phosphate in phosphoric acid.

Investigation of the influence of raw phosphoric acid impurities ( $\text{H}_2\text{SO}_4$ ,  $\text{H}_2\text{SiF}_6$ ,  $(\text{Fe}, \text{Al})\text{PO}_4$ ) on the urea phosphate solubility have shown that no significant difference in UP solubility for raw and pure phosphoric acid exists [9].

As previously pointed out, the key process parameter is not the reaction velocity, but the mass equilibrium ratio of crystalline urea phosphate to the corresponding mother liquor solution [10].

### Experimental

For testing the theoretical equilibrium model on experimental data, the urea with 46.2% N, produced by HIP "Pančevo", (YU) and the raw phosphoric acid with 51.4%  $\text{P}_2\text{O}_5$  produced by IHP "Prahovo", Prahovo (YU) were used. The solution concentrations of  $\text{H}_3\text{PO}_4$  between 30 and 50%  $\text{P}_2\text{O}_5$  were obtained by dilution.

Reaction was carried out in a cylindrical reaction vessel (200 cm<sup>3</sup>) equipped by a ( $D/H = 1$ ;  $d/D = 0.5$ ;  $n = 1000$  rpm) mech. stirrer and a shell for maintaining the constant level of temperature ( $\pm 0.5$  °C).

Solid urea was added into phosphoric acid at 70 °C up to the complete dissolution. After that, the reactor content was cooled to the selected temperature in the range of 10–40 °C. Crystallisation starts spontaneously by gaining saturation at a selected lower temperature level and is completed in 0.5 hr attaining an equilibrium state. In the absence of crystallisation (super-saturated solution), it was promoted by adding a small quantity of UP crystalline powder. The crystalline urea phosphate was rapidly separated from the liquid phase by the vacuum filtration, and crystals were washed with acetone and dried at 80 °C.

The contents of  $\text{P}_2\text{O}_5$  and  $N_{\text{amid}}$  were estimated by standard procedures [11, 12].

### Setting Up the Equilibrium Model

Setting up the theoretical equilibrium model for the urea-phosphoric acid reaction system at the molar urea-phosphoric acid ratio less than one was performed by a procedure, which is similar to that proposed earlier [10].

The relationship between the starting and the final (equilibrium) states of the system  $\text{CO}(\text{NH}_2)_2 - \text{H}_3\text{PO}_4 - \text{H}_2\text{O}$  can be represented by the following scheme:



The corresponding mass balance is:

$$m_U + m_{\text{HP}} = m_{\text{CR}} + m_{\text{ML}} \quad (2)$$

It is suitable to introduce the following nondimensional parameters:

$$\psi = \frac{m_U}{m_{\text{HP}}} \quad (3)$$

$$\kappa = \frac{m_{\text{ML}}}{m_{\text{HP}}} \quad (4)$$

$$\theta = \frac{m_{\text{CR}}}{m_{\text{ML}}} \quad (5)$$

Therefore, it is more practical to perform their indirect estimation from the measurement of the concentrations  $C_{\text{P}_2\text{O}_5(\text{HP})}$  and  $C_{\text{P}_2\text{O}_5(\text{ML})}$ .

Thus, for  $\psi$  and  $\kappa$  the following equations are used [10]:

$$\psi = \varphi \cdot K_1 \cdot C_{\text{P}_2\text{O}_5(\text{HP})} \quad (6)$$

$$\kappa = (1 - \eta_{\text{P}_2\text{O}_5}) \cdot \frac{C_{\text{P}_2\text{O}_5(\text{HP})}}{C_{\text{P}_2\text{O}_5(\text{ML})}} \quad (7)$$

Using the procedure proposed in [10] one can derive the equation for  $\theta$ :

$$\theta = \frac{1}{C_{\text{P}_2\text{O}_5(\text{HP})}} + \varphi \cdot K_1 \cdot C_{\text{P}_2\text{O}_5(\text{ML})} - 1 \quad (8)$$

According to the definition, the concentration  $C_{\text{P}_2\text{O}_5(\text{ML})}$  can be represented by:

$$C_{\text{P}_2\text{O}_5(\text{ML})} = \frac{m_{\text{UP}} \cdot K_2 + \frac{m_{\text{HP}}}{K_3}}{m_{\text{ML}}} \quad (9)$$

Accepting that the solubilities of urea phosphate S in pure and raw phosphoric acid are approximately the same [9] the mass of mother liquor solution could be estimated from the solubility of urea phosphate in pure phosphoric acid:

$$m_{\text{ML}} = \frac{m_{\text{UP}}(S + 100)}{S} \quad (10)$$

According to the definition, the concentration of phosphoric acid, which appears as a solvent of urea phosphate, could be expressed as follows:

$$C'_{\text{P}_2\text{O}_5(\text{HP})} = \frac{m'_{\text{HP}}}{m_{\text{H}_2\text{O}}} + m'_{\text{HP}} \cdot \frac{1}{K_3} \quad (11)$$

where  $m'_{\text{HP}}$  is the mass of the free phosphoric acid. Eq. (11) can easily be transformed into:

$$\frac{1-\varphi}{\frac{1}{C_{P_2O_5(HP)^*}} - K_3 \cdot \varphi} = C'_{P_2O_5(HP)} \quad (12)$$

One can write for the urea phosphate solubility in phosphoric acid as solvent, in agreement with the definition:

$$S = \frac{m_{UP} \cdot 100}{m_{H_2O} + m'_{HP}} \quad (13)$$

By substitution of  $m_{ML}$ ,  $m_{UP}$  and  $m'_{HP}$  from Eq. (10)–(13) into Eq. (9) one obtains:

$$C_{P_2O_5(MR)} = \left[ K_2 \cdot S + \frac{(1-\varphi) \cdot 100}{\frac{1}{C_{P_2O_5(HP)}} - K_3 \cdot \varphi} \right] \cdot \frac{1}{S+100} \quad (14)$$

The mass of phosphoric acid appearing in excess as the solvent, could be calculated from:

$$m'_{HP} = m_{P_2O_5} \cdot K_2 - m_U \cdot K_4 = m_{HP} - m_U \cdot K_4 \quad (15)$$

where:  $m_U/m_{P_2O_5} = \varphi \cdot K_1$

Using Eq. (7), i. e. Eq. (4) and Eq. (9) one derives:

$$1 - \eta_{P_2O_5} = \frac{m_{UP} \cdot K_2 + \frac{m'_{HP}}{K_3}}{m_{P_2O_5}} \quad (16)$$

From Eq. (11)–(13) one obtains:

$$\frac{\frac{m_{UP} \cdot 100}{m'_{HP}}}{a) C = C_{P_2O_5(HP)}; C' = C'_{P_2O_5(HP)}} = \frac{S}{K_3 \cdot C'} \quad (17)$$

Using Eq. (12) and Eq. (15)–(17) the following Equation for the  $P_2O_5$  efficiency coefficient can be derived:

$$\eta_{P_2O_5} = \varphi - \left( \frac{1}{C_{P_2O_5(HP)}} - K_3 \cdot \varphi \right) \cdot \frac{K_2 \cdot S}{100} \quad (18)$$

If the molar ratio  $CO(NH_2)_2 : H_3PO_4$  is less than one, it is more useful to apply the urea efficiency coefficient  $\eta_U$ :

Expanding the ratio in the definition equation for  $\eta_{P_2O_5}$

$$\eta_{P_2O_5} = \frac{m_{CR} \cdot C_{P_2O_5(CR)}}{m_{P_2O_5}} \quad (19)$$

by  $2 \cdot m_U \cdot C_{U(CR)} \cdot M_U \cdot M_{P_2O_5}$  results in:

$$\eta_{P_2O_5} = \eta_U \cdot K_1 \cdot \varphi \cdot \frac{C_{P_2O_5(CR)}}{C_{U(CR)}} \quad (20)$$

Obtaining pure UP crystals after separation of the mother liquor, Equation (20) becomes very simple:

$$\eta_U = \frac{\eta_{P_2O_5}}{\varphi} \quad (21)$$

Replacing concentration  $C$  with  $C'$  with the aid of Eq. (12), one can rewrite Eq. (18) as follows:

$$\eta_{P_2O_5} = \varphi - \frac{(1-\varphi) \cdot K_2 \cdot S}{C' \cdot 100} \quad (22)$$

The resulting equation (22) is more suitable for application than the original one (18), because the urea phosphate solubility is a function of temperature and concentration  $C'$ , according to the empirical relation [13]:

$$S(C', T) = 0.01241 \cdot \exp [0.030722 \cdot T - (2.9607 \cdot 10^{32} \cdot T^{-14.0377} + 0.03500) \cdot C'] \quad (23)$$

where  $C'$  is in %,  $T$  in  $K$  and  $S$  in  $g/100 g$ .

In order to avoid the application of the complex term (23) in Eq. (22), i. e. to eliminate temperature as a variable it is possible to combine Eq. (14) and Eq. (18) to obtain:

$$\eta_{P_2O_5} = \frac{\left( \frac{\varphi}{K_2} + A \cdot K_3 \right) \cdot C_{P_2O_5 (ML)} - 1}{\frac{C_{P_2O_5 (ML)}}{K_2} - 1} \quad (24)$$

$$A = \frac{1}{K_3 \cdot C_{P_2O_5 (HP)}} - \varphi$$

Parameter  $C_{P_2O_5 (ML)}$  is a function of concentration  $C$ , molar ratio  $\varphi$  and temperature, and it can easily be estimated by chemical analysis.

Substituting parameters  $C_{P_2O_5 (ML)}$  and  $\eta_{P_2O_5}$  in Eq. (8) by expressions (14) and (18), respectively, the function  $\theta(C, \varphi, S)$  can be formulated as:

$$\theta = \frac{\left( \frac{1}{C_{P_2O_5 (HP)}} + K_1 \cdot \varphi \right)}{\left( \frac{1}{C_{P_2O_5 (HP)}} - K_3 \cdot \varphi \right)} \cdot \frac{100}{(S+100)} - 1 \quad (25)$$

The function  $\theta(C', \varphi, S)$  can be derived analogously as for Eq. (22) which enables the application of  $\theta(C', \varphi, T)$  function, i. e.  $\theta(C, \varphi, T)$  function.

The influence of temperature as parameters, i. e. the application of the complex empirical relationship  $S(C', T)$  could also be avoided by the elimination of factor  $S$  from Eq. (18) and (25), and obtaining the equation:

$$\eta_{P_2O_5} = \varphi - \left[ \frac{1}{C_{P_2O_5(HP)}} + K_1 \cdot \varphi - \left( \frac{1}{C_{P_2O_5(HP)}} - K_3 \cdot \varphi \right) \right] \cdot K_2 \quad (26)$$

Eq. (26) subsequently combines two basic parameters:

$\theta$  main factor influencing the process and

$\eta$  correspondingly influencing the process and process economy.

Similarly as in Eq. (22), concentration  $C$  in Eq. (25) may be replaced by  $C'$  resulting in the function  $\theta(C', \varphi, S)$  and further in the function  $\theta(C', \varphi, T)$  through the correlation (23). Finally using Eq. (12) one can switch from  $\theta(C', \varphi, T)$  to  $\theta(C, \varphi, T)$ , the latter function being the most useful in application.

### Result and Discussion

Experimental testing of the obtained correlations illustrated by Eq. (6), (12), (18) and (21)–(26) is performed by the synthesis of UP described above and the results are comparatively given in *Table 1*.

*Table 1* illustrates satisfactory agreement between the experimental and calculated values showing the similarity of  $H_3PO_4 - CO(NH_2)_2 - H_2O$  systems for: pure phosphoric acid-urea and technical phosphoric acid-urea. This offers the possibility of the practical application of the relationships and functions evaluated here as in our previous work [10].

The mass ratio  $\theta$ , as the most important parameter of the process (Eq. 25)

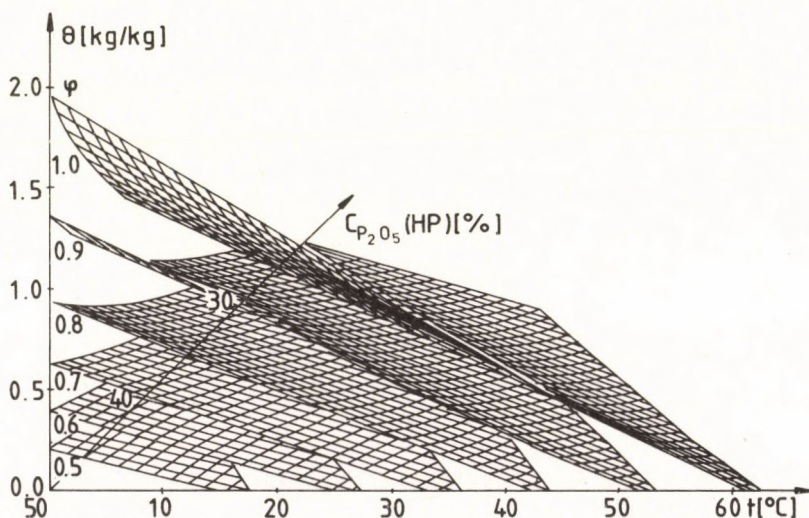


Fig. 1.

Graphical 3d-presentation of the  $\theta(C, \varphi, T)$  function.

Table 1.

Calculated and experimentally obtained values of parameters  $\eta_{P_2O_5}$ ,  $\eta_U$ ,  $\theta$  and  $\kappa$  as a function of the phosphoric acid concentration, temperature (UP solubility) and molar ratio urea-phosphoric acid.

Table 1.

Parameters	<i>t</i> [°C]	$C_{P_2O_5(H_2O)}(\varphi)$ [%] [1]							
		35 (1)		40 (0.9)		45 (0.8)		50 (0.7)	
$\theta_{\text{Cal, E}}$ [kg/kg]	10	0.423	0.458	0.699	0.685	0.945	1.044	1.092	1.049
		0.911	0.889	0.768	0.774	0.670	0.639	0.702	0.632
		0.495	0.500	0.603	0.570	0.633	0.637	0.608	0.571
		0.495	0.530	0.671	0.671	0.792	0.843	0.869	0.863
$\kappa_{\text{Cal, E}}$ [kg/kg]	20	0.264	0.274	0.498	0.470	0.769	0.767	0.930	0.925
		1.025	1.017	0.871	0.883	0.738	0.738	0.671	0.692
		0.347	0.350	0.487	0.463	0.566	0.554	0.561	0.548
		0.347	0.362	0.542	0.532	0.708	0.716	0.801	0.810
$\eta_{P_2O_5 \text{Cal, E}}$ [1]	30	0.080	0.082	0.305	0.298	0.535	0.540	0.716	0.691
		1.200	1.197	0.999	1.005	0.849	0.847	0.755	0.766
		0.123	0.121	0.342	0.322	0.454	0.437	0.486	0.455
		0.123	0.128	0.380	0.378	0.568	0.578	0.695	0.689
$\eta_U \text{Cal, E}$ [1]	40	–	–	0.065	0.051	0.311	0.320	0.531	0.606
		–	–	1.225	1.241	0.995	0.984	0.846	0.807
		–	–	0.090	0.068	0.309	0.306	0.404	0.421
		–	–	0.103	0.080	0.387	0.405	0.577	0.636
$m_{H_3PO_4}$ [g]		137.78		153.10		172.22		196.84	
$m_U$ [g]		60.00		60.00		60.00		60.00	
$m_{H_2O}$ [g]		65.08		44.14		25.00		6.02	
$m_{CR}$ [g]	10	82.60		104.60		131.40		134.60	
	20	56.50		83.00		111.70		126.30	
	30	20.00		59.00		90.20		107.40	
	40	–		12.40		63.20		99.20	

Cal = calculated

E = experimental

can be described by the complex function  $\theta(C, \varphi, T)$ , useful in practical application, with the aid of Eq. (12) and (23).

The function  $\theta(C, \varphi, T)$  is presented in 3d-diagram, Fig. 1.

Two partial functions  $\theta(\varphi, T)$  and  $\theta(C, \varphi)$  as projections of the  $\theta(C, \varphi, T)$  function are both presented in the diagram in Fig. 2.

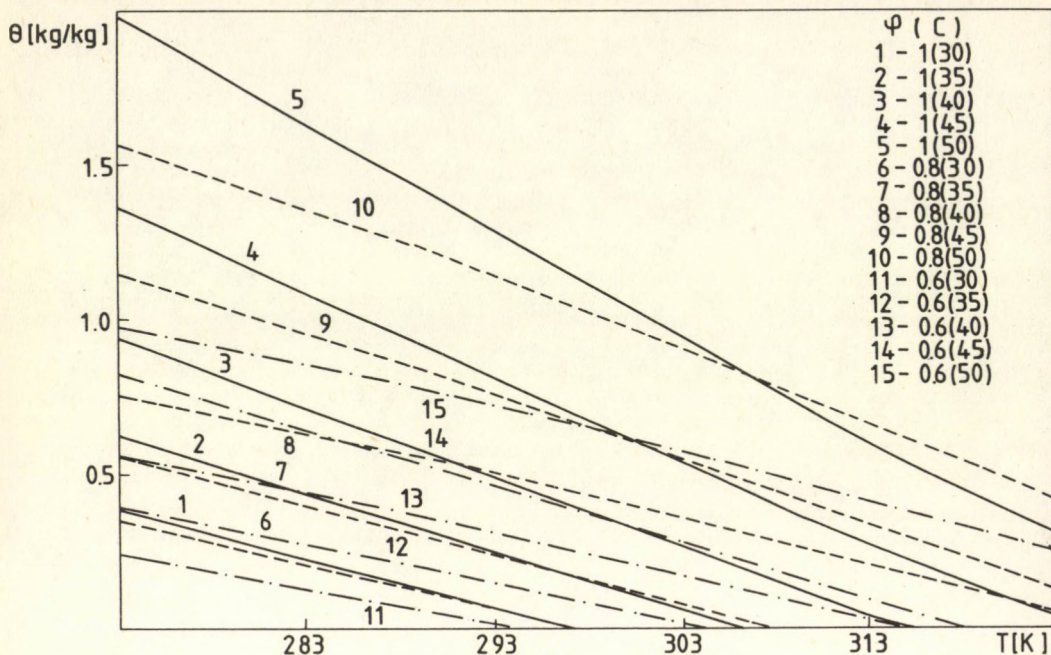


Fig. 2.

Graphical presentation of  $\theta$  as a temperature function for some phosphoric acid concentrations and molar  $\varphi$  ratios.

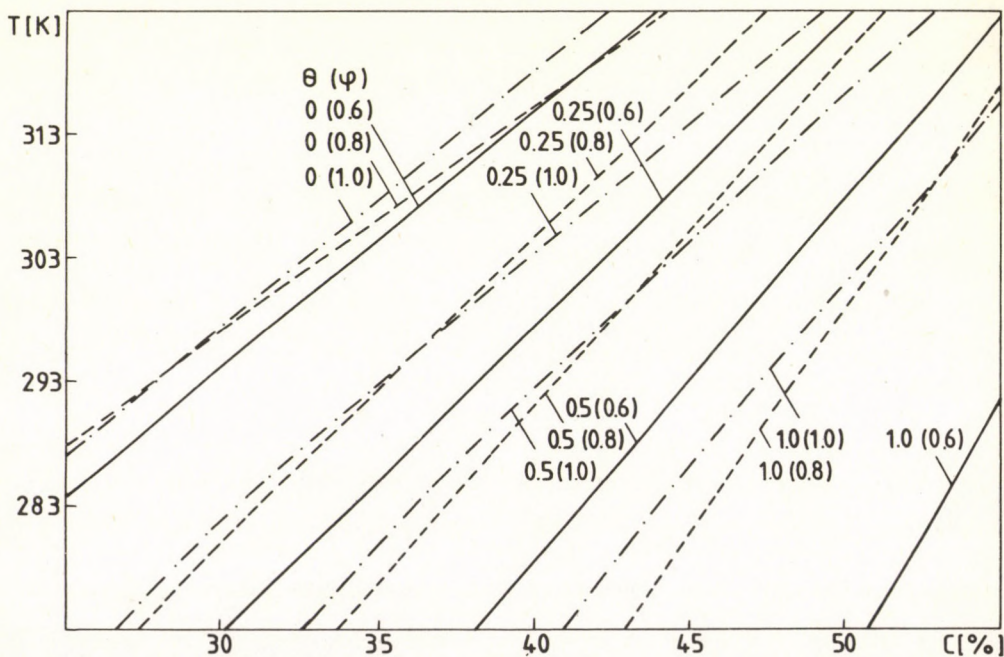


Fig. 3.

Graphical presentation of  $T(C)$  partial function for constant  $\theta$  values.

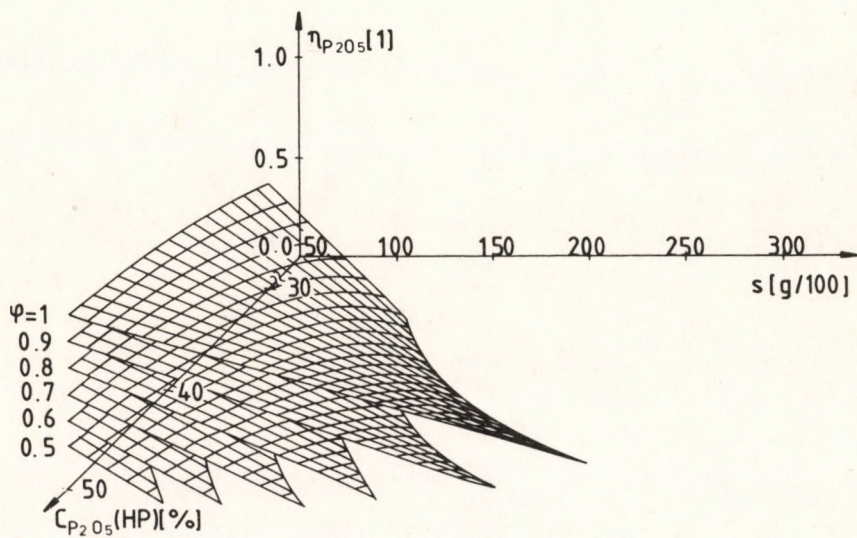


Fig. 4.  
Graphical 3d-presentation of  $\eta_{P_2O_5}(C, \varphi, S)$  function.

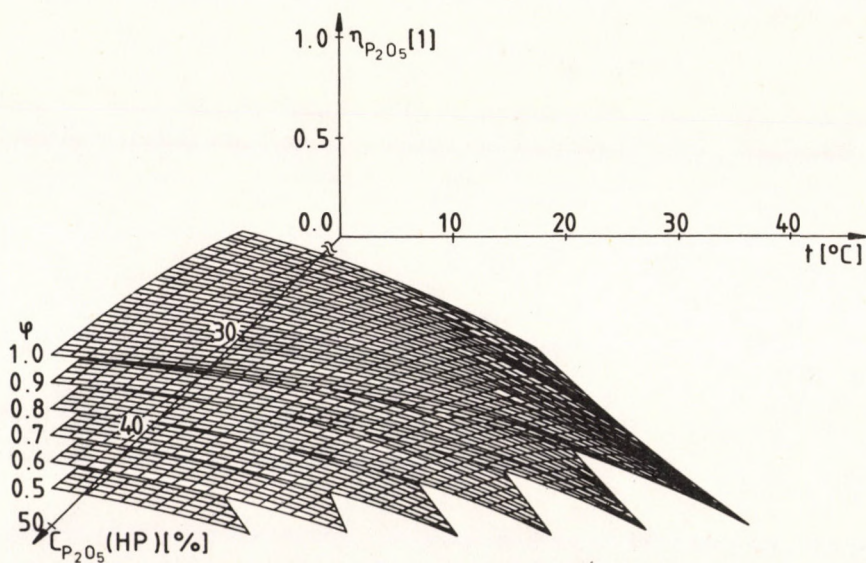


Fig. 5.  
Graphical 3d-presentation of  $\eta_{P_2O_5}(C, \varphi, T)$  function.

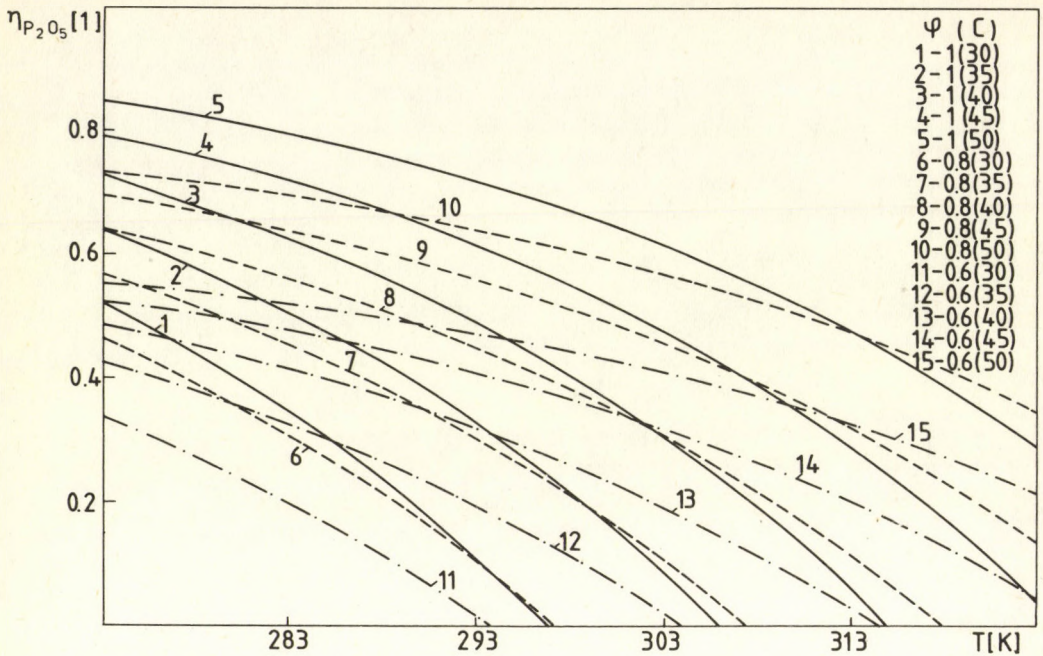


Fig. 6.

Graphical presentation of  $\eta_{P_2O_5}$  as a temperature function for some phosphoric acid concentrations and molar  $\varphi$  ratios.

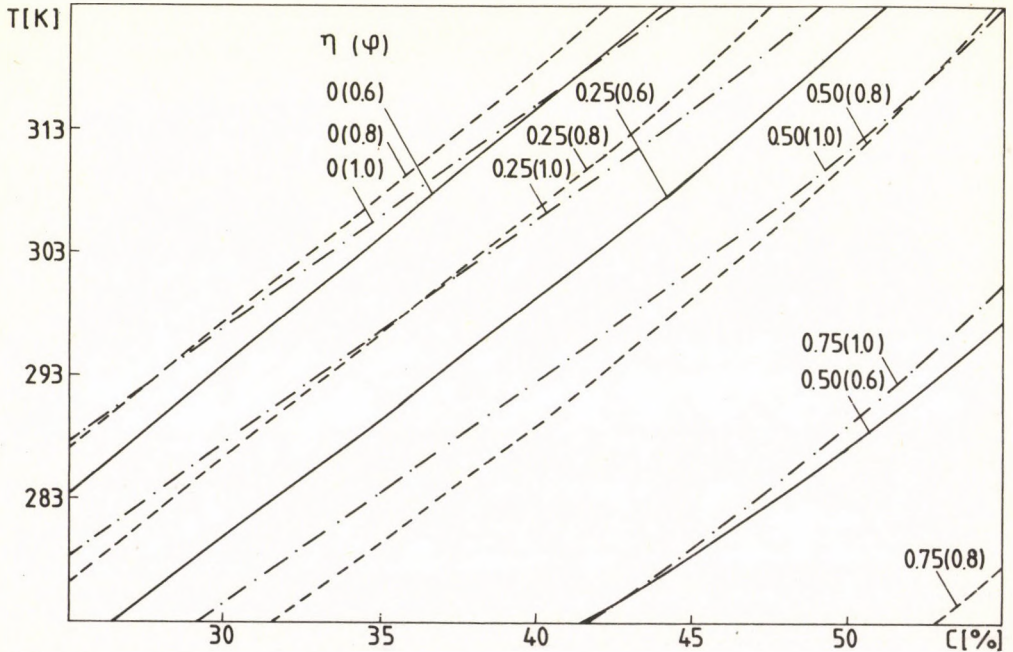


Fig. 7.

Graphical presentation of the  $T(C)$  partial function for constant  $\eta_{P_2O_5}$  values.

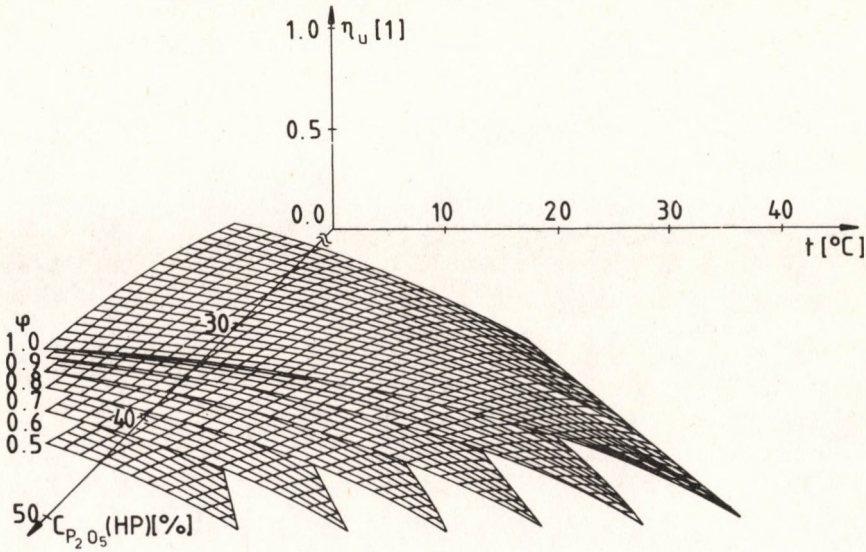


Fig. 8. Graphical 3d-presentation of  $\eta_U (C, \varphi, T)$  function

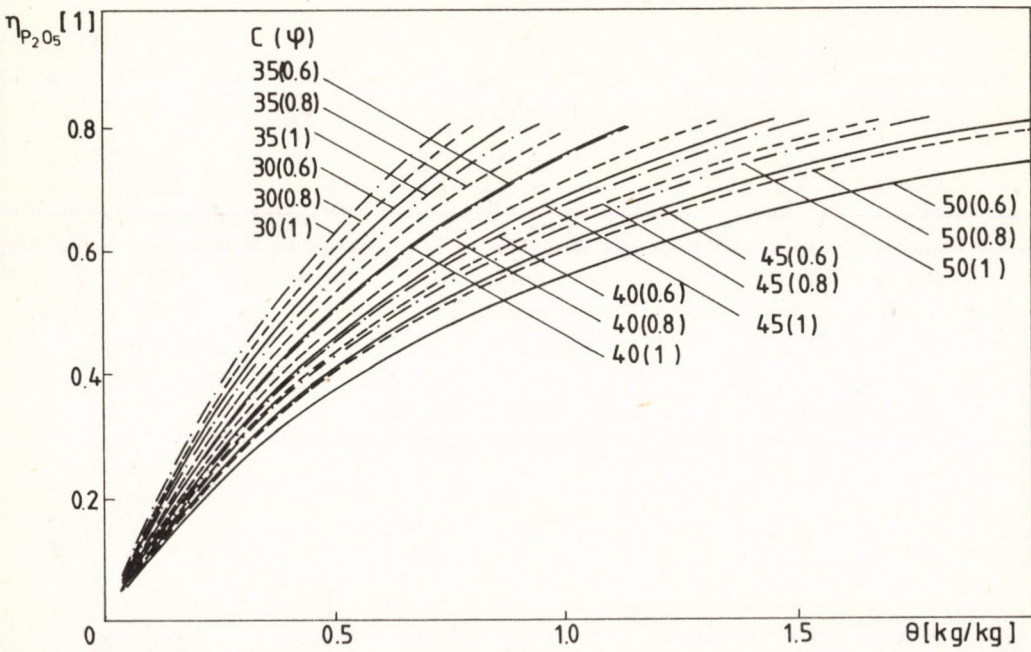


Fig. 9. Graphical presentation of the correlation between  $P_2O_5$  efficiency coefficient and UP pulp density  $\theta$ .

From Fig. 2 it is seen that some chosen values of  $\theta$ , which are directly correlated with the quality (purity) of UP crystals, can be realized in different ways through a complex change of the  $C$ ,  $\varphi$ ,  $T$  parameters.

Fig. 3 gives the third partial function  $T(C)$  (base projection of  $\theta(C, \varphi, T)$  function), which for the condition of  $\theta(C, \varphi, T) = 0$  shows the system limitations. In that respect, the curve  $T(C)$  at  $\theta = 0$ ,  $\varphi = 1$  divides the  $T-C$  field in two regions: the working area-below the curve and the upper area in which the crystallisation process is missing.

The correlation for the  $P_2O_5$  efficiency coefficient, being the most important techno-economical parameter of the process, given by Eq. (18), is shown by the 3d-diagram in Fig. 4.

In order to enable a simpler application of the  $\eta_{P_2O_5}$  function, it is presented as  $\eta_{P_2O_5}(C, \varphi, T)$  in Fig. 5.

The partial function  $\eta_{P_2O_5}(\varphi, T)$  and  $\eta_{P_2O_5}(C, \varphi)$  are together presented in Fig. 6 and the corresponding function  $T(C)$  in Fig. 7.

Instead of  $\eta_{P_2O_5}$ , more useful in application, at the molar ratio urea-phosphoric acid less than one, is the urea efficiency coefficient, which is presented in Fig. 8.

The correlation between  $P_2O_5$  efficiency coefficient and the crystalline pulp density  $\theta$  (Eq. 26) is illustrated in Fig. 9.

### Conclusion

A new theoretical model of the reaction equilibria for the urea-phosphoric acid system at the molar ratio  $CO(NH_2)_2 : H_3PO_4 < 1$  is presented.

The parameters obtained in this study are for the phases mass ratio: urea-phosphoric acid ( $\psi$ ), urea phosphate-mother liquor solution ( $\theta$ ), mother liquor solution-phosphoric acid solution ( $\kappa$ ) and the efficiency coefficients for  $P_2O_5$  and urea ( $\eta_{P_2O_5}$ ,  $\eta_U$ )

Correlations derived from these parameters could provide better understanding and control of the urea phosphate production process, as well as in designing the corresponding process equipment.

On the basis of the proposed correlations for mass ratio  $\psi$ ,  $\theta$  and  $\kappa$  an indirect determination of these parameters is possible by measuring the concentration parameters, thus avoiding the use of mass balance.

### SYMBOLS

$U_{(S)}$	urea solid phase	
$HP_{(L)}$	phosphoric acid liquid phase	
$CR_{(S)}$	urea phosphate crystalline phase	
$ML_{(L)}$	liquid phase of the mother liquor	
$\psi$	solid-liquid phase ratio at the beginning of the reaction	[kg/kg]
$\theta$	equilibrium solid-liquid phase ratio	[kg/kg]
$\kappa$	liquid-liquid phase ratio of the mother liquor and phosphoric acid	[kg/kg]

$\eta_{P_2O_5}$	$P_2O_5$ efficiency coefficient	[1]
$\eta_U$	urea efficiency coefficient	[1]
$M_s$	molar mass of the substance $S(S=UP, H_2O, P_2O_5, H_3PO_4)$	(kg/kmol)
$m_s$	mass of the substance S	[kg]
$m_F$	mass of the phase $F(F=U, HP, CR, ML)$	[kg]
$C_{S(F)}$	mass fraction (concentration) of the constituent S in the phase F	[kg/kg], [%]
$n_s$	number of mols of the substance S	[mol]
$K_1, K_2$	stoichiometric factors $\frac{2M_U}{M_{P_2O_5}}, \frac{M_{P_2O_5}}{2M_{UP}}$	
$K_3, K_4$	$\frac{2M_{H_3PO_4}}{M_{P_2O_5}}, \frac{M_{H_3PO_4}}{M_U}$	
$\varphi$	molar ratio urea-phosphoric acid	[mol/mol]
S	urea phosphate solubility	[g/100 g]
$m'_{HP}$	mass of free phosphoric acid	[kg]
$C_{P_2O_5(HP)}$	concentration of free phosphoric acid	[kg/kg], [%]
[K]	temperature	HT, t [°C]
$d_m$	mixer diameter	[m]
h	liquid layer height	[m]
d	diameter of mixing profile	[m]

## LITERATURE

- HARDESTI, DZH.: *Khim. i Khim. technol.* 1956, 6, 63.
- VOLL'FKOVICH, S. I., CHEKHOVSKIKH, A. I. i MIKHALEVA, T. K.: *Khim. prom.* 1970, 9, 676.
- FOWLER, C. W.: urea and urea Phosphate Fertilizers, Noyes Data Corp., Parke Ridge N. J., 1976.
- MCCULLOUGH, J. F., SHERIDAN, R. C. and LELAND, F. L.: *J. Agr. Food Chem.* 1978, 26, 670.
- Czech Pat. 177, 578.
- Germ. (East) Pat. 128, 300.
- S. African. Pat. 7805, 520.
- HUSSEIN, M., ZATOUT, A. A., HOSNY, A. Y.: *Afinidad (Egypt)* 1980, 37 (367), 223.
- VIDZHESINEKH, B., KUZNETSOVA, A. G., TOROCHESNIKOV, N. S. i KOZLOVA, G. A.: *Zh. Prikl. Khim.* 1976, 49 (9), 2074.
- BABIN, M. J., NENADOV, R. i ZRNIC, Z.: *Kem. Ind.* 1989, 38 (3), 123.
- JUS (Yu standard): H. B8. 287 (1983).
- Ibid.: HB-8066 (1967).
- BABIN, M. J., NENADOV, R. i ZRNIC, Z.: *Kem. Ind.* 1990, 39 (2), 51.



## EFFECT OF THE CRYSTAL SHAPE ON CRYSTAL SIZE DISTRIBUTION MEASURED BY THE PHOTSEDIMENTATION TECHNIQUE, MICROSCOPY AND SIEVING

MRS. I. LISZI, J. HOSTOMSKÝ\*, ZS. HALÁSZ AND J. NÝVLT\*

(Research Institute of Technical Chemistry, Hungarian Academy of Sciences, 8200 Veszprém, Hungary; \* Institute of Inorganic Chemistry, Czechoslovak Academy of Sciences, 16000 Prague 6, Czechoslovakia)

Received: December 21, 1989

The crystal size distributions of samples of copper sulphate pentahydrate (regular crystals), acetylsalicylic acid (crystals with a wide variability of the length-to-width ratio) and potassium aluminium sulphate (agglomerated crystals) were determined using the photosedimentation technique, sieve analysis and optical microscopy. The variability of particle shapes was taken into account in the calculation procedures used to check the consistency of size distributions measured by different methods. Satisfactory agreement was obtained on the size distributions put to the same basis, when particle shapes were approximated by appropriate geometric bodies (prisms and ellipsoids) with size-dependent proportions.

### Introduction

The measurement of the crystal size distribution is important in both research work and the routine quality control of crystalline products. It is well known that a direct comparison of results obtained by different methods is only possible for spheres with uniform density. When the particle shapes diverge from the spherical, the difference between data sets becomes more pronounced. To characterize and measure the particle shapes is a difficult task and no universal particle shape characterization scheme is so far available. A number of approaches were proposed [1], ranging from the characterization of the particle shape by a single factor (e.g. sphericity  $\psi$ , the ratio of the surface area of a sphere having the same volume as the particle to the surface area of the particle) to elaborate procedures using Fourier analysis [2] or fractal dimensions [3] to quantify particle shapes or, rather, two-dimensional projections of the particles.

In contrast to irregular particle shapes encountered in many processes of powder technology, particles obtained by crystallization of substances from a solution are often of relatively simple and regular shapes. Sieving, microscopy and methods based on the sedimentation of particles in a fluid medium are among the major techniques used for size analysis in crystallization practice. In a previous paper [4], we summarized and evaluated theoretical relationships and published experimental data for the sedimentation behaviour of non-spherical particles. Good agreement was obtained between the size distributions measured by the photosedimentation technique and by microscopy, assuming that the crystals may be approximated by appropriate geometric bodies (prisms and ellipsoids) with fixed relative proportions.

On the other hand, the crystals may exhibit a size dependence of their relative proportions [5] or even a distribution of their relative proportions for a given characteristic size, as a consequence of differences in linear growth rates in different crystallographic directions or the effects of crystal attrition and breakage. Further more, individual crystals may adhere to one another and grow into agglomerates.

The objective of this work is to extend the approach used in a previous paper [4] to samples of crystals exhibiting variability in their relative proportions, as well as agglomerating crystals; the photosedimentation technique, optical microscopy and sieving are used as methods of measurement.

### Theoretical

Size data obtained by a sedimentation method are usually expressed in terms of the equivalent Stokes diameter,  $d_{st}$  i.e. the diameter of a sphere having the same density as the particle and with the same terminal settling velocity  $u$  in an unbound fluid in the Stokes flow region (Reynolds number  $Re = ud_{st}\rho/\mu$  lower than about 0.2). Generally, nonspherical particles may exhibit a rotating and spiralling motion as they settle in a gravitational field. According to HAPPEL and BRENNER [6], a particle with three perpendicular planes of symmetry (an orthotropic particle in their terminology, e.g. a rectangular prism, cylinder and ellipsoid) settling in the Stokes flow region will reach a steady state of motion in which it does not change its orientation. The hydrodynamic resistance of a settling orthotropic particle is characterized by three coefficients (drag diameters)  $d_1, d_2, d_3$ . For example, the force  $F_1$  acting on an orthotropic particle settling with its axis  $x_1$  oriented vertically is:

$$F_1 = 3\pi d_1 \mu u_1 \quad (1)$$

and its terminal velocity  $u_1$  is:

$$u_1 = \frac{\Delta \rho g d_v^2}{18 \mu d_1} \quad (2)$$

For a non-spherical orthotropic particle, the drag diameters  $d_1$ ,  $d_2$ ,  $d_3$  are different and, therefore, a set of identical orthotropic particles will in general exhibit a spread in settling velocities owing to the orientation dependence of the settling velocity. Assuming that all particle orientations are equally probable, HAPPEL and BRENNER [6] derived a relationship for the integral mean value of the settling velocity  $\bar{u}$ :

$$\bar{u} = \frac{\Delta \rho g d_v^3}{18 \mu \bar{d}} \quad (3)$$

where  $\bar{d}$  is the average drag diameter of the orthotropic particle:

$$\frac{1}{\bar{d}} = \frac{1}{3} \left( \frac{1}{d_1} + \frac{1}{d_2} + \frac{1}{d_3} \right) \quad (4)$$

and  $d_i$  ( $i = 1, 2, 3$ ) are the drag diameters of the settling particle with its axis  $x_i$  oriented vertically. By comparing Eq. (3) with the Stokes formula for a settling sphere, we obtain for the average Stokes diameter of an orthotropic particle:

$$\bar{d}_{St} = d_v \left( \frac{d_v}{\bar{d}} \right)^{1/2} \quad (5)$$

The average drag diameters for several types of orthotropic bodies were summarized in [4]. For most particle shapes, the data for the drag diameters are not available. An approximate relationship can then be used [7]:

$$\bar{d}_{St} \cong d_v \left( \frac{d_v}{d_s} \right)^{1/2} = d_v \psi^{1/4} \quad (6)$$

i.e., it is supposed that the mean drag diameter is equal to the surface diameter of the particle  $d_s$  which is defined as the diameter of the sphere having the same surface area as the particle; sphericity  $\psi$  is then equal to  $d_v^2/d_s^2$ . Equation (6) is only valid for convex particles (i.e. for particles not exhibiting surface concavities). It was demonstrated [4] that for values of sphericity greater than about 0.5, Eq. (6) adequately represents the theoretical results for ellipsoids, as well as experimental data for cylinders, rectangular prisms and polyhedrons.

As far as the sedimentation behaviour is concerned, it is not critical whether the particle is approximated by an ellipsoid (a generalized sphere), a rectangular prism or a cylinder, provided that these bodies are of the same volume and of the same relative proportions. This fact is demonstrated in *Table 1*. It is of interest to note that even for a very elongated ellipsoid with axes ratio 10 : 1 : 1, the correction factor  $(d_v/\bar{d})^{1/2}$  in Eq. (6) for the calculation of the average Stokes diameter is relatively well approximated by  $\psi^{1/4}$ .

## Experimental

### *Materials*

The size distribution measurements were carried out for four different types of materials with an increasing degree of shape complexity:

- glass spheres (test material);
- angular crystals of copper sulphate pentahydrate, sieve cut 200 to 315  $\mu\text{m}$ ;
- needle-shaped crystals of acetylsalicylic acid with varying length/width ratio;
- partially agglomerated crystals of potassium aluminium sulphate dodecahydrate, sieve cut 1000 to 1250  $\mu\text{m}$ .

### *Methods of Measurements*

#### 1. Photosedimentation technique

The Bound-Brook photosedimentometer was used in the sedimentation size analysis. Solutions with suitable physical properties were prepared by saturating a glycerine-water mixture or ethanol with the material to be measured; the range of Reynolds numbers was 0.065 to 0.096. Measurements were carried out within the region of validity of the Lambert-Beer law. The maximum solids concentration (for large crystals of potash alum) was less than 1% vol. Three replicate analyses were made with each sample. The measurement gives a plot of cumulative undersize fraction of mean projected area of particles  $A(\bar{d}_{St})$  against the average Stokes diameter  $\bar{d}_{St}$ .

#### 2. Microscopy

By measuring the projected particle dimensions from photomicrographs, the characteristic dimensions  $L_L$  and  $L_W$  as defined by HEYWOOD [9] were determined: the width  $L_W$  is the minimum distance between two parallel lines touching the opposite sides of the particle silhouette; the length  $L_L$  is the distance between two parallel lines perpendicular to the lines defining  $L_W$  and tangent to the particle silhouette. The projected surface area of a particle was taken as  $L_L L_W$  in the calculation of the cumulative fraction of projected particle surface area  $A(L_W)$ . The thickness  $L_T$  is defined as the distance between two parallel planes, which are tangent to opposite surfaces of the particle, one plane being the plane of maximum stability. The values of  $L_T$  were determined for a limited number of particles by focusing the microscope on the upper and then on the lower surface of the particle.

Besides the manual evaluation of photomicrographs, samples of acetylsalicylic acid crystals were also analyzed, using a Leitz-Classimat image analyzer. The instrument utilized an optical microscope to obtain a video image of a particulate sample. The projected surface area of individual particles was measured

and the surface area distribution was evaluated; the characteristic size is the maximum length of a horizontal cord drawn through the particle silhouette.

### 3. Sieving

The sieve cuts of copper sulphate and potash alum crystals were obtained by sieving these materials for 15 minutes on a sieve shaker with standard analytical sieves of 200  $\mu\text{m}$  diameter. In the sieve analysis of glass spheres and acetylsalicylic acid crystals, the samples were first subjected to machine sieving and then hand sieved to visual completion.

## Results and Discussion

### Glass Spheres

Obviously, the Stokes diameter, particle width and sieve size, are equivalent for spherical glass particles. The mass distribution obtained by sieving was converted to the surface area distribution by means of the relationship:

$$\Delta A_i = \frac{\Delta M_i}{L_{\text{sieve},i} \sum_j (\Delta M_j / L_{\text{sieve},j})} \quad (7)$$

where  $\Delta A_i$ ,  $\Delta M_i$  are the surface area fraction and mass fraction in the  $i$ -th size range, respectively, and  $L_{\text{sieve},i}$  is the arithmetic mean of the appropriate sieve apertures. The cumulative size distributions by surface area in the sample of glass spheres are plotted in *Fig. 1*. As anticipated, there is good agreement among the size distributions for spherical particles determined by different methods.

### Copper Sulphate Pentahydrate

In order to check the consistency of sedimentation and microscopic size analyses, we have to find the relationship between the particle width  $L_w$  and the average Stokes diameter  $\bar{d}_{\text{st}}$  [4]. The copper sulphate crystals exhibited a fairly constant elongation ratio  $p = L_L / L_w$  and thickness ratio  $q = L_T / L_w$ ; the average values were  $\bar{p} = 1.71 \pm 0.20$  (arithmetic mean  $\pm$  standard deviation for 652 particles) and  $\bar{q} = 0.52 \pm 0.20$  (18 particles). It follows from the microscopic observations that the shape of these crystals may be approximated adequately by ellipsoids with the axis ratio equal to  $\bar{p} : 1 : \bar{q}$ , differing only in a single scale factor as the size changes. The volume diameter for such an ellipsoid is:

$$d_v = (\bar{p}\bar{q})^{1/3} L_w \quad (8)$$

The correction factor  $(d_v/\bar{d})^{1/2}$  appearing in Eq. (5) was calculated for the given axis ratio 1.71 : 1 : 0.52 by means of Eq. (4):

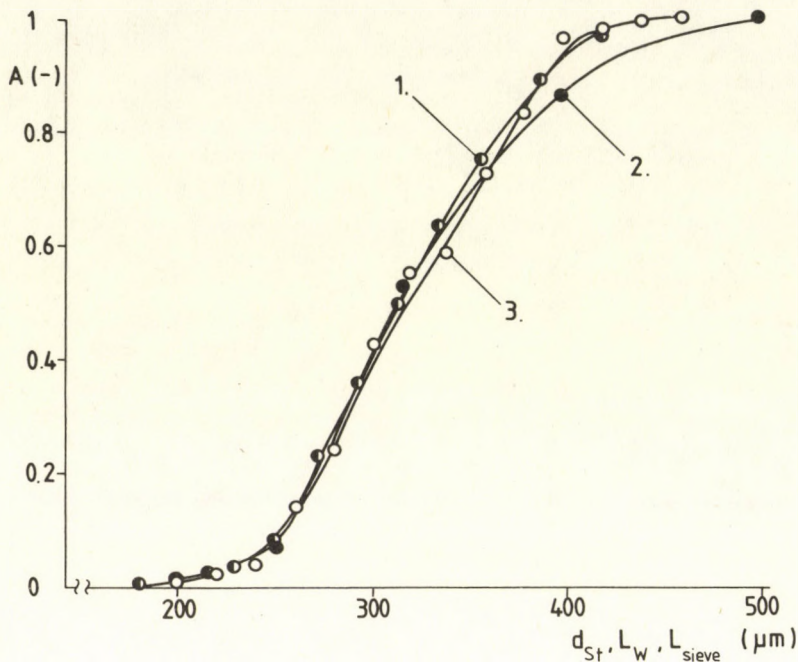


Fig. 1

Glass spheres; cumulative undersize surface area fraction plotted versus  $\bar{d}_{St}$  (the photosedimentation technique – curve 1), versus  $L_{sieve}$  (sieving – curve 2) and versus  $L_W$  (microscopy, 422 particles – curve 3)

$$\begin{aligned} (d_v/\bar{d})^{1/2} &= ((d_v/d_1 + d_v/d_2 + d_v/d_3)/3)^{1/2} = \\ &= ((1.014 + 0.914 + 0.812)/3)^{1/2} = 0.956 \end{aligned}$$

The values of the drag diameters  $d_1$ ,  $d_2$ ,  $d_3$  were obtained using the exact solution of linear hydrodynamic equations for a slow motion of ellipsoid in a viscous fluid [6]. Therefore, according to Eq. (5) and (8), the average Stokes diameter of a particle with the width  $L_W$  is equal to  $\bar{d}_{St} = 0.919L_W$ . Since the crystals are assumed to be of the same shape, the relationship between  $\bar{d}_{St}$  and  $L_W$  is valid over the entire size range and the plots of cumulative surface area fractions versus  $\bar{d}_{St}$  and  $L_W$  may be mutually converted by a simple change of the abscissa scale according to the relationship  $\bar{d}_{St} = 0.919L_W$ , as shown in Fig. 2.

It is of interest to note that in the sieve cut 200 to 315  $\mu\text{m}$  used in the experiments, there were crystals having a width greater than the nominal aperture of the upper sieve; relatively flat crystals of copper sulphate can pass through the sieve aperture diagonally and, therefore, the width (“the second-largest dimension”) is not equal to the sieve aperture as usually stated.

### Acetylsalicylic Acid

The prismatic crystals of acetylsalicylic acid exhibit considerable variability of the elongation ratio  $p$ . The average elongation ratio  $p$  evaluated for a constant particle width  $L_w$  decreases with increasing  $L_w$  according to the empirical equation:

$$p = 6.40 - 0.028L_w \quad (9)$$

( $L_w$  is expressed in micrometers; coefficient of correlation 0.955), as shown in Fig. 3. Even for a given particle width, there is a significant spread of elongation ratios. For example, for  $L_w = 20 \mu\text{m}$ , it is possible to find crystals with an elongation ratio ranging from 1 to 11. The spread of  $p$  values decreases with increasing crystal width. In Fig. 4, the distributions of the elongation ratio are plotted for several crystal widths. In the calculation of the overall area-weighted average value of the elongation ratio,  $\bar{p} = 4.46 \pm 1.69$  (1153 particles measured), a weighting factor equal to the surface area of the crystal was assigned to each

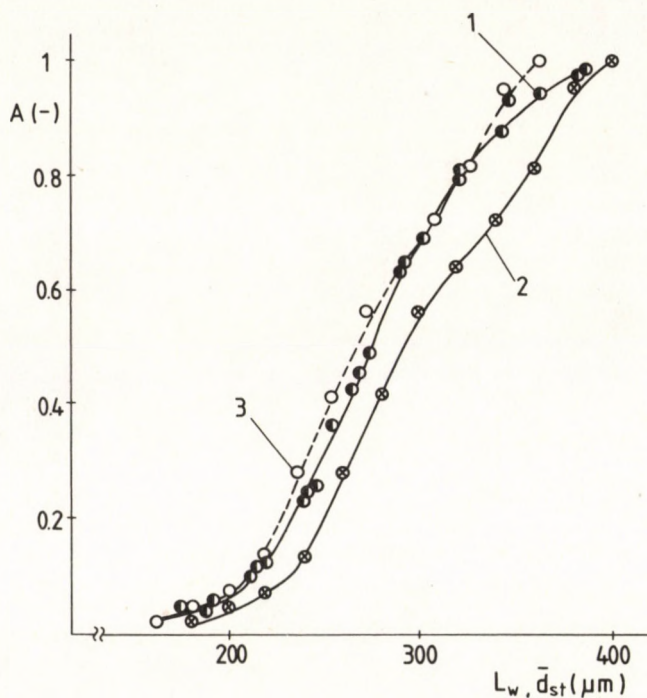


Fig. 2

Copper sulphate; cumulative undersize surface area fraction plotted versus  $\bar{d}_{st}$  (photosedimentation technique - curve 1) and versus  $L_w$  (microscopy, 652 particles - curve 2); results of microscopy expressed as a function of  $\bar{d}_{st}$  according to the relationship  $\bar{d}_{st} = 0.919 L_w$  - curve 3)

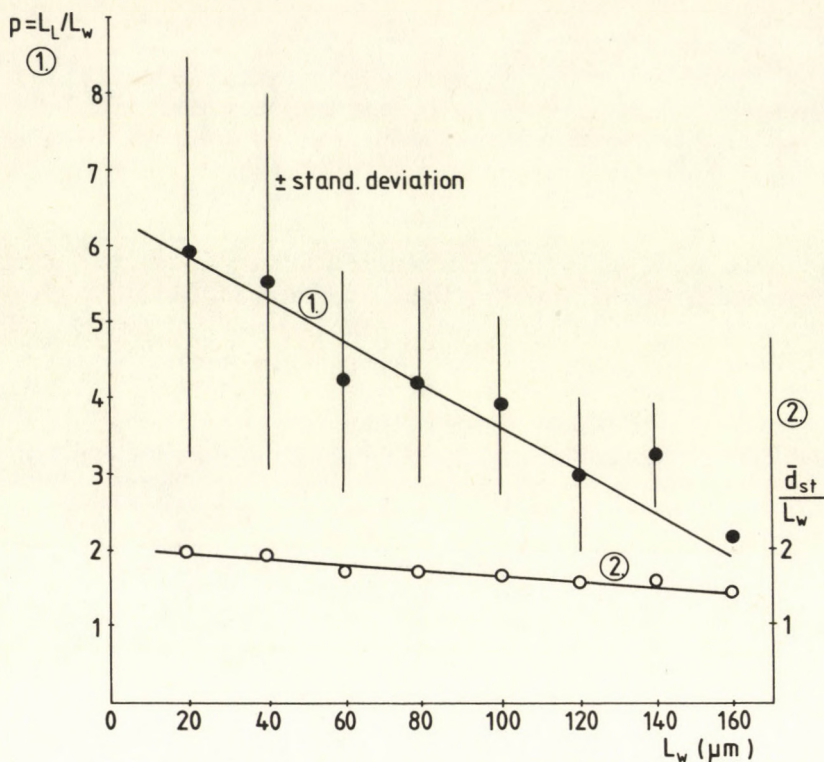


Fig. 3

Acetylsalicylic acid; average value of the length/width ratio  $p$  plotted versus the crystal width  $L_w$  - curve 1 (the bars indicate  $\pm$  standard deviation); ratio  $\bar{d}_{st}/L_w$  (calculated for thickness ratio  $q = 0.85$  and for elongation ratio  $p$  varying with  $L_w$  according to Eq. (9)) plotted versus  $L_w$  - curve 2

value of elongation ratio. Similarly, the overall area-weighted average value of the thickness ratio  $\bar{q} = 0.85 \pm 0.24$  (35 particles) was calculated from a limited number of thickness measurements.

Experimental data obtained by different size analysis methods will now be compared in order to check their consistency.

### 1. Microscopy versus photosedimentation technique

To compare the size distribution data derived from the photomicrographs with the results of the photosedimentation technique, the particle shape was approximated by a prism. For selected values of crystal width  $L_w$  in the plot of the cumulative surface area versus crystal width derived from the photomicrographs, the corresponding values of average Stokes diameter  $\bar{d}_{st}$  were calculated. First, the volume diameter  $d_v$  and the sphericity of crystals  $\psi$  were obtained according to the equations:

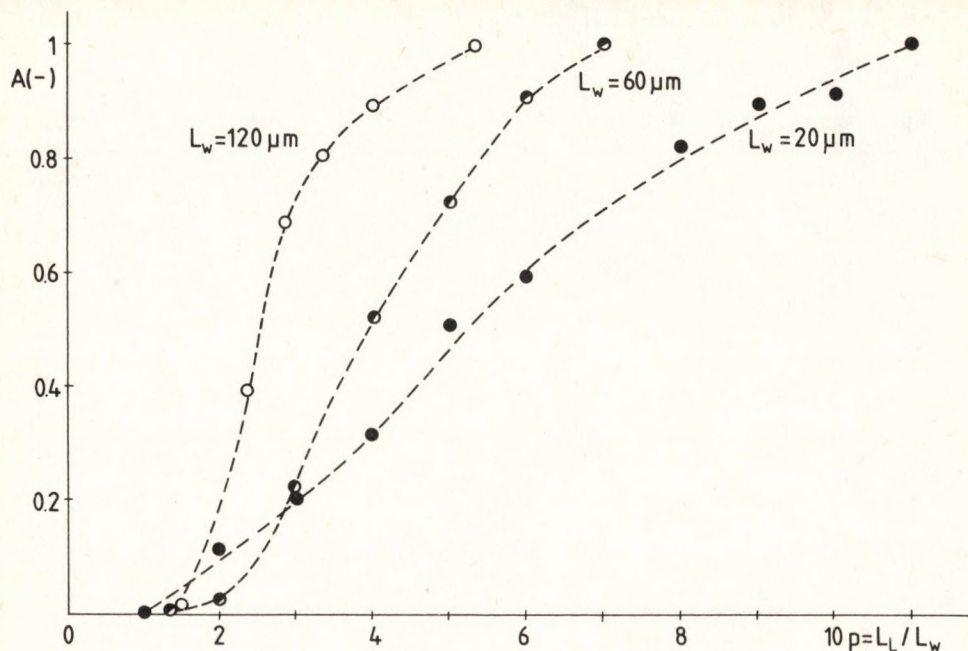


Fig. 4

Acetylsalicylic acid; cumulative distribution (by surface area) of elongation ratio  $p$  for a fixed crystal width  $L_w$

$$d_v = \left( \frac{6p\bar{q}}{\pi} \right)^{1/3} L_w, \quad \psi = \frac{\pi^{1/3}(6p\bar{q})^{2/3}}{2(p+p\bar{q}+\bar{q})} \quad (10), (11)$$

where the elongation ratio  $p$  is a function of  $L_w$  according to Eq. (9); the overall average value of the thickness ratio  $\bar{q}$  was used in Eq. (10), (11), since, as already stated,  $q$  was measured only for a limited number of crystals. The average Stokes diameter was then calculated by means of the approximate Equation (6). Thus, the statistical distribution of the elongation ratio  $p$  existing for a fixed crystal width was neglected, whereas the functional dependence between the average elongation ratio and the crystal width was taken into consideration.

The surface area distribution  $A(L_w)$ , which was obtained by microscopy is replotted against the calculated average Stokes diameter in Fig. 5. Good agreement can be seen between that plot and the experimental results of the photo-sedimentation technique, indicating the consistency of both data sets.

The values of the particle width  $L_w$  were also converted to the corresponding values of the average Stokes diameter  $\bar{d}_{st}$  by means of Eq. (10), (11) and (6) using only the overall average value of the elongation ratio  $\bar{p} = 4.46$ , i.e. completely neglecting the variation of the relative proportions of crystals. The resulting relationship between  $\bar{d}_{st}$  and  $L_w$  was  $\bar{d}_{st} = 1.73L_w$ . Even this simple procedure gives (with the exception of the upper size range) a relatively good approxima-

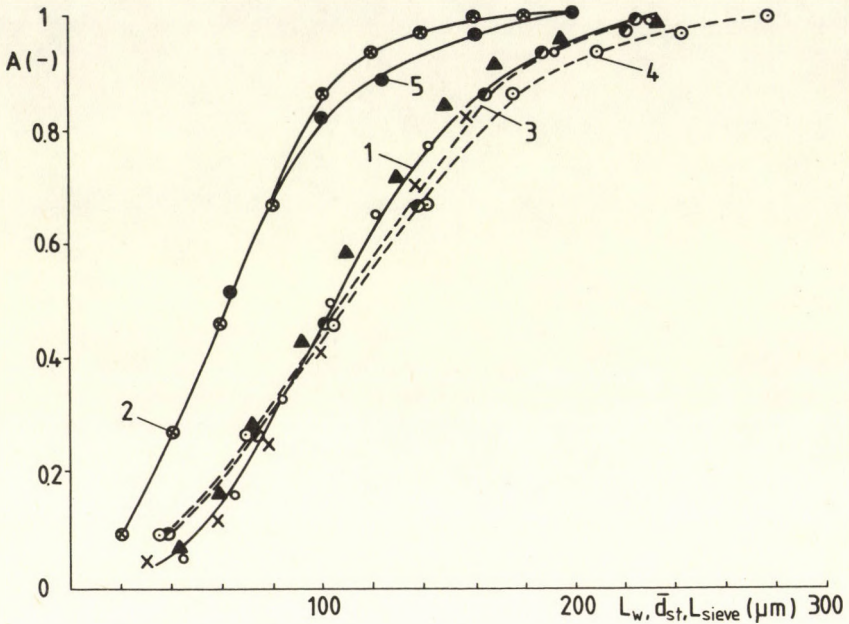


Fig. 5

Acetylsalicylic acid; cumulative undersize surface area fraction plotted versus  $\bar{d}_{st}$  (photosedimentation technique – curve 1) and versus  $L_w$  (microscopy, 1153 particles – curve 2); results of microscopy expressed as a function of  $\bar{d}_{st}$ , elongation ratio varying with  $L_w$  according to Eq. (9) – curve 3; results of microscopy expressed as a function of  $\bar{d}_{st}$ , constant elongation ratio  $\bar{p} = 4.46$  – curve 4; results of sieve analysis expressed as the surface area distribution and plotted versus  $L_{sieve}$  – curve 5

tion of the experimental distribution obtained by the photosedimentation technique as shown in Fig. 5.

## 2. Sieving versus microscopy

The mass distribution measured by sieve analysis was transformed to the surface area distribution (assuming for prismatic crystals of acetylsalicylic acid that the size dimension measured by sieving is equal to the crystal width):

$$\Delta A_i = \frac{k_i \Delta M_i / L_{sieve,i}}{\sum_i (k_i \Delta M_i / L_{sieve,i})} \quad (12)$$

where:

$$k_i = 1 + 1/p_i + 1/\bar{q} \quad (13)$$

and:  $p_i$  was calculated from Eq. (9) for  $L_W$  equal to  $L_{\text{sieve},i}$  (the arithmetic mean of the appropriate sieve apertures). The resulting surface area distribution is also plotted in Fig. 5. Both data compare well, in particular in the range of small crystals.

### 3. Leitz-Classimat versus microscopy

For non-spherical particles, the surface area distributions  $A(L_{\text{cord}})$  plotted as a function of maximum cord  $L_{\text{cord}}$  drawn in a selected direction (the dimension measured by the Leitz-Classimat instrument) is necessarily more spread than the surface area distribution  $A(L_W)$  plotted against the particle width  $L_W$ . This is due to a random orientation of crystals in the field of view. These two surface area distributions are related by the following integral equation:

$$A(L_{\text{cord}}) = \int_0^{L_{\text{cord}}} dL_{\text{cord}} \int_0^{\infty} g(L_{\text{cord}}|L_W) \left( \frac{dA(L_W)}{dL_W} \right) dL_W \quad (14)$$

where  $g(L_{\text{cord}}|L_W)$  is the conditional probability density function, i.e.  $g(L_{\text{cord}}|L_W) dL_{\text{cord}}$  is the probability that a cord drawn in a selected direction through the

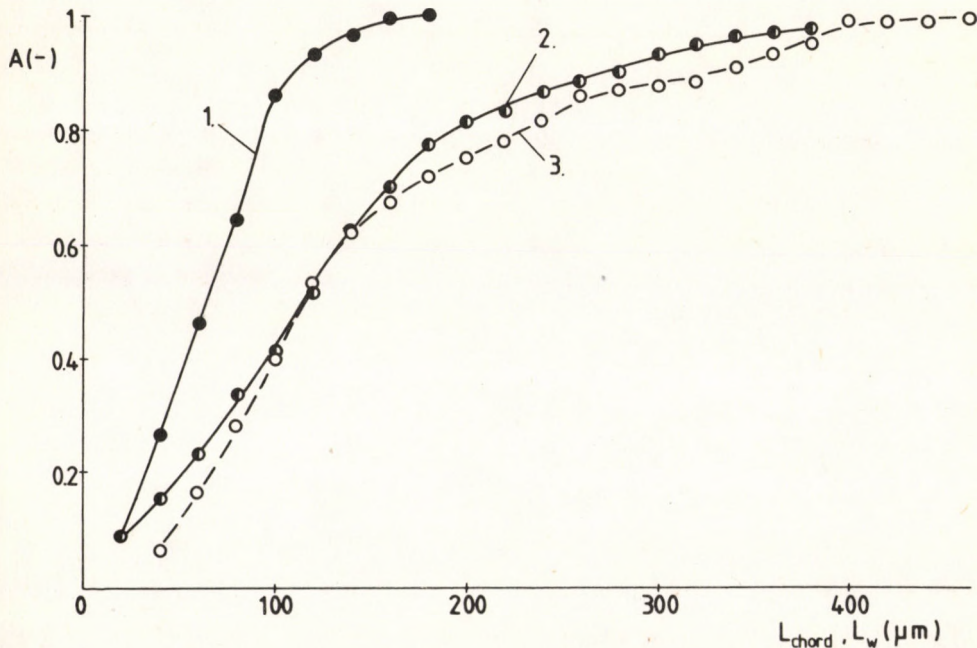


Fig. 6

Acetylsalicylic acid; cumulative undersize surface area fraction plotted versus  $L_W$  (microscopy, 1153 particles - curve 1) and versus  $L_{\text{cord}}$  (Leitz-Classimat - curve 2); results of microscopy expressed as a function of  $L_{\text{cord}}$  according to Eq. (14), (15a) (15b) - curve 3

Table 1.

Ratio of the volume diameter  $d_v$  to the drag diameters  $d_1$ ,  $d_2$  and  $\bar{d}$  for cylinders and rectangular prisms (experimental data [8]) and ellipsoids (exact solution of the Navier-Stokes equations [6]);  $\bar{d}$  is given by Eq. (4) with  $d_3$  equal to  $d_2$

	axis ratio	$(d_v/d_1)^{1/2}$	$(d_v/d_2)^{1/2}$	$(d_v/\bar{d})^{1/2}$	$\psi^{1/4}$
cylinder	4 : 1 : 1	0.964	0.871	0.903	0.926
prism	4 : 1 : 1	0.959	0.872	0.902	0.907
ellipsoid	4 : 1 : 1	0.997	0.879	0.920	0.940
ellipsoid	10 : 1 : 1	0.902	0.752	0.805	0.876

Table 2.

Sedimentation behaviour of agglomerates consisting of  $n$  identical spheres of diameter  $d$

numer of spheres, $n$	1	2	3	4
arrangement	—	—	triangular	tetraedric
volume diameter $d_v = n^{1/3}d$	$d$	$1.260d$	$1.442d$	$1.587d$
surface area $S = n\pi d^2$	$\pi d^2$	$2\pi d^2$	$3\pi d^2$	$4\pi d^2$
sphericity $\psi = n^{-1/3}$	1	0.794	0.693	0.630
$\bar{d}_{St} = \psi^{1/4}d_v$ (Equation (6))	$d$	$1.189d$	$1.316d$	$1.414d$
$L_w$	$d$	$d$	$1.866d$	$1.866d$
$\bar{d}_{St}/L_w$	1	1.189	0.705	0.758

particle image having the width  $L_w$  will have a length within the range  $L_{cord}$  to  $L_{cord} + dL_{cord}$ . For a rectangular particle silhouette we have for  $L_{cord} < pL_w$ :

$$g(L_{cord}|L_w) = \frac{2}{\pi L_{cord} \sqrt{\left(\frac{L_{cord}}{L_w}\right)^2 - 1}} \quad (15a)$$

and for  $L_{cord} \geq pL_w$ :

$$g(L_{cord}|L_w) = \frac{2}{\pi L_{cord}} \frac{p}{\sqrt{\left(\frac{L_{cord}}{L_w}\right)^2 - p^2}} + \frac{1}{\sqrt{\left(\frac{L_{cord}}{L_w}\right)^2 - 1}} \quad (15b)$$

The surface area distribution  $A(L_w)$  obtained for acetylsalicylic acid from the evaluation of photomicrographs by hand was converted to the distribution  $A(L_{\text{cord}})$  by numerical integration of Eq. (14) using the values of elongation ratio  $p$  given by Eq. (9). It can be seen from Fig. 6 that the surface area distribution  $A(L_{\text{cord}})$  calculated from the surface area distribution  $A(L_w)$  is close to the experimental surface area distribution  $A(L_{\text{cord}})$  measured by the Leitz-Classimat instrument. Nevertheless, it should be noted that measuring a distribution by an orientation-dependent method contributes heavily to the spread of the results and that the numerical deconvolution of Eq. (14) to obtain distribution  $A(L_w)$  from a measured distribution  $A(L_{\text{cord}})$  is more complex than the straightforward calculation of  $A(L_{\text{cord}})$  for a given distribution  $A(L_w)$ .

### *Potassium Aluminium Sulphate*

Visual examination of the potash alum samples revealed both discrete octahedral crystals and agglomerates of "elementary" particles. The surface area distributions  $A(\bar{d}_{\text{st}})$  and  $A(L_w)$  determined by the photosedimentation technique and by the evaluation of photomicrographs are shown in Fig. 7. Also included in the Figure is a plot of the size distribution of elementary particles (i.e. single particles and particles involved in agglomerates) which was determined from the photomicrographs. Single crystals and agglomerates involving 2, 3 and 4 elementary particles prevailed: the ratio of the number of elementary particles and the sum of agglomerates and single crystals was 1.9. It is apparent from Fig. 7 that median sizes of the distributions  $A(L_w)$  and  $A(\bar{d}_{\text{st}})$  are practically identical, but the distribution determined by microscopy is more spread than that obtained by the photosedimentation technique.

For a further discussion of these results, the average Stokes diameters and the widths of an agglomerate formed by  $n$  identical touching spheres (used to approximate the elementary octahedral particles) were estimated assuming that the average Stokes diameter of such an agglomerate may be calculated from Eq. (6). It is apparent from Table 2 that the agglomerates comprising three or four building units exhibit a smaller ratio  $\bar{d}_{\text{st}}/L_w$  than single particles or doublets. On average, the  $\bar{d}_{\text{st}}/L_w$  ratio is approximately equal to 1; this may explain the agreement between median sizes of  $A(L_w)$ , and  $A(\bar{d}_{\text{st}})$  distributions.

From the microscopic observations of the crystal samples, as well as from the size distribution of elementary particles, it follows that the number of elementary particles making up an agglomerate varies approximately from 2 to 3 or 4 with increasing agglomerate width  $L_w$ . Therefore, the conversion of the surface area distribution  $A(L_w)$  into the distribution  $A(\bar{d}_{\text{st}})$  should qualitatively be done in such a way that the part of the  $A(L_w)$  curve corresponding to smaller agglomerate widths should be shifted in the direction of increasing  $L_w$  (since  $\bar{d}_{\text{st}}/L_w$  is greater than 1 according to Table II), whereas the part of the  $A(L_w)$  curve corresponding to larger agglomerate widths should be shifted in the opposite direction ( $\bar{d}_{\text{st}}/L_w < 1$ ) - indicated by arrows in Fig. 7. The calculated

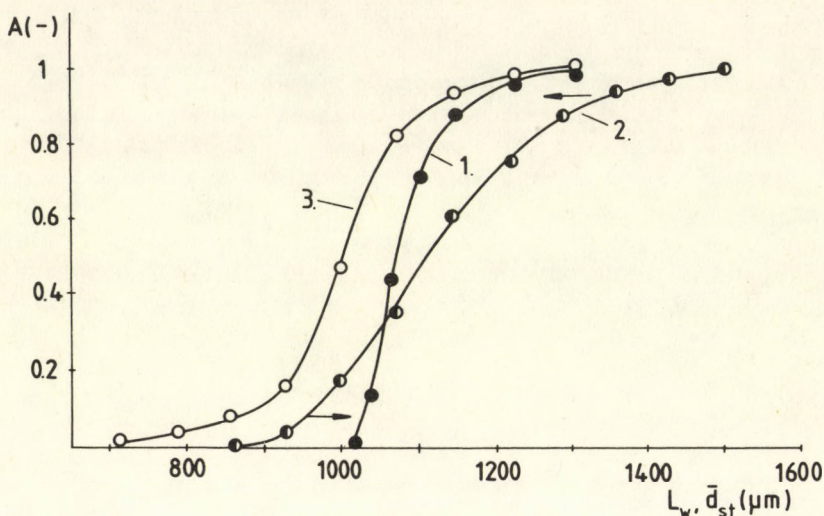


Fig. 7

Potassium aluminium sulphate; cumulative undersize surface area fraction plotted versus  $\bar{d}_{st}$  (photosedimentation technique – curve 1), versus the particle width  $L_w$  (microscopy, 577 agglomerated particles or single crystals – curve 2) and versus the width of elementary particles, i.e. single crystals and building units of agglomerates (microscopy, 571 elementary particles – curve 3); arrows indicate (qualitatively) transformation of the experimental distribution  $A(L_w)$  into the distribution  $A(\bar{d}_{st})$

distribution  $A(\bar{d}_{st})$  should be narrower than the distribution  $A(L_w)$  and should, therefore, approach the experimental distribution  $A(\bar{d}_{st})$ .

It should be recalled that the degree of agglomeration of the potash alum sample is relatively low. In such a case, the shape of agglomerate varies significantly with every addition of a building unit. The relative position of the building units and their different sizes also contribute to the variability of agglomerate shapes. Therefore, it is very difficult to describe quantitatively the distribution of the shapes in a partially agglomerated sample. The situation will be more favourable for higher degrees of agglomeration; it follows from geometrical considerations that with an increasing number of constituent particles, the shape of an agglomerate will tend to be more spherical.

### Conclusions

1. Microscopic measurements of elongation and thickness ratio proved to be a useful tool in the quantitative characterization of crystal shapes and the distribution of shapes in a crystal population.

2. Relatively limited information on crystal shapes is sufficient for mutual conversion of the results obtained by the photosedimentation method and

microscopy (or sieving) as demonstrated with samples of copper sulphate and acetylsalicylic acid crystals. Even though the elongation ratio of acetylsalicylic acid crystals varied in a wide range for a constant crystal width, the distribution of average Stokes diameters by surface area was successfully reconstructed using only a single (average) elongation ratio for each crystal width; acceptable results were obtained even by assuming the elongation ratio to be constant over the entire population of crystals.

3. Approximate equation (6) gives satisfactory estimates of the average Stokes diameters of non-spherical particles.

### Symbols

$A$	cumulative undersize fraction of surface area, -
$d_i$ ( $i = 1, 2, 3$ )	drag diameters of an orthotropic particle moving in the direction of the particle axis $x_i$ , [m]
$\bar{d}$	average drag diameter defined by Eq. (4), [m]
$d_s$	surface diameter (diameter of the sphere having the same surface area as the particle), [m]
$\bar{d}_{St}$	average Stokes diameter of the particle, [m]
$d_v$	volume diameter (diameter of a sphere having the same volume as the particle), [m]
$F_1$	drag force exerted on a particle moving in the direction of particle axis $x_1$ , [ $\text{kg} \cdot \text{m}/\text{s}^2$ ]
$g$	acceleration due to gravity, [ $\text{m}/\text{s}^2$ ]
$g(L_{\text{cord}} L_W)$	conditional probability density, Eq. (15), -
$L_{\text{cord}}$	maximum length of a cord drawn in a fixed direction through the particle image, [m]
$L_L, L_W, L_T$	length, width and thickness, respectively, of a particle, [m]
$L_{\text{sieve}}$	side dimension of sieve aperture, [m]
$M$	cumulative undersize mass fraction, -
$p = L_L/L_W$	elongation ratio, -
$q = L_T/L_W$	thickness ratio, -
$Re = \bar{u}d_v\rho/\mu$	Reynolds number of particle sedimentation, -
$u_1, \bar{u}$	terminal settling velocity in the direction of particle axis $x_1$ and average settling velocity, respectively, [m/s]
$\rho$	density of sedimentation liquid, [ $\text{kg}/\text{m}^3$ ]
$\Delta\rho$	difference in density between the particle and sedimentation liquid, [ $\text{kg}/\text{m}^3$ ]
$\psi$	sphericity of a particle, $\psi = d_v^2/d_s^2$ , [-]
$\mu$	viscosity of sedimentation liquid, [ $\text{kg}/(\text{m} \cdot \text{s})$ ]

### LITERATURE

1. ALLEN, T.: Particle Size Measurement, Chapman and Hall, London, 1975. p. 76.
2. LUERKENS, D. W., BEDDOW, J. K. and VETTER, A. F.: Powder Technology 1987, 50, 93.
3. KAYE, B. H.: Powder Technology 1978, 21, 1.
4. HOSTOMSKÝ, J., HALÁSZ, ZS., LISZI I. and NÝVLT, J.: Powder Technology 1986, 49, 45.
5. BUDZ, J., JONES, A. G. and MULLIN, J. W.: Ind. Eng. Chem. Res. 1987, 26, 820.
6. HAPPEL, J. and BRENNER, H.: Low Reynolds Number Hydrodynamics. Chapter 5, Prentice-Hall, Englewood Cliffs, 1965.
7. HAWSKLEY, P. W. G.: British Coal Utilization Research Bulletin 1951, 15, 4.
8. HEISS, J. F. and COULL, J.: Chem. Eng. Progress 1952, 48, 133.
9. HEYWOOD, H.: J. Pharm. Pharmac. 1963, 15 (Supplement), 56T



## USE OF MICELLES IN A PHOTOGALVANIC CELL FOR SOLAR ENERGY CONVERSION AND STORAGE: AZUR A-EDTA SYSTEM.

SURESH C. AMETA, MISS SADHNA KHAMESRA, RAMESHWER AMETA and MRS. SUSHILLA LODHA

(Department of Chemistry, University College of Science, Sukhadia University, Udaipur (Rajasthan) 313 001 India.)

Received: December 21, 1989

Sodium lauryl sulphate (NaLS), cetyl pyridinium chloride (CPC) and triton x-100 (TX-100) were used in a photogalvanic cell containing azur-A as a photosensitizer and EDTA as a reductant for solar energy conversion and storage. The photopotential and photocurrent generated by the cell in the presence of NaLS were 932 mV and 44 $\mu$ A, respectively. The effect of the variation of the concentrations of the surfactants on the electrical output, fill-factor, conversion efficiency and performance of the cell in the dark was studied in detail. In the presence of NaLS, the cell can be used in the dark (storage capacity) for 155 minutes.

### Introduction

Photogalvanic effect was first discovered in 1925 by RIDEAL and WILLIAMS [1], but it was systematically investigated by RABINOWITCH [2]. This kind of work was followed, later on, by various workers throughout the world [3-15]. Problems encountered in the development of this field were discussed by HOFFMAN and LICHTIN [16]. The expected conversion efficiency of an ideal photogalvanic cell is about 18% [17], but the observed conversion efficiencies are quite low (0.03-0.1%). Back-electron transfer, low stability of dyes, aggregation of dye molecules around the electrode, and reversible oxidation of reductant, etc., are considered the main reasons for the lower output.

A careful survey of literature reveals that various photosensitizers like proflavin [18], tolusafranine [17], riboflavin [11], and brilliant cresyl blue [12, 14], etc., have been used in photogalvanic cells, but no attention was paid to Azur-A as a photosensitizer with EDTA and, therefore, the present work was undertaken. Secondly, the photovoltaic cell cannot be used in the absence of light, whereas photogalvanic cells (of course with lower conversion efficiency) can be

used in the dark for a reasonably good time period. Use of surfactants (micelles) in photogalvanic cell showed an appreciable increase in the performance of the cell; therefore, the work was further investigated using cationic, anionic and neutral micelles.

### Experimental

Azur-A (Chroma), sodium lauryl sulphate (Sisco), cetyl pyridinium chloride (Sisco), triton x-100 (BDH), sodium hydroxide (SM) and EDTA-disodium salt (EM 'GR') were used in the present work. Doubly distilled water was used to prepare all the solutions. A mixture of the solutions of the dye, EDTA, sodium hydroxide and surfactant was taken in H-shaped glass cells. Platinum electrode ( $1.0 \times 1.0 \text{ cm}^2$ ) was dipped in one limb of the cell and a saturated calomel electrode (SCE) was kept in the other one. The platinum electrode was exposed to a 200 W tungsten lamp (Sylvania) and the limb containing the SCE was kept in the dark. A water filter was placed between the exposed limb and the light source to cut-off infra-red radiations.

The photochemical bleaching of azur-A was studied potentiometrically. The photopotential and photocurrent generated by the system azur-A/EDTA/ $\text{OH}^-$ /surfactant/ $h\nu$  were measured by digital pH meter (Systronics model 335) and multimeter (Systronics Model 435) respectively. The  $i$ - $V$  characteristics of the cell were studied by using an external load (log 500 K) in the circuit. Intensity of light was measured by solarimeter (CEL Model SM 203), as  $13.5 \text{ mWcm}^{-2}$ .

### Results and Discussion

The optimum conditions for the azur-A-EDTA system were determined first in the absence of surfactants [22]: pH = 12.5, [Azur-A] =  $4.8 \times 10^{-5} \text{ M}$ , [EDTA] =  $1.2 \times 10^{-3} \text{ M}$ , Temperature = 303 K, Intensity =  $13.5 \text{ mWcm}^{-2}$ . The photopotential and photocurrent generated by the cell were 807 mV and 40  $\mu\text{A}$ , respectively.

#### *Effect of Variation of Concentrations of Surfactant:*

The effect of variation of the concentrations of surfactant on the electrical output was studied in detail and the results are reported in *Table 1*, *Table 2* and *Table 3*, respectively. It is clear from all the Tables that the electrical output increases in the presence of all the micelles at the concentrations just above the critical micelle concentration (CMC) of the surfactants; [NaLS] =  $8.4 \times 10^{-3} \text{ M}$ ; [CPC] =  $9.2 \times 10^{-4} \text{ M}$ ; [Triton-X-100] =  $3.4 \times 10^{-4} \text{ M}$ .

Table 1

## Effect of NaLS Concentration

[Azur A] =  $4.8 \times 10^{-5}$  M  
pH = 12.5

[EDTA] =  $1.2 \times 10^{-3}$  M  
Intensity =  $13.5 \text{ mWcm}^{-2}$   
Temperature = 303 K

[NaLS] $\times 10^3$ M	Photopotential (mV)	Photocurrent ( $\mu\text{A}$ )
—	807.0	40.0
6.6	836.0	41.0
7.4	882.0	42.0
8.2	917.0	44.0
8.6	932.0	44.0
9.0	804.0	39.0
9.8	713.0	36.0

Table 2

## Effect of CPC Concentration

[Azur A] =  $4.8 \times 10^{-5}$  M  
pH = 12.5

[EDTA] =  $1.2 \times 10^{-3}$  M  
Intensity =  $13.5 \text{ mWcm}^{-2}$   
Temperature = 303 K

[CPC] $\times 10^4$ M	Photopotential (mV)	Photocurrent ( $\mu\text{A}$ )
—	807.0	40.0
7.4	811.0	40.0
8.0	817.0	40.0
8.6	820.0	41.0
9.0	824.0	41.0
9.3	827.0	41.0
9.7	763.0	40.0
10.0	714.0	40.0

Table 3

## Effect of triton x-100 Concentration

[Azur A] =  $4.8 \times 10^{-5}$  M  
pH = 12.5

[EDTA] =  $1.2 \times 10^{-3}$  M  
Intensity =  $13.5 \text{ mWcm}^{-2}$   
Temperature = 303 K

[Triton x-100] $\times 10^4$ M	Photopotential (mV)	Photocurrent ( $\mu\text{A}$ )
—	807.0	40.0
2.8	817.0	40.0
3.0	828.0	40.0
3.3	835.0	40.0
3.5	845.0	40.0
3.8	810.0	40.0
4.0	768.0	40.0

*Current-Voltage Characteristics:*

The open circuit voltage ( $V_{oc}$ ) and short circuit current ( $i_{sc}$ ) of the photogalvanic cell were measured on the digital pH meter (keeping the circuit open) and on the multimeter (keeping the circuit closed), respectively. The current and potential values in between these two extreme values ( $V_{oc}$  and  $i_{sc}$ ) were recorded with the help of a carbon pot (log 500 K) connected in the circuit of the multimeter, through which an external load was applied. The current voltage data are given in *Tables 4, 5 and 6.*

Table 4

i-v Characteristics of the Cell in the presence of NaLS  
 [Azur A] =  $4.8 \times 10^{-5}$  M      [EDTA] =  $1.2 \times 10^{-3}$  M  
 pH = 12.5      Intensity =  $13.5 \text{ mWcm}^{-2}$   
 [NaLS] =  $8.6 \times 10^{-3}$  M      Temperature = 303 K

Potential* (mV)	Photocurrent ( $\mu\text{A}$ )	Fill-factor (n)
932.0	0.0	0.45
857.0	5.0	
805.0	10.0	
735.0	15.0	
685.0	20.0	
631.0	25.0	
563.0	30.0	
443.0	35.0	
248.0	40.0	
0.0	44.0	

\* Absolute value

Table 5

i-v Characteristics of the Cell in the presence of CPC  
 [Azur A] =  $4.8 \times 10^{-5}$  M      [EDTA] =  $1.2 \times 10^{-3}$  M  
 pH = 12.5      Intensity =  $13.5 \text{ mWcm}^{-2}$   
 [CPC] =  $9.3 \times 10^{-4}$  M      Temperature = 303 K

Potential* (mV)	Photocurrent ( $\mu\text{A}$ )	Fill-factor (n)
827.0	0.0	0.23
708.0	5.0	
598.0	10.0	
477.0	15.0	
395.0	20.0	
317.0	25.0	
238.0	30.0	
163.0	35.0	
54.0	40.0	
0.0	41.0	

\* Absolute value

Table 6

*i*-*v* characteristics of the Cell in the presence of Triton x-100

[Azur A] =  $4.8 \times 10^{-5}$  M

[EDTA] =  $1.2 \times 10^{-3}$  M

pH = 12.5

Intensity =  $13.5 \text{ mWcm}^{-2}$

[Triton x-100] =  $3.5 \times 10^{-4}$  M

Temperature = 303 K

Potential* (mV)	Photocurrent ( $\mu\text{A}$ )	Fill-factor (n)
845.0	0.0	0.30
708.0	5.0	
605.0	10.0	
523.0	15.0	
467.0	20.0	
402.0	25.0	
314.0	30.0	
209.0	35.0	
0.0	40.0	

\* Absolute value

It was observed that the *i*-*V* curve of the cell deviated from its ideal regular rectangular shape. A point in the *i*-*V* curve, called the power point (pp) was determined, where the product of potential and current is maximum. The values of potential and current at power point is represented as  $V_{pp}$  and  $i_{pp}$ , respectively. With the help of the (*i*-*V*) curve, the fill-factor and conversion efficiency of the cell were determined using formula:

$$\text{Fill-factor} = \frac{V_{pp} \times i_{pp}}{V_{oc} \times i_{sc}} \quad (1)$$

$$\text{Conversion efficiency} = \frac{V_{pp} \times i_{pp}}{13.5 \text{ mWcm}^{-2}} \times 100\% \quad (2)$$

The performance of the cell was studied by applying the external load necessary to have current and potential at power point after removing the source of light. It was observed that the cell in the presence of NaLS, can be used in the dark for 155 minutes. The fill-factor, conversion efficiency and performance of the cell are summarised in Table 7.

#### Effect of Micelles:

The effect of anionic (NaLS), cationic (CPC) and neutral (TX-100) micelles on the photopotential, photocurrent, fill-factor, conversion efficiency and the performance of the cell was studied in detail and the results are summarised in Table 7. Maximum output was obtained at a concentration just above the critical micelle concentration of the surfactant. The anionic micelle was found to give a better output than the cell without micelle, whereas the presence of cationic and neutral micelles adversely affected the output, fill-factor and con-

Table 7

Fill-factor, Conversion Efficiency and Performance of the Cell  
Intensity =  $13.5 \text{ mWcm}^{-2}$  Temperature = 303 K

System	Fill-factor (n)	Conversion efficiency (%)	Performance (capacity to work in dark) (min.)
Azur A-EDTA	0.31	0.0781	61.0
Azur A-EDTA-NaLS	0.45	0.1255	155.0
Azur A-EDTA-CPC	0.23	0.0593	87.0
Azur A-EDTA-Triton x-100	0.30	0.0747	110.0

version efficiency (cf. Table 7), however, all the micelles increase the usefulness of the cell in the dark (storage capacity) in the order

anionic > neutral > cationic.

This may be due to the better stabilization of dye molecules by the anionic micelle, because azur-A is cationic in nature, secondly, the incorporation of the dye into the anionic micelle will drastically increase the probability of photoejection of electron from micelle aggregates to the aqueous phase [23].

#### Acknowledgement

The authors are indebted to the Professor and Head of the Department of Chemistry, Sukhadia University, Udaipur for providing the necessary laboratory facilities and to the Department of non-conventional energy sources, New Delhi for its financial support. Thanks are also due to Miss Chitra Jain and Shri K. M. Gangotri for their critical discussion.

#### LITERATURE

1. RIDEAL, E. K. and WILLIAMS, D. C.: *J. Chem Soc.* 1925, 258.
2. RABINOWITCH, E.: *J. Chem. Phys.* 1940, 8, 551, 560.
3. OSTER, G. and ADELMAN, A. H.: *J Amer Chem. Soc.* 1956, 78, 913.
4. POTTER, A. E. and THALLER, L. H.: *Solar Energy* 1959, 3, 1.
5. GOMER, R.: *Electrochim Acta* 1975, 20, 13.
6. CLARK, W. D. K. and ECKERT, R. A.: *Solar Energy* 1975, 17, 147.
7. KANEKO, M. and YAMADA, A.: *J. Phys. Chem* 1977, 81, 1213.
8. QUICKENDEN, T. J. and YIM G. K.: *Solar Energy* 1977, 19, 283.
9. KIRSCH-DE MESMAKER, A., LEEMPOEL, P. and NASIELSKI, J.: *Nouv. J. Chem.* 1979, 3, 239.
10. FOX, M. A. and KABIR-UD-DIN: *J. Phys. Chem* 1980, 83, 1800.
11. MURTHY, A. S. N., DAK, H. C. and REDDY, K. S.: *Int. J. Energy Res.* 1980, 4, 339.
12. JAIN, PRABUDH K., JAIN, PRAVEEN K. and AMETA, SURESH C.: *Z. Phys. Chem. (Leipzig)* 1984, 265, 841.

13. AMETA, SURESH C., DUBEY, G. C., DUBEY, T. D. and AMETA, RAMESHWER: *Z. Phys. Chem. (Leipzig)* 1985, 266, 200.
14. AMETA, SURESH C., JAIN, P. K., JANOO, A. K. and AMETA RAMESHWER: *The Energy Journal* 1985, 58, 8.
15. TIEN, H. T. and MOUNTZ, J. M.: *J. Electrochem. Soc.* 1978, 125, 885.
16. HOFFMAN, M. Z. and LICHTIN, N. N.: In *Solar Energy* (Eds. HAUTALA, R. R., KING, R. B. and KUTAL, C.) Clifton (N. J.) 1979, p. 153.
17. ALBERY, W. J. and FOULDS, A. W.: *J. Photochem* 1979, 10, 41.
18. EISENBERG, M. and SILVERMAN, H. P.: *Electrochim Acta.* 1961, 5, 1.
19. ROHATGI-MUKHERGEE, K. K., BAGCHI, M. and BHOWMIK, B. B.: *Electrochim. Acta.* 1983, 28, 293.
20. AMETA, SURESH C., DUBEY, G. C., DUBEY, T. D. and AMETA R. C.: *Z. Phys. Chem. (Leipzig)* 1984, 265, 838.
21. MURTHY A. S. N. and REDDY K. S.: *Solar Energy*, 1983, 30, 39.
22. SETH, SUSHILA: Ph. D. Thesis, Sukhadia University, Udaipur, India 1986.
23. ALKAITIS, S. A., GRATZEL M. and HENGLEINA.: *Ber. Bunsenges. Phys. Chem.* 1975, 79, 541.



## Guide for authors

The "Hungarian Journal of Industrial Chemistry" is a joint publication of the Veszprém scientific institutions of the chemical industry that deals with the results of applied and fundamental research in the field of chemical processes, unit operations and chemical engineering in the form of original articles written in English.

In addition to the scientific workers of the institutions at Veszprém, the Editorial Board of this publication also welcomes articles for inclusion in this periodical, which are written by authors who are engaged in the above mentioned fields.

1. Manuscripts should be sent – **in duplicate** – to the Editor-in-Chief:

Dr. Endre Bodor

Veszprém University of Chemical Engineering (VVE), P.O.B. 158  
H-8201, Veszprém, Hungary

2. *In a brief letter attached to the manuscripts, authors should declare that:*
  - a) their work is original and has not previously been published elsewhere in its present format, and
  - b) for the purposes of correspondence, they can be contacted at the address and telephone number which they give.
3. Manuscripts should be typed on paper of A/4 size.

The first page should give the title, the author's name, place of work and a brief summary of the article (maximum of 15 lines).

If possible the article should be presented with an introduction, experiments carried out, conclusions and discussion. Tables and Figures must be presented on separate sheets and their position in the text should be noted on the margin. A summary of the symbols used, and captions of the Figures should be attached separately to the manuscripts.

It is regretted that photographs cannot be included in the periodical.

The Tables and Figures should not exceed an A/4 size. If diagrams are presented, only the explanation and dimensions of the ordinate and abscissa, and marking numbers are required, while further explanatory texts can be given in the captions of the Figures. The equations used should be numbered, and Tables and Figures should be numbered and noted on the margin.

*With regard to units, it is essential that an SI (Système International d'Unités) should be used.*

4. References should be prepared in the following manner:

a) Publications which have appeared in periodicals; e.g.

WAKAO, N. and SCHWARTZ, J. M.: Chem. Eng. Sci. 1962, 17 (3), 825–827.

b) Books; e.g.

SATTERFIELD, C. N.: Mass Transfer in Heterogeneous Catalysis. MTI Press, Cambridge, Mass., 1951. pp. 26–32.

c) Patents; e.g.

U.S. Pat. 3,425,442, Brit. Pat. 997,665 Hung. Pat. 553,243

d) Published lectures; e.g.

HIH, S., HHU, C. and LEECH, W. J.: A Discrete Method to Heat Conduction Problems. 5th International Heat Transfer Conference, Tokyo, 1975. Co. 2.4.

5. Authors receive 50 complimentary copies of their paper.

**Editorial Board**  
**Hungarian Journal of Industrial Chemistry**

## CONTENTS

BOYADJIEV, CHR.: Asymptotic Theory of Non-Linear Transport Phenomena. II.: Heat Transfer .....	1
BOYADJIEV, CHR.: Asymptotic Theory of the Non-Linear Transport Phenomena. III.: Multicomponent Mass Transfer .....	7
SARBAK, Z.: Model Studies of Catalytic Hydrogenolysis of n-Butylamine over Zeolite and Alumina Catalyst .....	13
EL-DIB, F.I., SALAMA, M.A. and EL-SHARKAWY, A.Y.: New Derivatives of Dichlorobenzene Sulphonanilides for Pest Control in Maize .....	17
HUNG, L.T., GÁRDOS, GY. and KUN SZABÓ, T.: Production of Motor Fuels by Pyrolysis Oil Hydrocracking under Severe Conditions. II. ....	23
KRAMARZ, J. and WYCZESANY, A.: Equilibrium Restrictions in Methanol-to-Gasoline Conversion .....	33
KRAMARZ, J., WYCZESANY, A. and WOLFF, A.: Thermodynamic Model of Coal and Petroleum Feeds Gasification .....	43
IVANOV, B.B., VAKLIEVA-BANCHEVA, N.GR. Ms. and BOYADJIEV, CHR.: Optimal Load of Energy Supply Systems (ESS) During the Performance of Multipurpose Chemical Plans .....	55
BÉKÁSSY-MOLNÁR, E. Ms., MONIUK, W., MUSTAFA, H. and POHORECKI, R.: Simulation of Carbon Dioxide Absorption into Sodium Hydroxide Solutions in a Nutter-Valve Plate Column .....	67
SZALAI, I. and RATKOVICS, F.: A Study of Keto-Enol Tautomerism in Methyl-Ethyl-Ketone + Carbon Tetrachloride Mixtures, Using Linear and Non-Linear Dielectric Methods .....	81
CHIDAMBARAM, M. and MALLESWARARAO, Y.S.N.: Robust Control of High-Order Oscillations in Continuous Isothermal Crystallisers .....	91
BARANYI, J. and ILLENI, T.: Estimation Procedures for Two Stochastic Models Describing Partition and Replication of Plasmids .....	101
BABIN, M.J., NENADOV, R. and ZRNIĆ, Z.: Theoretical Model of the Reaction Equilibria for the Urea-Phosphoric Acid System at the Molar Ratio Less than One .....	111
LISZI, I. MRS., HOSTOMSKY, J., HALÁSZ, Zs. Ms. and NYVLT, J.: Effect of the Crystal Shape on Crystal Size Distribution Measured by the Photosedimentation Technique, Microscopy and Sieving .....	125
AMETA, S.C., KHAMESRA, S. Ms., AMETA, R. and LODHA (Nee SETH), S. Ms.: Use of Micelles in a Photogalvanic Cell for Solar Energy Conversion and Storage: Azur A-EDTA System .....	141